



Energy, Mines and
Resources Canada

Énergie, Mines et
Ressources Canada

Earth Physics Branch

Direction de la physique du globe

1 Observatory Crescent
Ottawa Canada
K1A 0Y3

1 Place de l'Observatoire
Ottawa Canada
K1A 0Y3

**Geothermal Service
of Canada**

**Service géothermique
du Canada**

**ICE-MOSES. THE THEORY OF A NEW OFFSHORE
ELECTRICAL METHOD AND A PROPOSAL FOR AN
ARCTIC TRIAL**

**R.N. Edwards
University of Toronto
Toronto, Ontario**

**Earth Physics Branch Open File Number 85-14
Dossier public de la Direction de la Physique du Globe No. 85-14**

NOT FOR REPRODUCTION

REPRODUCTION INTERDITE

**Department of Energy, Mines and
Resources Canada
Earth Physics Branch
Division of Gravity, Geothermics
and Geodynamics**

**Ministre de l'Énergie, des Mines
et des Ressources du Canada
Direction de la physique du globe
Division de la gravité, géothermie
et géodynamique**

This document was produced
by scanning the original publication.

Ce document est le produit d'une
numérisation par balayage
de la publication originale.

ABSTRACT

This report outlines an electrical method (MOSES) designed to sound the seafloor in arctic regions. A description of the factors which influence the electrical conductivity of material beneath the sea (including permafrost) is first presented. The theory of the MOSES method is then developed and followed by numerical modelling of its response to one and three dimensional typical arctic structures. The report concludes with the detailed proposal and budget for an Arctic experiment.

RÉSUMÉ

Ce rapport décrit une méthode électrique (MOSES) conçue pour le sondage des fonds océaniques arctiques. Les facteurs qui influencent la conductivité électrique des matériaux sous-marins, y compris le pergélisol, sont d'abord présentés. La théorie de la méthode MOSES est ensuite développée et suivie de modélisations numériques de sa réponse à des structures arctiques typiques uni- et tri-dimensionnelles. Le rapport termine avec les détails et le budget d'une expérimentation proposée pour l'Arctique.

ICE - MOSES

The theory of a new offshore electrical method
and
a proposal for an Arctic trial

R. N. Edwards

*Geophysics Laboratory, Department of Physics,
University of Toronto, Toronto, Ontario,
Canada, M5S 1A7*

Submitted to *Department of Energy, Mines and Resources*

March 31st, 1985

DSS File Number 20ST.23235-3-1430

Table of Contents

| | |
|---|----|
| 1. Introduction | 2 |
| 1.1 Permafrost | 3 |
| 1.2 Sub-sea geophysical methods in Arctic areas | 4 |
| 1.3 MOSES | 6 |
| 2. Factors influencing marine sediment resistivity | 9 |
| 2.1 Archie's formula | 9 |
| 2.2 Porosity and resistivity variation with depth | 13 |
| 2.3 Transverse isotropy | 16 |
| 3. Theory | 20 |
| 3.1 The MOSES response of an anisotropic layered medium | 20 |
| 3.2 Impedance transfer accross an exponential layer | 26 |
| 3.3 The static MOSES response of a lamella | 28 |
| 3.4 The electromagnetic MOSES response of a disc | 36 |
| 4. Numerical modelling and experimental design | 42 |
| 4.1 Analysis of an electric log: macro-anisotropy | 42 |
| 4.2 Forward one dimensional modelling | 48 |
| 4.3 Eigenparameter statistical analysis | 55 |
| 4.4 Model resolution, hypothesis testing | 60 |
| 4.5 Three dimensional modelling | 70 |
| 5. Research proposal and budget | 82 |
| References | 86 |

1. Introduction

In March 1984, the University of Toronto, Department of Physics, was contracted by the Department of Energy, Mines and Resources, Earth Physics Branch, Government of Canada, to develop an electrical method to sound the seafloor in Arctic regions, specifically in the Beaufort Sea. The statement of work included, "*The preparation of a complete report documenting the system design and capabilities, the preparation of a theoretical analysis of the application of the method to permafrost mapping and the presentation of a detailed proposal for an Arctic test.*" This document is a description of the work completed to date.

It is divided into a number of sections. The introduction continues with the presentation of mainly background material on permafrost, on the geophysical methods currently used for Arctic exploration and on the reasons for the choice of the MOSES as one of the more suitable electrical methods. The second section is devoted to a description of the factors which influence the electrical conductivity of material beneath the sea, including permafrost. It is in this section that the concept of transverse macro-isotropy is introduced - the grouping together of several thin, horizontal, isotropic layers to form a thicker, anisotropic zone, capable of being resolved by a electrical method. At the start of the project, the inclusion of effects of anisotropy was thought to be quite important, but not nearly as important as the subsequent data analyses and design studies were to demonstrate.

The third section of the report contains the theoretical studies. Much of this work is original. The response of the MOSES method to a one-dimensional model, which includes layers which are anisotropic and whose resistivities increases exponentially with depth, is calculated. A novel integral equation technique for calculating the local anomalies associated with three-dimensional conductive and resistive zones is also described.

The responses of the MOSES method to one and three dimensional structures typical of those found in the Arctic are presented in section four. Suitable parameters for the one dimensional forward models are determined by filtering an electrical log from an offshore well which passes through unfrozen sediment and permafrost of various kinds. Estimates of the resolution of model parameters from typical data

sets with typical errors, the inverse problem, are also given using the eigenparameter statistical analysis of generalized inverse theory.

The fifth and final section of the report is the proposal and budget for an Arctic experiment.

1.1: Permafrost.

The term "permafrost" is a contraction of "permanent frost". It is by definition, *"any soil, subsoil, or other surficial deposit, or even bedrock, occurring in Arctic regions at a variable depth beneath the Earth's surface, in which a temperature below freezing has existed continuously for a long time (at least two years)."* The definition is based exclusively on temperature, without regard to texture, degree of compaction, water content or lithologic character of the material. Permafrost may be bonded, when the interstitial water freezes, *hard permafrost*, or unbonded, when high dissolved salt concentrations keep interstitial water from freezing, *soft permafrost*. Clearly, a degree of softness can be defined which depends on the amount of ice-bonding.

The permafrost under the Beaufort Sea is a layer from 100 to 600 meters thick, underlying shallow water, typically 50 to 100 meters deep, and several tens of meters of soft sediment. There are a number of reasons for trying to map this geological phenomenon more accurately. The Beaufort Sea area is now known to contain several major petroleum reservoirs and a greater knowledge of sub-sea structure will aid in both development and further discoveries. With regard to development, thaw settlement of oil production platforms is a serious hazard in areas containing shallow sub-sea permafrost. (There are also environmental concerns as to the effects of widespread thawing.) The dredging of shipping lanes may be difficult or impossible at locations where ice-bonded sediments occur close to the surface. For similar reasons, the excavation of pipeline trenches may also be influenced by shallow sub-sea permafrost distribution. Further, degraded permafrost appears to be related to shallow gas hydrate occurrences, the latter is both a possible resource and a hazard to drilling. With regard to exploration, it is important to recognize permafrost as a geological factor that often hinders the most commonly used geophysical exploration method in this area, the seismic method.

1.2: Sub-sea geophysical methods in Arctic areas.

By far the most widely used exploration strategy for obtaining geological information in Arctic sub-sea areas is the reflection seismic survey and interpretation fol-

lowed by the drilling and logging of exploratory wells and the subsequent correlation of the two kinds of data. The occurrence of permafrost can make reflection seismic interpretation difficult. Frequent and unusual natural phenomena such as multiple reflectors, ice lenses, and patchy low velocity zones degrade the seismic section. The occurrence within permafrost of lenticular zones of liquid gas hydrate which attenuate seismic waves also result in a loss of information. O'Conner (1980) states "...It was concluded that acoustic identification of specific geologic units appears to be possible, except where ice scouring, permafrost and/or the presence of shallow gas interfere with acoustic stratigraphy. ...".

The seismic refraction method, the geophysical method routinely used to identify permafrost beneath the sea floor, has a severe limitation. The high contrast in velocity between the seismically rigid permafrost and the softer sedimentary environment makes the determination of the depth to the top of permafrost easy. However, the method does not see the lower interface because of the velocity reversal. Despite this limitation seismic is still the most effective mapping technique in sub-sea Arctic regions.

Other geophysical methods have been tried offshore in the north with limited success. Corwin (1983) used a galvanic (DC) electrical resistivity method whereby a standard Schlumberger array is towed behind a ship. The method seems to have been reasonably successful in water depths of a few metres. In deeper water, the high electrical conductivity of the sea water inhibits measurement of sub-sea resistivities. The array, like all standard resistivity arrays, is sensitive to the value of the resistivity reflection coefficient, an expression which is close to unity for all crustal resistivities. Further, as a direct result of the work on anisotropy described later in this report, it can be argued that static resistivity methods are virtually useless for permafrost mapping anywhere. The presence of anisotropy, which is totally undetectable by the method, can cause typically a vertical scale error of a factor of 1.5 to 2.

Electromagnetic methods, particularly the large loop transient technique, have proven to be capable of resolving the base of offshore permafrost. However, the successful experiments have been conducted either on sea ice over very shallow water, or on artificial islands. The problem is the attenuation of electromagnetic signals by the conductive sea water. The methodology can be improved by locating the systems on the sea floor. The choice of method then becomes a trade-off between the one or

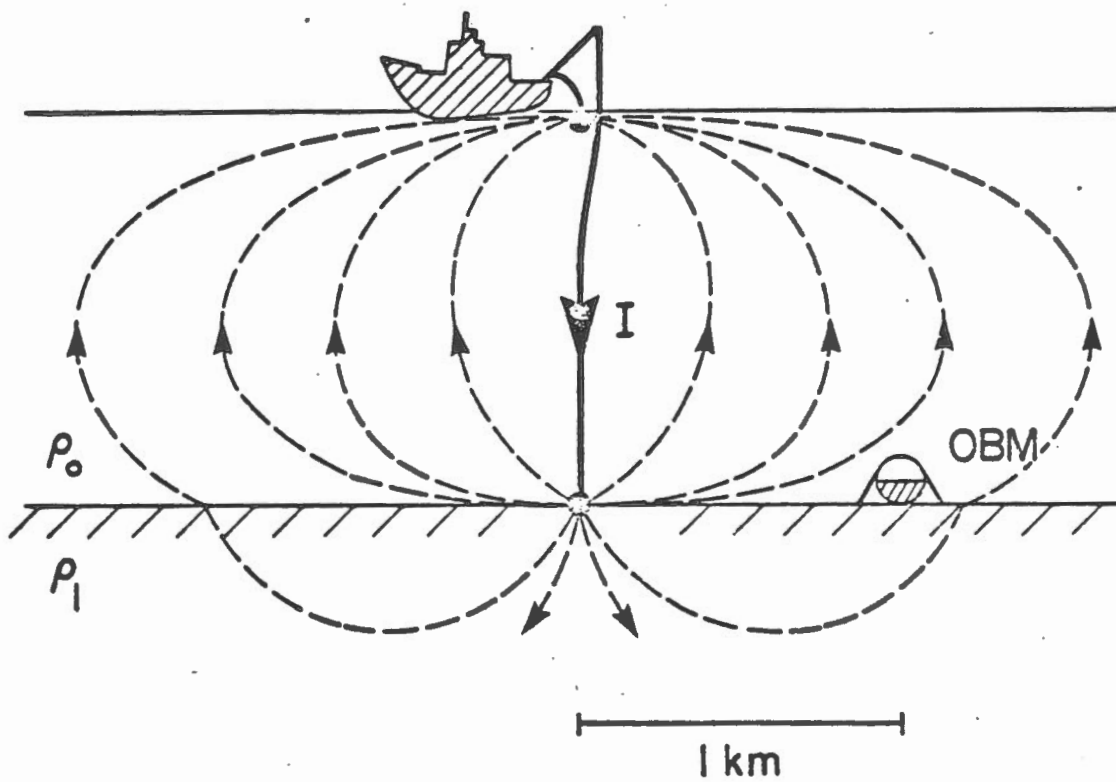
two logistically feasible methods and the optimum ones from the point of view of physics. The MOSES method, designed specifically for crustal sounding beneath a sea many hundreds of metres deep, was the result of one such compromise. It is described here in its original form.

1.3: MOSES

Any controlled source method requires a transmitter of electrical energy and a receiver to detect the presence of the electromagnetic field. In our method, the transmitter is a vertical, long-wire bipole, extending from the sea surface to the sea floor. A commutated current is generated on the ship and is fed to two large electrodes: one at the sea surface, the other at the end of a long insulated wire. The current return path is through the sea as illustrated in Figure 1.3.1. The receiver is a self-contained micro-processor controlled magnetometer located on the sea floor. The total horizontal component of the static, commutated magnetic field generated by the current system is measured over a range of horizontal transmitter-receiver separations and a range of suitable frequencies.

The acronym MOSES which has been coined for the method stands for Magnetometric Off-Shore Electrical Sounding. The choice of MOSES is actually quite appropriate because the system geometry is carefully designed to remove many of the adverse effects of the relatively conductive sea water. In particular, accurate estimates of sea floor resistivity are possible because the data are proportional to the transmitted current from the source into the crustal material. Resistivity sounding at sea with any standard array does not generate data sensitive to sediment resistivity unless unreasonably large separations are used. Short array spacings yield only the value of the resistivity reflection coefficient which is close to unity for all crustal resistivities. In contrast, our method measures the resistivity *transmission* coefficient which is inversely proportional to crustal resistivity.

If we apply Ampere's circuital law to a horizontal circuit on the sea floor centered at the base of the current bipole then the total current flow, for a uniform layered earth, has axial symmetry about a vertical axis defined by the bipole (see Figure 1.3.1). The azimuthal magnetic field is constant in magnitude around the Ampere circuit and, by the theorem, is due only to the current which crosses the plane of the circuit, i.e. to the current which enters the crust. This current may be shown to be proportional to the ratio of sea resistivity to the crustal resistivity. Consequently, the associated



MOSES

Figure 1.3.1: The MOSES method.

magnetic field is a direct measure of crustal conductivity. The results of numerical computations (Edwards et al., 1981) show that the field strength is small. However, the field need only be measured to an accuracy of say 10 percent to obtain the crustal conductivity to the same degree of accuracy. Estimates of crustal conductivity are obtained at all transmitter-receiver separations, the larger separations averaging to greater depth. Apparent resistivity curves similar to standard Schlumberger sounding curves may be constructed as an aid to layered earth interpretation. And the method, unlike the purely electromagnetic methods, is equally sensitive to conductive and resistive zones.

The measurements of the magnetic field as a function of frequency as well as separation enables MOSES data to be interpreted in terms of not only mean resistivity and thickness of a buried zone but of also the anisotropic properties of the zone. This makes the method particularly attractive for Arctic surveys.

The method has been used successfully on a number of occasions and some of the most recent results include the Bute Inlet sounding (Edwards et al., 1985) and two soundings in the middle of the Juan de Fuca ridge (Nobes et al., 1985). The Bute Inlet sounding, conducted in a water depth of 640 meters, determined the resistivity and thickness of a sedimentary section as $1.9 \Omega\text{m}$ and 560 meters respectively. Parameter eigenvector analysis gave an estimate of the error at 9.2 percent. The sediment at the first site in the Juan de Fuca ridge was determined as having resistivity and thickness of $0.82 \Omega\text{m}$ and 1700 meters respectively. The second site proved to have only a thin sedimentary cover and the resistivity of the basement was determined to be on average $10 \Omega\text{m}$ to a depth greater than 1500 meters. Presently, Peter Wolfgram (PhD Student) is interpreting data from a small scale (MINI-)MOSES sounding that was conducted over ocean floor sulphides in the Endeavour segment of the Northern Juan de Fuca ridge.

2. Factors influencing marine sediment resistivity

The object of this section is to provide justification for the study of certain theoretical problems and guidelines for subsequent numerical modelling and experimental design.

2.1: Archie's formula

The electrical resistivity of an unconsolidated, unfrozen sediment composed of non-conductive minerals depends primarily on the resistivity of the pore fluid and the porosity of the sediment. The rock conducts electricity because of the movement of ions (electrolytic conduction) in the fluid filled pores. The empirical relation between formation resistivity ρ_f and porosity ϕ (fractional pore volume) is given by Archie's formula

$$\rho_f = A\phi^{-m}S^{-n}\rho_w. \quad (2.1.1)$$

where A is a constant in the range $0.5 < A < 2.5$, S is the fraction of pores filled with water, n is the saturation exponent, ϕ is the porosity, ρ_w is the resistivity of the pore water. The exponent m is a constant which depends mainly on the geometry of the pore spaces and is called the cementation or formation factor.

Shallow marine sediments are completely saturated with water consequently the saturation factor S is unity and the equation simplifies to

$$\rho_f = A\phi^{-m}\rho_w. \quad (2.1.2)$$

The porosity of marine sediments can vary from as much as 0.8 at the sea floor to as little as 0.1 at large depths. Since in the limit as ϕ approaches 1, ρ_f goes to ρ_w , and given that ϕ varies greatly for the case of marine sediments, it is reasonable to assume that A is unity (Jackson et al., 1978). Thus we are now left with only three parameters which determine the resistivity of the sea sediment, ϕ , m and ρ_w .

The formation factor m depends on the shape of the particles in the rock. In a study of artificial samples, Jackson et al. (1978) found that m increased from 1.2 for spheres to 1.9 for platy shell fragments, while for sands m fell between 1.4 and 1.6. They also discovered that particle size has very little effect on the formation factor.

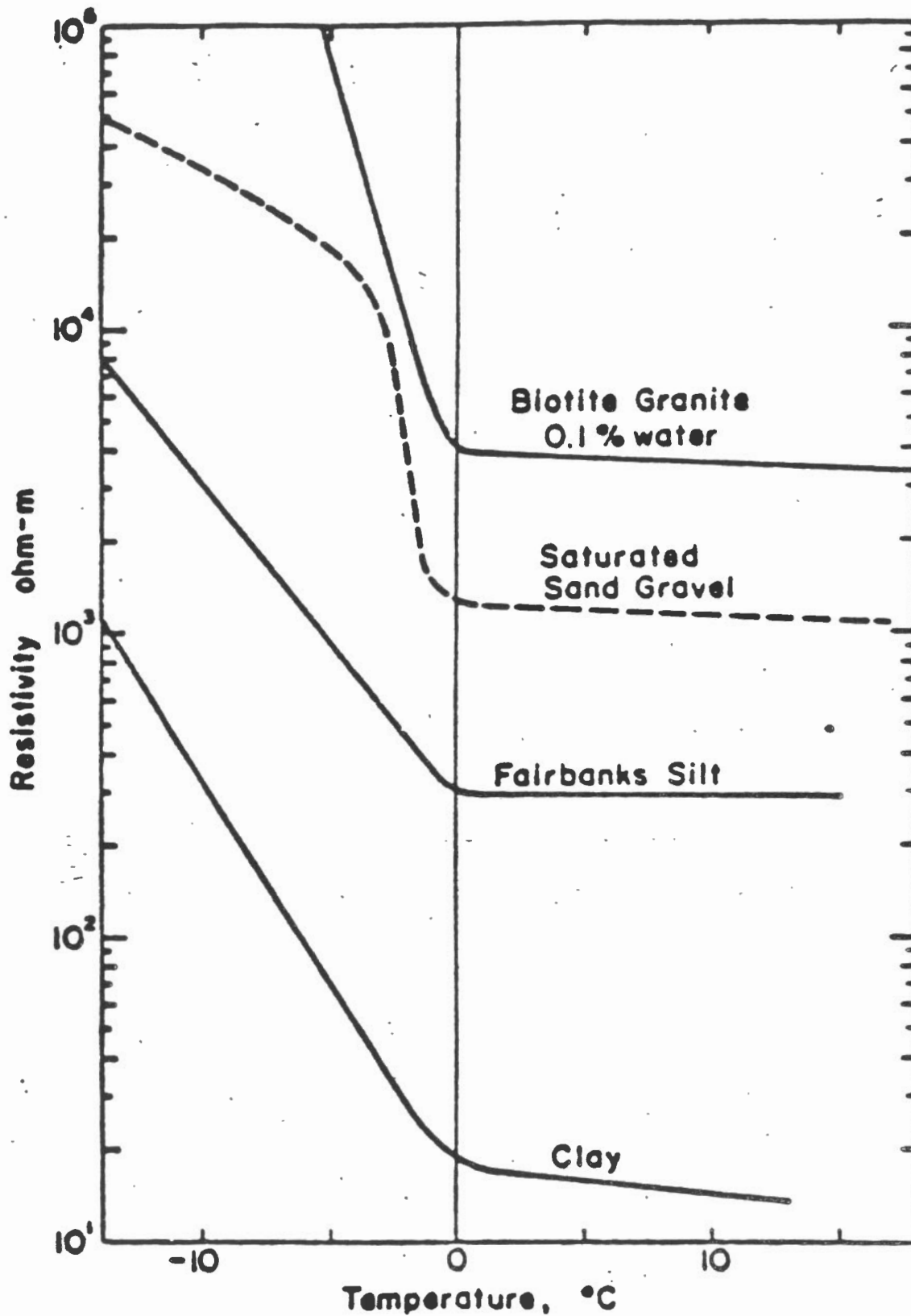


Figure 2.1.1: Resistivities for several soils and one rock type as a function of temperature (after Hoekstra, Sellman and Delaney, 1975).

In-situ measurements of sediment formation factors for the shallow-sea, near-shore environment range between 1.5 and 3.

The conduction in water is almost entirely electrolytic and consequently ρ_w is a function of the number of ions, their charges, and their mobility. Generally, the mobility is independent of the type of ion since it depends principally on the collision rate which is similar for most molecules. The charge, however, can vary depending on the valence of the ion - for example $(Mg)^{++}$ has the same conductive effect as $(Na)^+$, but at half the molar concentration. The number of ions dissolved in the water is influenced by the type of rock and in the majority of marine sediments the two dominant species are $(Na)^+$ and $(Cl)^-$.

The mobility and concentration of ions are both dependent on the temperature of the fluid. A rise in temperature will increase the average molecular velocity and hence the mobility of ions is greater. For a wide range of temperatures, Becker et al. (1982) have suggested the empirical rule

$$\rho_w = (3.0 + T/10)^{-1}, \quad (2.1.3)$$

for the resistivity of sea water, where T is the temperature in degrees celcius. Measured resistivities of pore water samples from the Arctic seem to be consistent with the average pore water sample being sea water. Given these formation factor and pore fluid resistivity values, the resistivities of unfrozen Arctic marine sediments would be expected to range from .5 to 4 Ωm , with the most typical value being 2 Ωm .

If the temperature of a sediment is lowered to the point where some of the water begins to freeze, then the ionic mobility is greatly reduced. In contrast, the ion concentration in the remaining fraction of unfrozen liquid increases. There is a reduction of the effective porosity and an increase in the salinity of the fluid. The resistivity of the rock rises rapidly with decreasing temperature as very resistive ice blocks the continuity of the conductive pathways in the material. Some examples of the overall variation of resistivity with temperature are given in Figure 2.1.1. The absolute resistivities and temperatures shown are not relevant to the marine environment because the samples are saturated with ground water rather than sea water. In the case of saturated sand gravel there is an order of magnitude increase in resistivity for a 0 to -3 degree change in temperature. The clays and silts have a resistivity that increases relatively slowly with decreasing temperature. This is attributed to

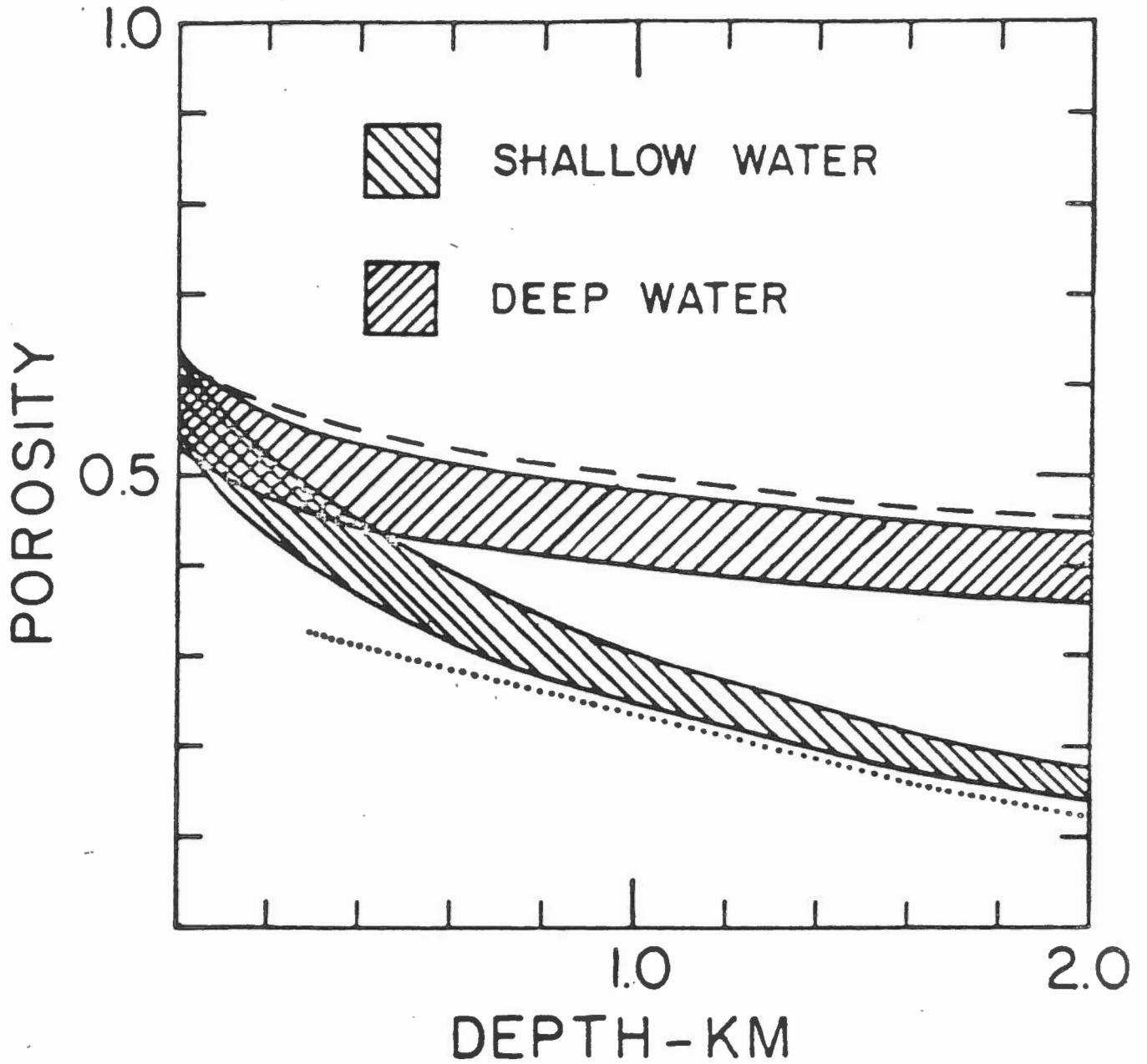


Figure 2.2.1: Porosity of shallow and deep water sediments plotted against depth (after Nafe and Drake, 1957).

the large ion exchange capacity of clays. It would appear that the negatively charged surfaces of clay particles attract cations in the fluid producing a local increase in the concentration of ions close to the clay surface. The higher concentration of dissolved ions prevents this water from freezing and hence provides a conductive path through the sediment. Since frozen clays can have a lower resistivity than unfrozen silts or sand gravel it is clear that resistivity measurements alone can not always identify permafrost, and some other geological information is necessary.

2.2: Porosity and resistivity variation with depth

There is precious little information available on this subject and it would appear that porosity-depth modelling of shallow marine sediments has been almost entirely neglected. Part of the problem is the lack of any kind of log. The standard drilling procedure requires the casing of the first 100 meters of drill hole in order to set up the blow out preventer and marine riser which permits the use of drilling mud.

Nafe and Drake (1957) describe one of the few studies which has attempted to relate porosity to seismic velocity with an empirical function. They examined the variation with depth of porosity, density, and seismic velocity in both shallow and deep water marine sediment. Their compilation of the variation of porosity with depth for average deep (greater than 3 km) and shallow water (less than 200 m) is shown in Figure 2.2.1. The dashed line represents data obtained from artificial compaction of sediments while the dotted line is a combination of data from Venezuelan and Kansan bore holes.

The porosity of shallow water sediment is considerably less than that of deep water sediment because the effective stress is greater for shallow water. (The effective stress, a function of depth, is the stress produced by the weight of rock above minus the hydrostatic pressure of the pore fluid; consequently, deep water reduces the effective stress.) The porosity curve for shallow water is replotted in Figure 2.2.2 with logarithmic and linear scales for porosity and depth respectively. The straight line suggests an exponential variation of porosity with depth for shallow water marine sediments.

$$\phi = \phi_0 \exp(-sz) \quad (2.2.1)$$

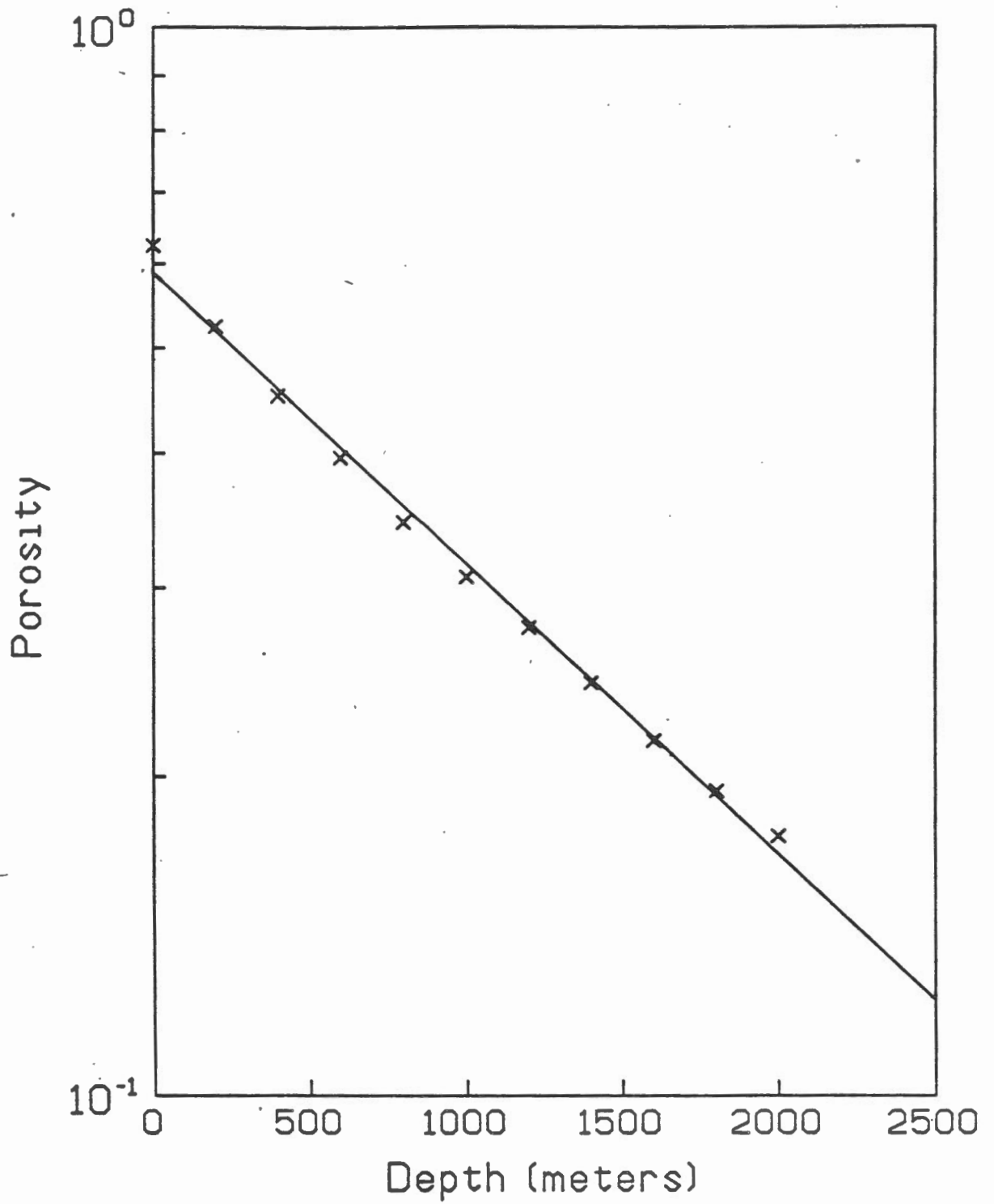


Figure 2.2.2: The logarithm of the porosity of shallow water sediments plotted against depth.

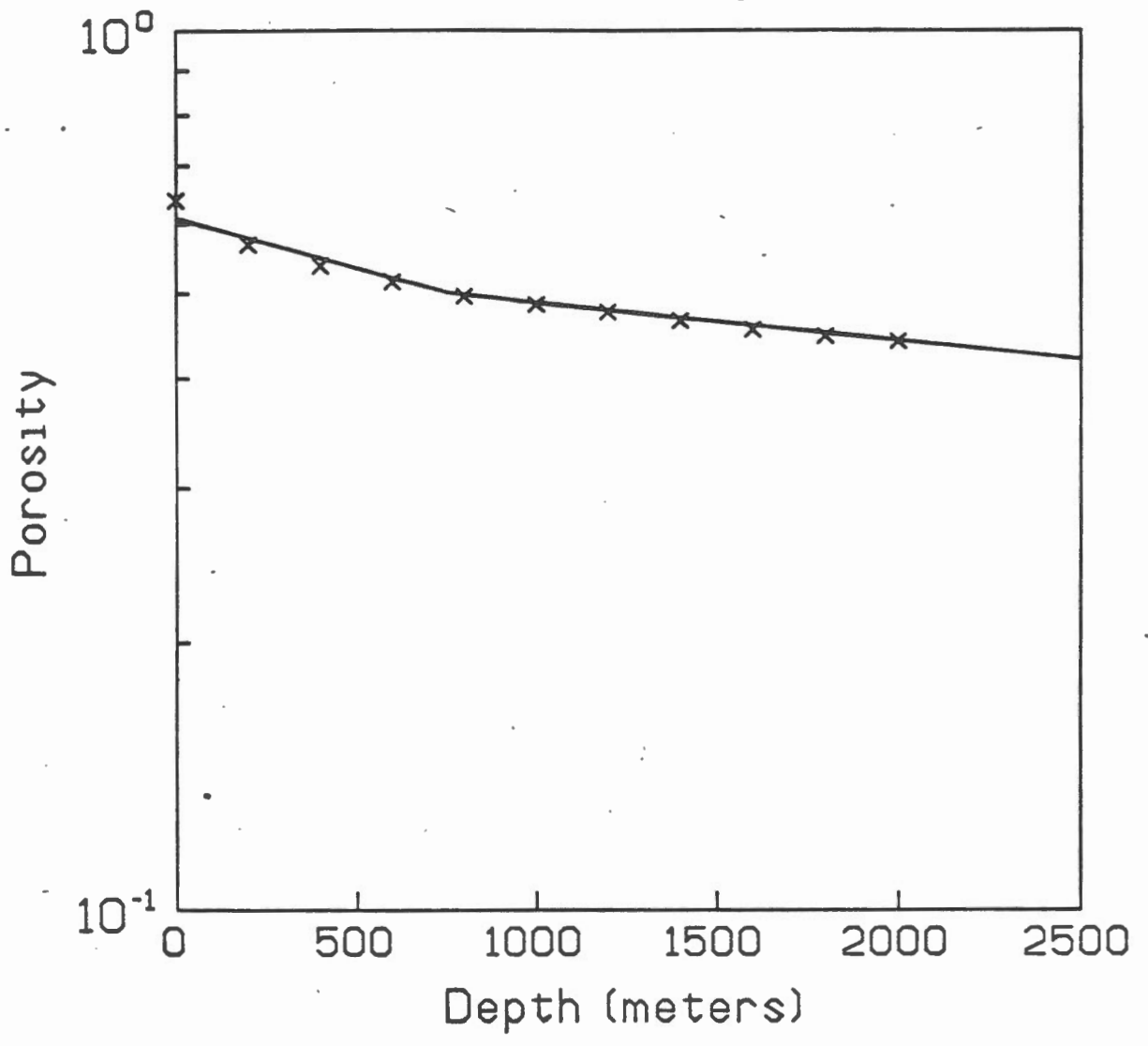


Figure 2.2.3: The logarithm of the porosity of deep water sediments plotted against depth.

where decay constant $s \approx 6.15 \times 10^{-4} m^{-1}$ is determined from Figure 2.2.2, and ϕ_0 is the porosity at $z=0$. The porosity of the deep water sediment does not behave in a similar manner. However, two piecewise continuous exponential functions appear to fit the data very well, as shown in Figure 2.2.3.

This limited data base indicates that an exponential decrease in porosity with depth is an extremely good representation of the behaviour marine sediments. Consequently, some reduction in the number of parameters in a layered one-dimensional model representing the sediment may be achieved by allowing an exponential variation in porosity within the layer, rather than the more elementary constant porosity.

The corresponding resistivity variation may be obtained by substituting the porosity-depth relation (2.2.1) into Archie's rule. There results

$$\rho_f = [\phi_0 \exp(-sz)]^{-m} \rho_w \quad (2.2.2)$$

or

$$\rho_f = \phi_0^{-m} \rho_w \exp(\nu z) \quad (2.2.3)$$

with decay constant ν equal to the product of formation factor m with the porosity decay constant s . Thus an exponential decrease in porosity causes a corresponding exponential increase in resistivity. When forward modelling the MOSES response of a layered medium at the static limit, an exponential variation of resistivity with depth within a given layer is no more difficult to programme than the constant resistivity case.

2.3: Transverse isotropy.

Resistivity dependence upon direction is called anisotropy or aeolotropy and it is the overall result of the microscopic phenomena of grains and their orientation combined with macroscopic effects such as alternating sedimentary layers. The scale length of anisotropy is related to the resolution of the sounding method - for example, if the resolution is 10 meters and alternating layers of differing conductivity occur at one meter intervals, then this layering would be blurred and would become part of the anisotropy of the material. Unfortunately, the term anisotropy is used loosely to mean *transverse isotropy* which is the particular case of anisotropy when the two

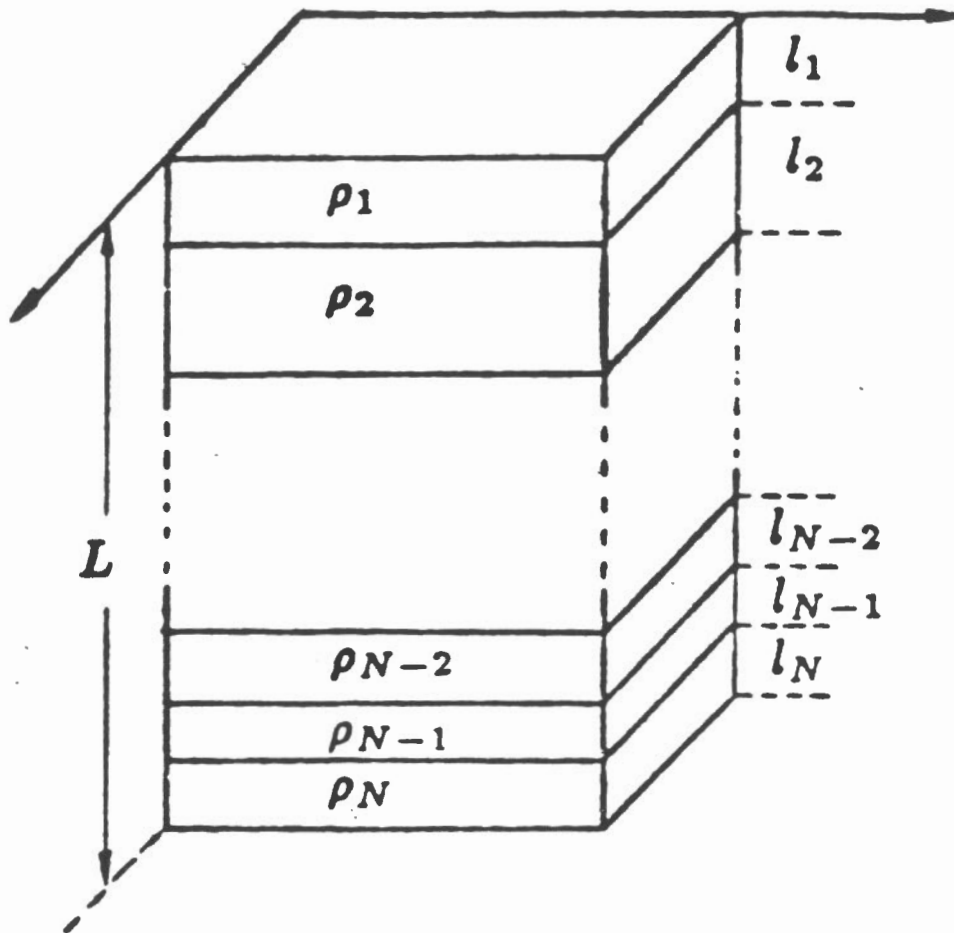


Figure 2.3.1: A horizontally stratified medium.

horizontal elements of the diagonal resistivity tensor are equal but different from the vertical element.

Since most rocks and minerals are poor conductors, electrical current is passed by electrolytic conduction in the saturated pores. Rock grains which make up sediments tend to have a platy structure and lie in bedding planes. Current paths that are perpendicular to bedding planes are more resistive than current paths which run parallel; consequently the resistivity is directionally dependent. This type of anisotropy is called micro-anisotropy.

Macro-anisotropy, on the other hand, is the macroscopic effect of the repeated occurrence of two different facies which form thin horizontal beds. (Here, *thin* is interpreted as being significantly smaller than the resolution of the geophysical method at the depth of the bed) The case of a horizontally stratified medium is illustrated in Figure 2.3.1. In the horizontal direction, the *admittances* $\frac{l_i}{\rho_i}$ of horizontal layers in *parallel* add together to produce $\frac{L}{\rho_h}$, the total admittance. However, in the vertical direction, it is the *impedances* $\rho_i l_i$ of the horizontal layers in *series* which add to give the total impedance $\rho_v L$; consequently the vertical and horizontal resistivities, for the block of material, are not the same. There results

$$\frac{L}{\rho_h} = \sum_{i=1}^N \frac{l_i}{\rho_i}, \quad (2.3.1)$$

and

$$\rho_v L = \sum_{i=1}^N \rho_i l_i. \quad (2.3.2)$$

The coefficient of anisotropy f and the mean resistivity ρ_m are defined as

$$f = \sqrt{\frac{\rho_v}{\rho_h}}, \quad (2.3.3)$$

and

$$\rho_m = \sqrt{\rho_v \rho_h}. \quad (2.3.4)$$

The coefficient of anisotropy is by definition always greater than or equal to one. Macro-anisotropy ($1 < f < 3$) is usually much larger than micro-anisotropy

($1 < f < 1.2$), except in extreme cases, so that the resolution of the geophysical method is quite important and must be considered when modelling a resistivity-depth profile. Generally, the directional dependence of resistivity is more complicated than the simple transversely isotropic case. However, in horizontally stratified sediments this approximation works very well.

The overall effect of an anisotropic medium on a dc resistivity sounding is analogous to an elongation of the vertical axis. In transversely isotropic media, the depth of penetration of an electrical sounding is reduced because current prefers to flow horizontally rather than vertically; this effect causes anisotropic layers to have an apparent thickness which is greater than their true thickness. Fortunately, a quasi-static method such as MOSES can detect anisotropic effects from the phase information so that the problem does not produce any ambiguity.

3. Theory

3.1: The MOSES response of an anisotropic layered medium.

The theory of the MOSES method was partially developed by Edwards et al. (1981) and Edwards et al. (1984). The full layered-earth solution in a form suitable for direct implementation on a computer is given here. The geometry is illustrated in Figure 3.1.1. In the model, the sea is represented by a layer of uniform resistivity ρ_0 and thickness d . The planes $z = -d$ and $z = 0$ represent the sea surface and the sea floor respectively. Two current poles, a current sink (at time zero) labelled $C1$ of strength $-I(t)$ and a current source $C2$ of strength $+I(t)$ are located at $(0, 0, -d)$ and at the origin of the cylindrical coordinate system (r, ϕ, z) respectively. The poles $C1$ and $C2$ are joined by a straight insulated conductor which carries the current $I(t)$ from $C1$ to $C2$ to complete the continuity of current.

The crustal rock beneath the sea is divided in N regions, $N - 1$ homogeneous layers, where the thickness of the i^{th} layer is h_i , over a lower homogeneous halfspace. Each region is transversely isotropic. The vertical resistivity ρ_i^v of the i^{th} region is different from the horizontal resistivity ρ_i^h . As mentioned earlier, this form of anisotropy is usually a representation of a region in the crust composed of many thin homogeneous isotropic layers which cannot be resolved independently. On physical grounds, it is useful to introduce two other parameters. Maillet (1947) among others has shown that if a region is transversely isotropic then static electrical sounding methods, for example dc resistivity, can only detect the geometric mean resistivity ρ_i , defined by $\rho_i^2 = \rho_i^v \rho_i^h$. The orthogonal combination of the resistivities is the coefficient of anisotropy f_i , given by $f_i^2 = \rho_i^v / \rho_i^h$, a parameter which is always greater than or equal to unity. The effective sounding depth of a static electrical method into an anisotropic zone is inversely proportional to f . Put another way, an anisotropic zone always appears to be thicker than it actually is by a factor f when static data are analysed with a layered-earth isotropic modelling programme.

Let $I(t)$ vary as $I \exp(i\omega t)$. The electric current flow everywhere has axial symmetry about the z axis. Consequently, the magnetic field has only one component, in the ϕ direction, which may be written as

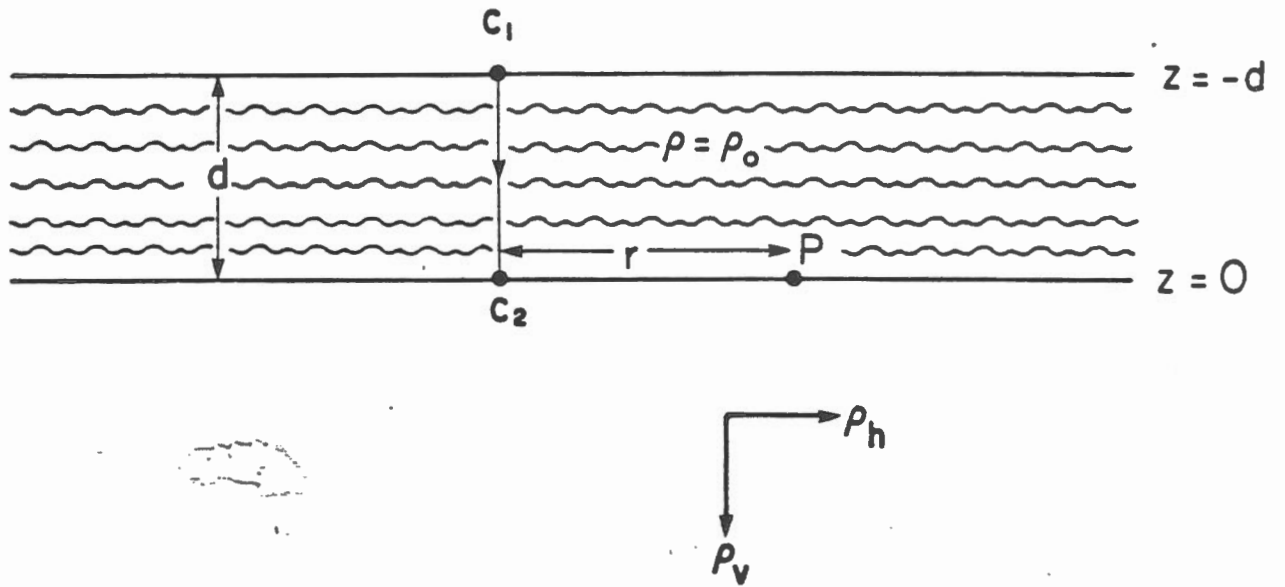


Figure 3.1.1: The geometry of the MOSES system.

$$\mathbf{B} = B(r, z) \exp(i\omega t) \hat{\phi}. \quad (3.1.1)$$

If the magnetic effects of displacement currents are neglected, the Helmholtz equation for B may readily be derived from Maxwell's equations as

$$\frac{\partial^2 B}{\partial r^2} + \frac{1}{r} \frac{\partial B}{\partial r} - \frac{B}{r^2} + \frac{1}{f^2} \frac{\partial^2 B}{\partial z^2} = \alpha^2 B, \quad (3.1.2)$$

where

$$\alpha^2 = i\omega\mu/\rho^v. \quad (3.1.3)$$

The magnetic field close to the wire is independent of z and from equation (3.1.2) is given by

$$B = (\mu\alpha_0 I/2\pi) K_1(\alpha_0 r), \quad (3.1.4)$$

where $\alpha_0^2 = i\omega\mu/\rho_0$, ρ^v being equal to ρ_0 in the sea, and K_1 is the modified Bessel function of the second kind of order 1. As α_0 tends to zero, expression (3.1.4) reduces to

$$B = \mu I/2\pi r, \quad (3.1.5)$$

the low-frequency static limit.

A Hankel transform pair relating any two functions $A(r; z)$ and $A(\lambda; z)$, may be defined as

$$A(\lambda; z) = \int_0^\infty r A(r; z) J_1(\lambda r) dr, \quad (3.1.6)$$

and

$$A(r; z) = \int_0^\infty \lambda A(\lambda; z) J_1(\lambda r) d\lambda. \quad (3.1.7)$$

where J_1 is a Bessel function of the first kind of order 1. The Hankel transform of the partial differential equation (3.1.3) yields the simple second order equation

$$\frac{d^2 B}{dz^2} - f^2 \lambda^2 B = f^2 \alpha^2 B. \quad (3.1.8)$$

A general solution of (3.1.8) in the sea is

$$B_0(\lambda; z) = (\mu I/2\pi)[F \exp(-\theta_0 z) + G \exp(\theta_0 z)], \quad (3.1.9)$$

where $\theta_0^2 = \lambda^2 + \alpha_0^2$ and f has been set to unity.

The Hankel transform of the particular integral (3.1.4) is

$$(\mu I \alpha_0/2\pi) \int_0^\infty r K_1(\alpha_0 r) J_1(\lambda r) dr = \mu I \lambda/2\pi \theta_0^2. \quad (3.1.10)$$

by standard integral 6.565/4 of Gradshteyn and Ryzhik (1965). The complete solution for the magnetic field in the sea is the sum of expressions (3.1.9) and (3.1.10) and is

$$B_0(\lambda; z) = (\mu I/2\pi)[F \exp(-\theta_0 z) + G \exp(\theta_0 z) + \lambda/\theta_0^2]. \quad (3.1.11)$$

and, in particular, the value of the field on the sea floor is

$$B_0(\lambda; 0) = (\mu I/2\pi)[F + G + \lambda/\theta_0^2]. \quad (3.1.12)$$

The electric field has two components in the vertical and radial directions, related to the single azimuthal component of the magnetic field by Ampere's law. In particular, the radial or tangential component E_r is given by

$$(\mu/\rho^h) E_r(r; z) = -\frac{\partial B(r; z)}{\partial z} \quad (3.1.13)$$

or equivalently, in the transform domain,

$$(\mu/\rho^h) E_r(\lambda; z) = -\frac{dB(\lambda; z)}{dz}. \quad (3.1.14)$$

The electric field E_{r0} in the sea is therefore

$$E_{r0}(\lambda; z) = (I \rho_0 \theta_0/2\pi)[F \exp(-\theta_0 z) - G \exp(\theta_0 z)]. \quad (3.1.15)$$

which, on the sea floor becomes

$$E_{r0}(\lambda; 0) = (I \rho_0 \theta_0/2\pi)[F - G]. \quad (3.1.16)$$

A boundary condition of the problem is that the magnetic field shall be zero on and above the surface of the sea. The boundary condition is easily established by

applying Amperes circuital law to a circular circuit drawn on the plane $z = d$, or on any plane above and parallel to it. The azimuthal and only magnetic component B is constant around the circuit, by symmetry: The current through the circuit is zero. Hence, the magnetic field must vanish. An explicit form of the boundary condition is obtained by setting $z = -d$ in expression (3.1.11). It is

$$0 = F \exp(\theta_0 d) + G \exp(-\theta_0 d) + \lambda/\theta_0^2. \quad (3.1.17)$$

Expressions (3.1.12), (3.1.16) and (3.1.17) may be combined to give an expression for $B_0(\lambda; 0)$ independent of the constants F and G and of the explicit value of the electric field. The expression does depend on the ratio of the electric and magnetic components B and E_r . It is

$$\lambda B(\lambda; 0) = \left[\frac{\mu I}{2\pi} \right] \left[\frac{1 - K}{2} \right] \left[\frac{1 - 2 \exp(-\theta_0 d) + \exp(-2\theta_0 d)}{1 - K \exp(-2\theta_0 d)} \right] \left[\frac{\theta_0^2}{\lambda^2} \right], \quad (3.1.18)$$

where $K = (Z_1 - \rho_0 \theta_0)/(Z_1 + \rho_0 \theta_0)$ is a reflection coefficient and Z_1 , in turn, is the ratio $\mu E_r(\lambda; 0)/B(\lambda; 0)$.

The parameter Z_1 has the dimensions of electric field, volts per metre, divided by magnetising field, amperes per metre, i.e. the dimensions of ohms. Consequently, it is referred to as an impedance. The impedance is continuous across all horizontal planes in the model, and the impedance at the top of the i^{th} crustal layer is designated the subscript i . It is possible to find Z_1 given the resistivities and thicknesses of the crustal layers, by means of a recurrence rule. The value of Z_1 is then substituted into expression (3.1.18) and the magnetic component $B(r; z)$ evaluated through the inverse Hankel transform (3.1.7).

A general solution of the differential equation (3.1.8) in the i^{th} layer is

$$B_i(\lambda; z) = (\mu I/2\pi)[U \exp(-\theta_i f_i z) + V \exp(\theta_i f_i z)]. \quad (3.1.19)$$

The corresponding radial component of the electric field is given by

$$\mu E_{r_i}(\lambda; z) = (\mu I \rho_i \theta_i/2\pi)[U \exp(-\theta_i f_i z) - V \exp(\theta_i f_i z)], \quad (3.1.20)$$

where $\theta_i^2 = \lambda^2 + i\omega\mu/\rho_i^2$ and ρ_i is the geometric mean resistivity. The impedance is the ratio of expressions (3.1.20) and (3.1.19). If its values at the top and bottom of the layer are Z_i and Z_{i+1} respectively, then

$$Z_i = \rho_i \theta_i \left[\frac{Z_{i+1} + \rho_i \theta_i \tanh(\theta_i f_i h_i)}{\rho_i \theta_i + \tanh(\theta_i f_i h_i) Z_{i+1}} \right]. \quad (3.1.21)$$

The impedance Z_1 may be derived recursively from rule (3.1.21) provided the value of Z_N is specified. As the thickness of the N^{th} layer is infinite, the value of $\tanh(\theta_N f_N h_N)$ is unity. Substituting this value in (3.1.21) gives the required impedance as $\rho_N \theta_N$.

If, in any layer i , the induction wavenumber α_i is allowed to approach zero, then θ_i approaches λ_i and the effects of anisotropy at the static limit are evident. The recursion through the anisotropic layer of mean resistivity ρ_i and thickness h_i/f_i , is the same as through an isotropic layer, of uniform resistivity ρ_i and thickness h_i .

3.2: Impedance transfer across a layer having an exponential increase in resistivity with depth

Nafe and Drake (1957), among others, have shown that the resistivity of some sea floor sediments increases exponentially with depth due to an exponential decrease in porosity. In this section, methods are described for determining the impedance transfer across an intermediate, isotropic horizontal layer, thickness h_i , whose resistivity $\rho_i(z)$ increases from b_i at the top of the layer to $b_i \exp(\nu_i/h_i)$ at the bottom. For the static dc case, the problem is analytic. However, the addition of electromagnetic induction terms makes the problem tractable only at a numerical level.

The inclusion of a continuous variation of resistivity with depth modifies the differential equation (3.1.8) and it becomes

$$\frac{d^2 B}{dz^2} + \frac{1}{\rho_h} \frac{d\rho_h}{dz} \frac{dB}{dz} - f^2 \lambda^2 B = f^2 \alpha^2 B. \quad (3.2.1)$$

If the medium is isotropic and the effects of frequency are negligible, then a more simple form is obtained which is

$$\frac{d^2 B}{dz^2} + \frac{1}{\rho} \frac{d\rho}{dz} \frac{dB}{dz} - \lambda^2 B = 0. \quad (3.2.2)$$

or, for the i^{th} layer with an exponential variation in resistivity, the constant coefficient form

$$\frac{d^2 B}{dz^2} + \nu_i \frac{dB}{dz} - \lambda^2 B = 0. \quad (3.2.3)$$

A general solution of this differential equation is

$$B_i(\lambda; z) = (\mu I / 2\pi) [M \exp(-\gamma_{1i} z) + N \exp(\gamma_{2i} z)], \quad (3.2.4)$$

where $\gamma_{1i} = [\lambda^2 + (\nu_i/2)^2]^{1/2} + \nu_i/2$, and $\gamma_{2i} = [\lambda^2 + (\nu_i/2)^2]^{1/2} - \nu_i/2$. The corresponding radial component of the electric field is given by

$$\mu E_{ri}(\lambda; z) = (\mu I \rho_i(z) / 2\pi) [M \gamma_{1i} \exp(-\gamma_{1i} z) - N \gamma_{2i} \exp(\gamma_{2i} z)]. \quad (3.2.5)$$

The impedance is the ratio of expressions (3.2.5) and (3.2.4). If its values at the top and bottom of the layer are Z_i and Z_{i+1} respectively, then

$$Z_i = \frac{b_i\{\gamma_{1i} + \gamma_{2i}\mathcal{E}\}Z_{i+1} + b_i^2 \exp(\nu_i d_i)\gamma_{1i}\gamma_{2i}\{1 - \mathcal{E}\}}{b_i \exp(\nu_i d_i)\{\gamma_{2i} + \gamma_{1i}\mathcal{E}\} + \{1 - \mathcal{E}\}Z_{i+1}} \quad (3.2.6)$$

where $\mathcal{E} = \exp\{-(\gamma_{1i} + \gamma_{2i})d_i\}$.

In order to include electromagnetic induction terms in the model the differential equation (3.2.1) must be solved numerically. For an exponential resistivity variation, it becomes

$$\frac{d^2 B}{dz^2} + \nu_i \frac{dB}{dz} - [\lambda^2 + \alpha^2]B = 0 \quad (3.2.7)$$

Equation (3.2.7) is of second order and thus requires two boundary conditions, however, only Z_{i+1} (the impedance at the bottom) is known. Application of a theorem attributed to Ricatti transforms this second order differential equation into a non-linear first order one.

$$\frac{d\Psi}{dz} + \Psi^2 + \nu_i \Psi = [\lambda^2 + \alpha^2] \quad (3.2.8)$$

where

$$\Psi = \frac{dB}{dz} B^{-1} \quad (3.2.9)$$

Equation (3.2.8) may be integrated numerically through layer. The initial value of Ψ at the bottom of the layer is related to the impedance there by

$$\Psi_{i+1}^i = -\frac{Z_{i+1}}{b_i \exp(\nu_i h_i)} \quad (3.2.10)$$

The final value of Ψ at the top of the layer may be converted back to an impedance with a similar rule.

3.3: The static MOSES response of a conductive, rectangular lamella.

The electrical conductivity of the earth beneath the sea does not just vary with depth. In many areas, lateral changes in conductivity are to be expected and indeed are evident from a study of the electrical logs of adjacent drill holes. A useful representation of a conductivity anomaly is a plate, or a more general lamella such as a warped or folded plate. A conductive anomaly within the earth channels an impressed source current and causes an anomalous magnetic field in its vicinity. In order to derive simply the form of the magnetic anomaly, and the equivalent apparent resistivity perturbation, the concept of a current dipole is introduced. The current dipole is a complete, infinitesimal, self-contained current system consisting of a wire element linking a point source and a point sink such that the combined current flow is everywhere divergence free. The current channelling into, out of and inside a conductive lamella may be represented by a distribution of current dipoles lying in the plane of the lamella.

A computer algorithm has been developed to compute the effect of a set of lamellae. A simplified version of the theory, that for a single vertical plate, is presented here.

The geometry of the single, vertical plate problem is illustrated in Figure 3.3.1. The plate lies in the y, z plane and has strike length and depth extent a and b respectively. The distance from the sea floor, the plane $z = 0$, to the top of the plate is h . The plate is offset a distance c from the base of the MOSES source bipole. The conductivity-thickness product S of the plate varies with position. The plate is located in a half-space crust of isotropic resistivity ρ_1 . Other parameters are as specified in section 3.1, except, for the static approximation, the angular frequency ω is set to zero.

The integral equation method of solving the static resistivity problem for a three dimensional body in a uniform host medium is well known (Dieter, Paterson and Grant 1969). The Fredholm equation of the second kind is set up in terms of the free charge on the surface of the body and solved for it. Surface integrals of the product of the charge and an appropriate Green's function yield the electric potential or the electric field anywhere in the medium. Gomez-Trevino and Edwards (1979) showed that the magnetic field in the medium could subsequently be derived through a surface integral provided the tangential electric field was first evaluated everywhere on the body. Their

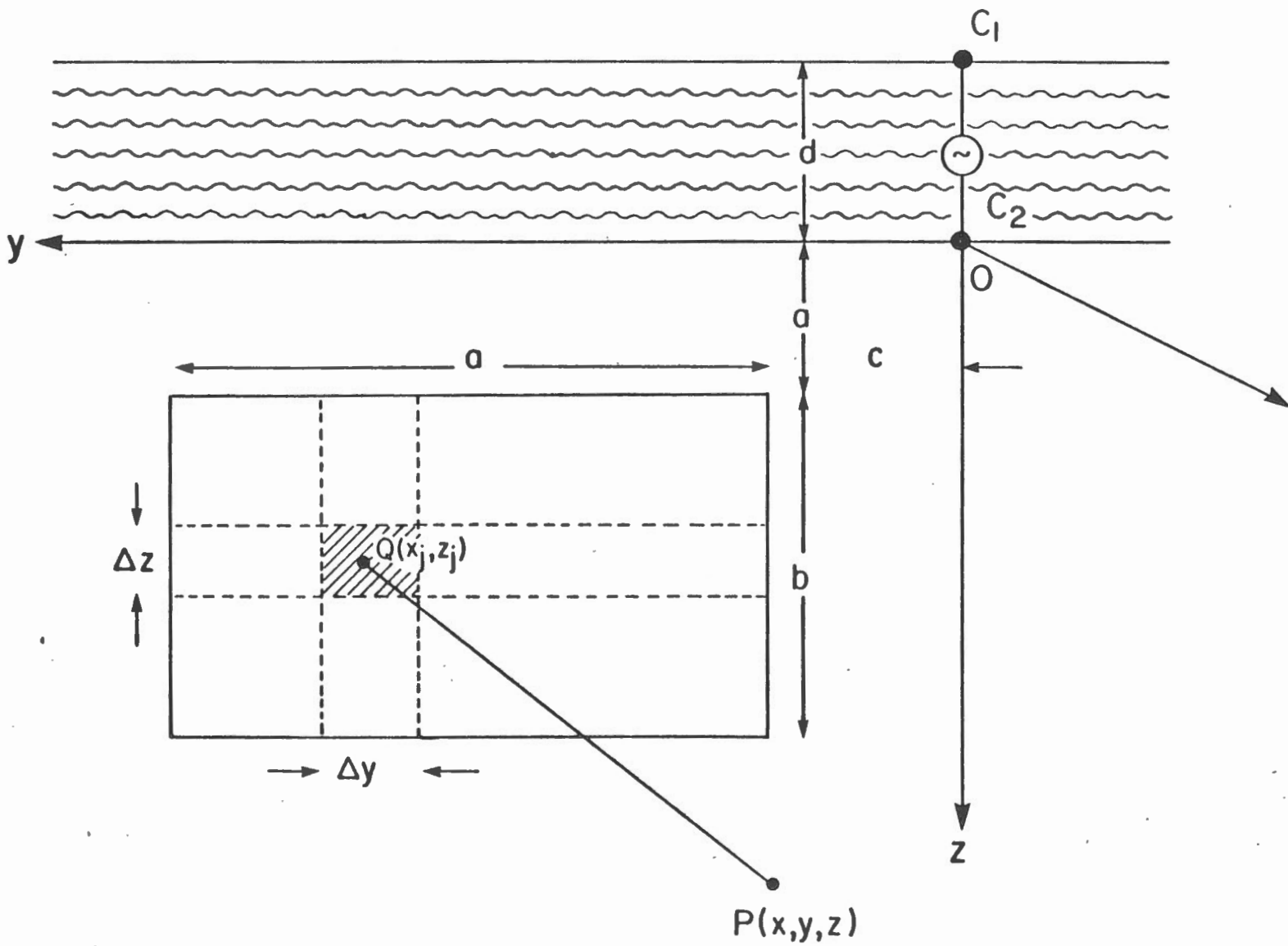


Figure 3.3.1: The geometry of the conductive rectangular plate buried beneath the sea in the vicinity of a MOSES bipole.

computation of the magnetic field in this manner is clearly a three stage process - charge, electric field, magnetic field. The method may be improved by solving the integral equation for a distribution of current dipoles in the plane of the plate. The current dipole, introduced by Stefanescu (1958), is a complete infinitesimal current system, a point source and a point sink linked by a current element such that the whole system is everywhere divergence free. The electric potential, the electric field and the magnetic field can be expressed as simple integrals over the dipole distribution, reducing the problem of computing any field to a two stage process. The alignments of the current dipoles in the plate are in the cartesian y and z directions.

The plate shown in Figure 3.3.1 is divided up into infinitesimal small rectangles of area $dy dz$ like the one shown in Figure 3.3.2. A total current I_y enters the rectangle along one edge and leaves along another forming a current dipole of moment m_y equal to $I_y dy$ by definition. The y -component of the surface current i_y in the rectangle due to the uniform flow is I_y/dz or equivalently $m_y/dy dz$. It is the total surface current because the plate has infinitesimal thickness so that the contribution to the total current from any source outside the plate is itself infinitesimal. It follows that the total y -component of the electric field within the rectangle is $m_y/dy dz S$. The orthogonal z -component of the surface current and electric field are defined in terms of the dipole moment m_x in a similar manner.

The integral equation is formed by equating the two components of the internal tangential electric field to the corresponding external electric field at the surface of the plate. The latter is simply expressed as a sum of the external field of the dipole distribution and the field of the exciting point source.

Let $P(y, z)$ be a test point on the surface of the plate. The external y -component of the electric field at P due to an infinitesimal current dipole at $Q(y_p, z_p)$ of moment $m_y(y_p, z_p)$ is

$$E_y^y(y, z) = (\rho m_y(y_p, z_p)/4\pi) \left[-\frac{1}{r^3} + \frac{3(y - y_p)^2}{r^5} \right], \quad (3.3.1)$$

where $r^2 = (y - y_p)^2 + (z - z_p)^2$. Written in terms of the surface current i_y by substituting for the moment m_y , the total y -component of the distribution of y -directed dipoles is

$$E_y^y(y, z) = (\rho/4\pi) \int_h^{h+b} \int_{-a/2}^{a/2} i_y(y_p, z_p) \left[-\frac{1}{r^3} + \frac{3(y-y_p)^2}{r^5} \right] dy_p dz_p. \quad (3.3.2)$$

Also, the same component at P due to the distribution of z -directed dipoles is

$$E_y^z(y, z) = (\rho/4\pi) \int_h^{h+b} \int_{-a/2}^{a/2} i_z(y_p, z_p) \left[\frac{3(y-y_p)(z-z_p)}{r^5} \right] dy_p dz_p. \quad (3.3.3)$$

The external y -component of the electric field at the point $P(y, z)$ due to the source bipole is

$$E_y^e(y, z) = (\rho_1/\mu) \int_0^\infty \lambda^2 B(\lambda; 0) \exp(-\lambda z) J_1(\lambda y) d\lambda. \quad (3.3.4)$$

where $B(\lambda; 0)$ is as given in expression 3.1.18, except, at the static limit, $\theta_0 = \lambda$ and $Z_1 = \rho_1 \lambda$.

An integral equation for the surface current i_y can now be formed by equating the internal and external tangential y -components of the electric field at P , it is

$$\begin{aligned} i_y(y, z)/S(y, z) = & (\rho/4\pi) \int_h^{h+b} \int_{-a/2}^{a/2} i_y(y_p, z_p) \left[-\frac{1}{r^3} + \frac{3(y-y_p)^2}{r^5} \right] dy_p dz_p \\ & + (\rho/4\pi) \int_h^{h+b} \int_{-a/2}^{a/2} i_z(y_p, z_p) \left[\frac{3(y-y_p)(z-z_p)}{r^5} \right] dy_p dz_p \\ & + (\rho_1/\mu) \int_0^\infty \lambda^2 B(\lambda; 0) \exp(-\lambda z) J_1(\lambda y) d\lambda \\ & + \{ \text{Appropriate Image Terms} \}. \end{aligned} \quad (3.3.5)$$

where the appropriate image terms are introduced to account for the effect of the sea water. If ρ_1 is larger than ρ_0 , it is often sufficiently accurate to include only one image term, arranged to cancel the dipole tangential electric components at the sea floor.

One can write down a similar integral equation for the z -component of the surface current, and the two equations should be solved simultaneously.

The simultaneous integral equations may be solved numerically in many different ways. The method of subsections is one of the simpler techniques. The plate is divided into $M \times N$ rectangles of finite size $[\Delta y \Delta z]$ equal to $[a/M b/N]$. The coordinates of

the centre of a given rectangle, defined by the indices i, j are (y_i, z_j) . The array S_{ij} specifies the conductance of each rectangle.

The two components of the surface current are selected to be constant over the area of a given rectangle and are written as $i_y(i, j)$ and $i_z(i, j)$. The integral equation for the y-component of the surface current in discrete form at one of $M \times N$ test points located at the centre of rectangle i, j is

$$\begin{aligned} i_y(i, j)/S_{ij} = & (\rho/4\pi) \sum_{n=1}^N \sum_{m=1}^M [i_y(m, n)H_y^y(i, j; m, n) + i_z(m, n)H_y^z(i, j; m, n)] \\ & + (\rho_1/\mu) \int_0^\infty \lambda^2 B(\lambda; 0) \exp(-\lambda z_j) J_1(\lambda y_i) d\lambda \\ & + \{The Image Terms\}, \end{aligned} \quad (3.3.6)$$

where the Green's functions $H_y^y(i, j; m, n)$ and $H_y^z(i, j; m, n)$ are

$$H_y^y(i, j; m, n) = \int_{z_n - \Delta z/2}^{z_n + \Delta z/2} \int_{y_m - \Delta y/2}^{y_m + \Delta y/2} \left[-\frac{1}{r^3} + \frac{3(y_i - y_p)^2}{r^5} \right] dy_p dz_p, \quad (3.3.7)$$

and

$$H_y^z(i, j; m, n) = \int_{z_n - \Delta z/2}^{z_n + \Delta z/2} \int_{y_m - \Delta y/2}^{y_m + \Delta y/2} \left[\frac{3(y_i - y_p)(z_j - z_p)}{r^5} \right] dy_p dz_p, \quad (3.3.8)$$

and the distance r is given by $r^2 = (y_i - y_p)^2 + (z_j - z_p)^2$. The Green's functions are trivial integrals which are never singular.

The corresponding matrix equation for the z-component of the surface current is

$$\begin{aligned} i_z(i, j)/S_{ij} = & (\rho/4\pi) \sum_{n=1}^N \sum_{m=1}^M [i_y(m, n)H_z^y(i, j; m, n) + i_z(m, n)H_z^z(i, j; m, n)] \\ & + (\rho_1/\mu) \int_0^\infty \lambda^2 B(\lambda; 0) \exp(-\lambda z_j) J_0(\lambda y_i) d\lambda \\ & + \{Different Image Terms\}. \end{aligned} \quad (3.3.9)$$

Equations (3.3.6) and (3.3.9) are solved simultaneously for the $2 \times M \times N$ unknown surface currents. The solution is stable for all values of S , even for the case of a perfectly conductive plate. Other integral equations often yield inaccurate answers at this limit. The equivalent current dipoles are obtained from the surface currents by multiplying each current by the area $\Delta y \Delta z$.

The magnetic field $\mathbf{B}(\mathbf{r})$ of a distribution of static current in a conductive medium of volume V may be written as

$$\mathbf{B}(\mathbf{r}) = k_m \int_V \frac{\nabla' \sigma(\mathbf{r}') \times \mathbf{E}(\mathbf{r}')}{|\mathbf{r} - \mathbf{r}'|} dv' \quad (3.3.10)$$

where $\mathbf{E}(\mathbf{r}')$ and $\sigma(\mathbf{r}')$ are the variation of the electric field and the conductivity through the medium respectively, and k_m is the ratio of the permeability μ_0 of free space to 4π . This modified form of the Biot-Savart law was derived by Edwards, Lee and Nabighian (1978). It is used extensively to compute MMR responses.

In our problem, the gradient of the conductivity vanishes everywhere except on the surfaces of the sea and on the two faces and four edges of the plate. The integral for the magnetic field is easily evaluated provided one precaution is taken. The zeroth-order contribution to the magnetic field at a field point $P(x, y, z)$ from the face of the plate looking in the positive x -direction is opposite in sign to the contribution from the other face. Consequently, the sum of the effects from the two faces should be obtained as a Taylor series expansion, which is the negative of the derivative of expression (3.3.10) w.r.t. the field coordinate x multiplied by the true thickness τ of the plate. The thickness τ appears in the analysis only through the conductance S or in terms like τ/ρ which are small compared with S and are subsequently neglected.

For many purposes, a sufficiently accurate representation of the magnetic field may be obtained by combining the two distributed current dipoles associated with a given rectangle into two infinitesimal current dipoles, of the same total moments, located at the centre of that rectangle, i.e. at points like $Q(y_i, z_j)$. Under this approximation, the magnetic fields the dipoles produce are very easily evaluated, by representing the dipoles by the line currents and current elements which generate the same magnetic field on the sea floor. The elementary currents for the simplification ρ_1 large compared with ρ_0 are shown in Figure 3.3.3. The computations are elementary applications of the Biot-Savart law.

For a current dipole of moment m_y equal to $I dy$ located at the point $Q(y_i, z_j)$ and

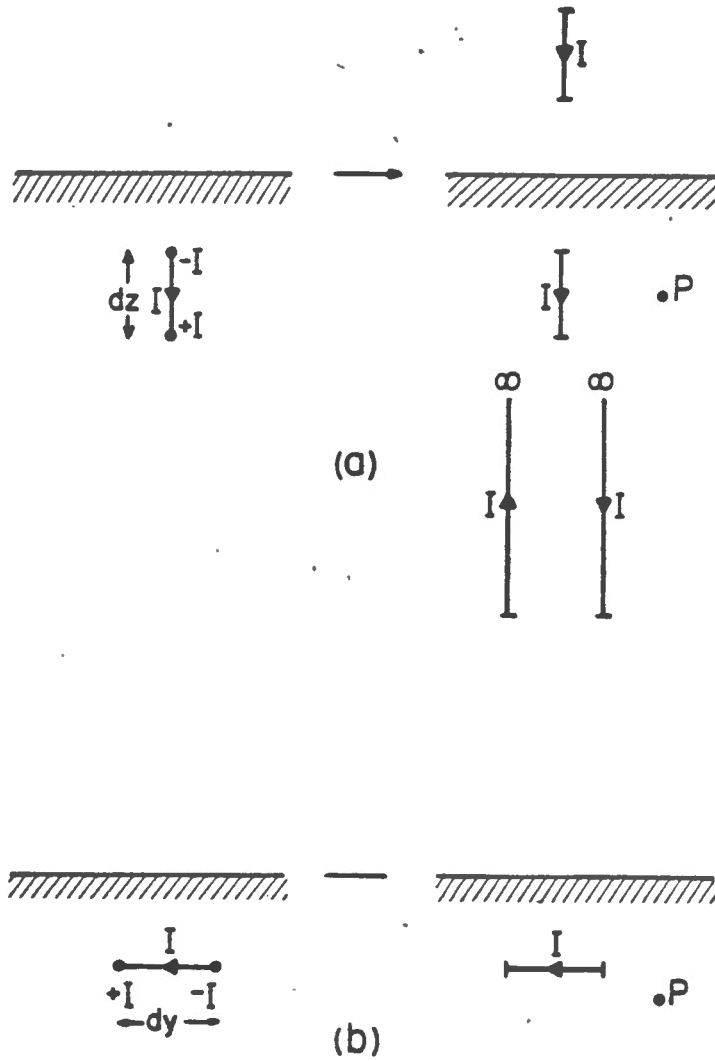


Figure 3.3.3: The buried vertical (a) and horizontal (b) current bipoles and the line current elements which generate the same magnetic field at the bottom of the sea.

directed in the positive y-direction, the magnetic components at the point $P(x, y, z)$ due the dipole itself are

$$B_x^{yd}(x, y, z) = k_m m_y(i, j) \left[\frac{z - z_j}{r^3} \right]; \quad (3.3.11)$$

$$B_y^{yd}(x, y, z) = 0; \quad (3.3.12)$$

$$B_z^{yd}(x, y, z) = -k_m m_y(i, j) \left[\frac{x}{r^3} \right], \quad (3.3.13)$$

where the length r is given by $r^2 = x^2 + (y - y_i)^2 + (z - z_j)^2$.

The additional components caused by the discontinuity in conductivity at the sea floor, or alternatively the contributions from the equivalent line currents in the upper half-space, are

$$B_x^{yo}(x, y, z) = -k_m m_y(i, j) \left\{ \left[1 - \frac{z + z_j}{s} \right] \left[\frac{x^2 - (y - y_i)^2}{t^4} \right] - \left[\frac{(y - y_i)^2 (z + z_j)}{t^2 s^3} \right] \right\}; \quad (3.3.14)$$

$$B_y^{yo}(x, y, z) = -k_m m_y(i, j) \left\{ \left[1 - \frac{z + z_j}{s} \right] \left[\frac{2x(y - y_i)}{t^4} \right] + \left[\frac{x(y - y_i)(z + z_j)}{t^2 s^3} \right] \right\}; \quad (3.3.15)$$

$$B_z^{yo}(x, y, z) = 0, \quad (3.3.16)$$

where the lengths s and t are given by $s^2 = t^2 + (z + z_j)^2$ and $t^2 = x^2 + (y - y_i)^2$ respectively.

The corresponding components for a z-directed dipole are more simple, they are

$$B_x^{zd}(x, y, z) = -k_m m_z(i, j) \left[\frac{y - y_i}{r^3} \right]; \quad (3.3.17)$$

$$B_y^{zd}(x, y, z) = k_m m_z(i, j) \left[\frac{x}{r^3} \right]; \quad (3.3.18)$$

$$B_z^{zd}(x, y, z) = 0, \quad (3.3.19)$$

and

$$B_x^{zo}(x, y, z) = -k_m m_z(i, j) \left[\frac{y - y_i}{s^3} \right]; \quad (3.3.20)$$

$$B_y^{zo}(x, y, z) = k_m m_z(i, j) \left[\frac{x}{s^3} \right]; \quad (3.3.21)$$

$$B_z^{zo}(x, y, z) = 0. \quad (3.3.22)$$

3.4: The electromagnetic MOSES response of a conductive, circular disc.

The perturbation of current flow by a three dimensional body at the static limit is readily computed. The complete quasi-static electromagnetic problem is not as straightforward. A conductive body influenced by a time varying electromagnetic field not only channels an impressed electric current but also responds to a magnetic field normal to its surface. A vortex current is set up within the body. Both the vortex and channelled currents generate secondary magnetic fields, and these fields interact with one another. The complete electromagnetic solution has to include the interaction terms, which makes the mathematics quite complicated, even for simple geometry.

A common simplification of the problem is to drop out the current channelling effect, a valid move provided the host medium is very resistive. Such an approximation for a MOSES bipole source is not possible. If the crust is made very resistive, no electromagnetic inducing field is transmitted beneath the sea. The logical alternative is to minimise the vortex effect, which is possible only for one type of conductivity anomaly - an axi-symmetric, thin conductive lamella whose axis of symmetry coincides with axis of the MOSES bipole. Vortex currents are not induced on the surface of the lamella as the only component of the magnetic field is, by symmetry, azimuthal and parallel to the surface. Since a lamella is infinitesimal in thickness, vortex current flow in a section through the lamella is negligible.

The simplest axi-symmetric lamella is the disc. Figure 3.4.1 shows a disc, radius a , conductivity-thickness product S , lying in the plane $z = h$ immediately beneath the MOSES bipole. The uniform resistivity of the crust is ρ_1 . The disc is divided up into infinitesimal concentric rings of radius s and thickness ds . A current $J(s)$ enters the ring along its inside edge and leaves along its outside edge. The radial surface current in the ring due to the flow is $J(s)/2\pi s$. It is the total surface current because the disc has infinitesimal thickness so that the contribution to the total current from any source outside the disc is itself infinitesimal. It follows that the total radial electric field within the ring is $J(s)/2\pi sS$. The integral equation is formed by equating this internal tangential electric field to the corresponding external electric field at the surface of the disc. The latter is simply expressed as a sum of the external field of the dipole distribution and the field of the exciting point source.

The azimuthal component of the magnetic field due the ring current dipole may be evaluated trivially by Amperes Circuital Law on the plane $z = h^-$ immediately

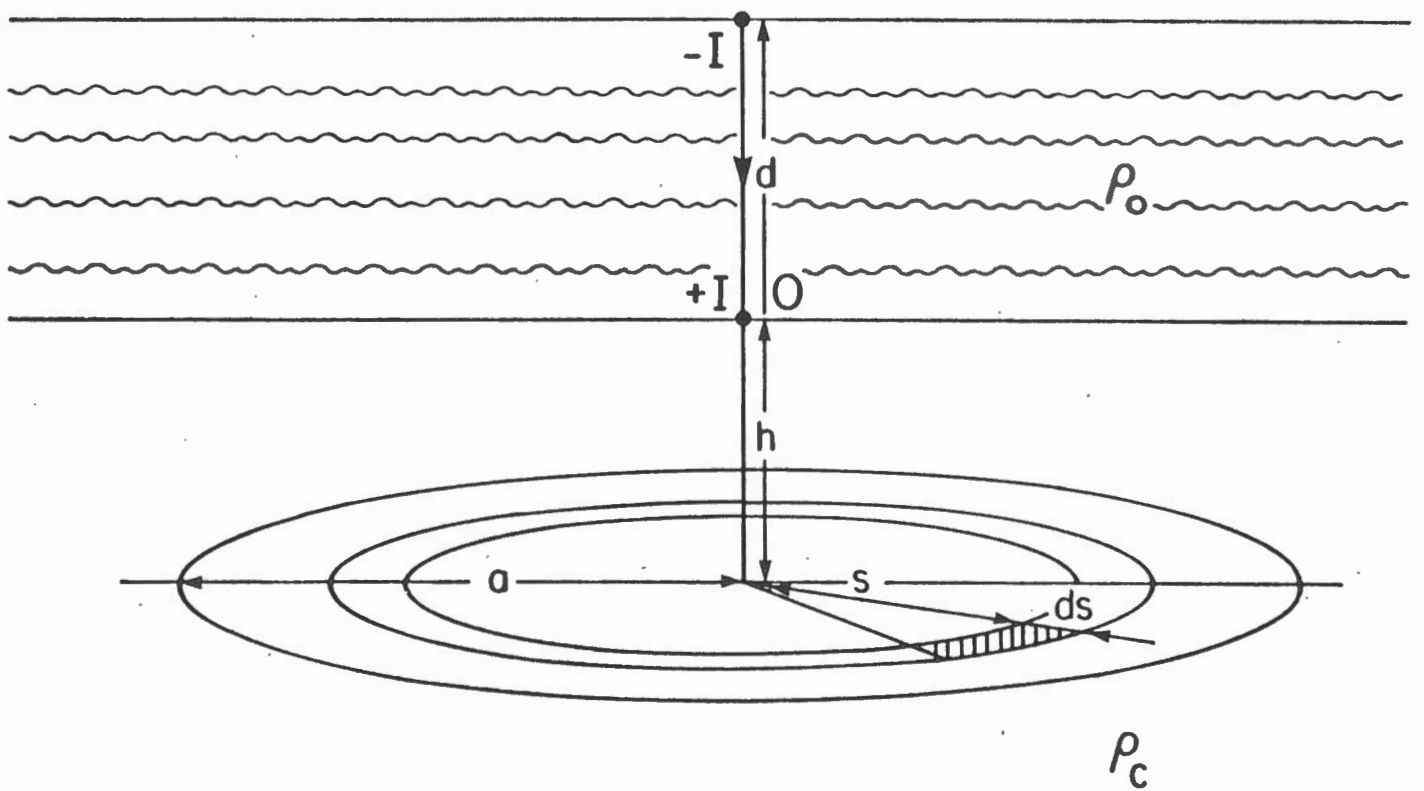


Figure 3.4.1: The geometry of the buried disc-like conductor located coaxially with the MOSES bipole.

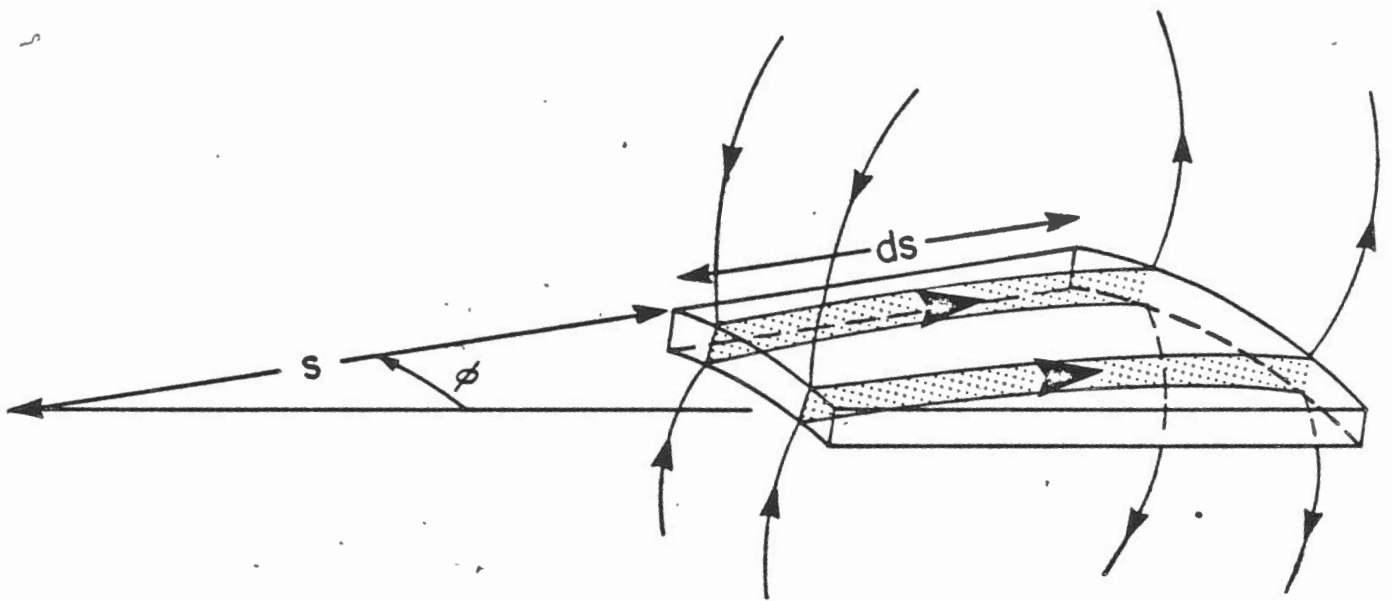


Figure 3.4.2: The elemental current dipole in the disc.

above the disc. For $s < r < s + ds$, the component is

$$B(r; h^-) = \mu J(s)/4\pi s, \quad (3.4.1)$$

while for all other values of r ,

$$B(r; h^-) = 0. \quad (3.4.2)$$

The Hankel transform (3.1.6) of the component is

$$B(\lambda; h^-) = \mu J(s) ds J_1(\lambda s)/4\pi. \quad (3.4.3)$$

Expression (3.4.3) may be multiplied by the continuation operator $\exp(-\theta_1(h-z))$ to obtain the form of the dipole field in the region $0 < z < h$. The complete solution in transform domain has also to include the effect of the sea layer. A general solution with coefficients obtained by solving the boundary value problem has to be added to the current dipole field. The final result is

$$B(\lambda; z) = (\mu J(s) ds/4\pi)[\exp(-\theta_1(h-z)) + R \exp(-\theta_1(h+z))]J_1(\lambda s), \quad (3.4.4)$$

where the reflection coefficient R is given by

$$R = [\rho_1 \theta_1 \tanh(\theta_0 d) - \rho_0 \theta_0]/[\rho_1 \theta_1 \tanh(\theta_0 d) + \rho_0 \theta_0]. \quad (3.4.5)$$

Let $P(r)$ be a test point on the surface of the disc. The external radial electric field $E_r^d(r)$ at P due to the ring dipole is obtained by differentiating expression (3.4.4) according to (3.1.14), setting z to the value h and taking the inverse transform according to (3.1.7). It is

$$E_r^d(r) = -(\rho_1 J(s) ds/4\pi) \int_0^\infty \theta_1 \lambda [1 - R \exp(-2\theta_1 h)] J_1(\lambda s) J_1(\lambda r) d\lambda. \quad (3.4.6)$$

and the field of all such rings is

$$E_r^d(r) = -(\rho_1/4\pi) \int_0^a J(s) ds \int_0^\infty \theta_1 \lambda [1 - R \exp(-2\theta_1 h)] J_1(\lambda s) J_1(\lambda r) d\lambda. \quad (3.4.7)$$

The external radial electric field at the point $P(r)$ due to the MOSES source current bipole is

$$E_r^e(r) = (\rho_1/\mu) \int_0^\infty \theta_1 \lambda B^e(\lambda; 0) \exp(-\theta_1 h) J_1(\lambda r) d\lambda, \quad (3.4.8)$$

where $\lambda B^e(\lambda; 0)$ is as in expression (3.1.18) with $Z_1 = \rho_1 \theta_1$.

The total external field is the sum of the fields given in (3.4.7) and (3.4.8).

The integral equation can now be formed by equating the internal and external tangential components of the electric field at P . It is

$$J(r)/2\pi r S = E_r^e(r) + E_r^d(r). \quad (3.4.9)$$

For a disc of finite radius a , no analytic solution of the integral equation exists. The equation may be solved numerically by the method of subsections. The disc is divided into N rings of finite thickness Δ equal to a/N . The radius of the centre of the i^{th} ring is s_i . On a physical basis, the total radial current $J(s_i)$, rather than the local radial electric field, is selected to be constant over the width of the i^{th} ring. The integral equation in discrete form for a set of N test points r_j is

$$J(r_j)/2\pi r_j S = E_r^e(r_j) + \sum_{i=1}^N J(s_i) H(i, j), \quad (3.4.10)$$

where the Green's function $H(i, j)$ is given by

$$H(i, j) = -(\rho_1/4\pi) \int_0^\infty \int_{s_i-\Delta/2}^{s_i+\Delta/2} J_1(\lambda s) ds \theta_1 \lambda [1 - R \exp(-2\theta_1 h)] J_1(\lambda r_j) d\lambda \quad (3.4.11)$$

Evaluation of the Green's function proceeds by first integrating out the dependence on s , which is a trivial task. The remaining Bessel integrals are integrated using the technique of Chave (1985). Finally, equation (3.4.10) is written as a matrix equation and solved. The solution is stable for all values of S , even for the case of a perfectly conductive disc. Other integral equations often yield inaccurate answers at this limit.

The computation of the anomalous magnetic component on the sea floor is a summation over the current dipoles. A reasonable approximation is the assumption that both the radial current $J(s)$ and the distance s are constant over the finite ring width Δ . Then, the component is

$$B(r; 0) = (\mu\Delta/4\pi) \sum_{i=1}^N J(s_i) \int_0^{\infty} \lambda [1 + R] \exp(-\theta_1 h) J_1(\lambda s_i) J_1(\lambda r) d\lambda. \quad (3.4.12)$$

The Hankel transform in (3.4.12) may be evaluated by any of the common convolution filter methods.

4. Numerical modelling and experimental design

The results presented in this section are highlights of ongoing research of the author and his students. Many of the ideas are in the process of being published separately. More detailed information can be provided by the author on request.

4.1: Analysis of an electrical log: macro-anisotropy

Through the courtesy of the Sohio Petroleum Company, a number of reliable deep induction logs of Arctic drill holes were obtained. All the logs showed the occurrence of permafrost in its various grades. A more detailed analysis of one of the logs is presented here to illustrate the importance of the phenomenon of macro-anisotropy.

The Sag Delta 3 well was drilled from an artificial island in two metres of water off the Sagavanirktok River Delta. A non-aliased form of the deep induction resistivity variation with depth from the well is reproduced in Figures 4.1.1a, 4.1.1c, 4.1.1e and 4.1.1g as the highly irregular, dashed curve. Notice the great range of resistivity values, from a low of less 1 Ωm to a high in excess of 300 Ωm . Notice also the wild excursions that occur in the depth range 230 to 500 feet. At first it was believed that these excursions were a figment of the drilling process, the local destruction of a permafrost zone by warm drilling fluid. However, a questioning of the staff of Sohio revealed that this is not the case. The log is a true representation of the variation of rock resistivity with depth. The zone is a zone of soft, partially-bonded permafrost typical of the area. The log shows two zones of harder permafrost around 575 feet and at a depth greater than 800 feet. The latter zone extends to 1400 feet (not shown).

Data collected with an electrical method at the surface of the earth clearly does not have the same resolving power as data collected down-hole. The inverted resistivity profile is a smoothed version of the down-hole log. The degree of smoothing is a complicated function of the electrical method, the profile, the depth, the type of model and the errors of measurement. For a given data set and profile, standard techniques are available to determine resolving kernels about a given depth. And, in general, there is a trade-off between accuracy of estimation of resistivity within a given zone and resolution.

To some extent, the effects of finite resolution can be simulated by filtering the down-hole log with a window whose width is prescribed and increases with depth.

Figures 4.1.1a to 4.1.1h
are in the pocket at the
end of the report.

The filtering has to be done with care. The quantities that should be averaged depend on the electrical method employed. For the electromagnetic methods, like the large-loop, transient method or the magnetotelluric method, it is the average admittance (expression 2.3.1) over the window that is required. The resistivity method sees the mean resistivity (expression 2.3.4), while the MOSES technique sees both the average admittance and the average impedance (expression 2.3.2). In general, the horizontal and vertical resistivities will not be the same and the process of averaging will cause macro-anisotropy to appear. The magnitude of the anisotropy for a section containing permafrost is very large.

Two kinds of distinct inverse methods are available to the interpreter. There is inversion to a continuous variation of resistivity with depth, and inversion to a layered medium. Simulated inversions of the first kind are shown in Figures 4.1.1a and 4.1.1c respectively. The downhole log is smoothed by a window whose equivalent width is 10 and 20 per cent of the depth respectively. Three curves are shown on each figure. They are the vertical, geometric mean and horizontal averaged resistivities respectively. On a logarithmic plot, the geometric mean resistivity appears to pass through the original data, while the upper vertical and lower horizontal resistivity curves appear to emphasise the resistive and conductive zones respectively.

The macro-anisotropy generated by the filtering process is plotted in Figures 4.1.1b and 4.1.1d respectively. The anisotropy seems to be caused by two relatively distinct effects, small scale resistivity excursions within a given zone and interfaces between frozen and unfrozen ground. The latter effect causes the largest anisotropies, which suggested to us a method of identifying interfaces from a continuous inversion. It is worth mentioning again the effect of anisotropy on a resistivity inversion is to change the depth scale by the value of the indeterminate anisotropy. Clearly, inversion of resistivity data collected over ground containing discrete zones of permafrost to a continuous resistivity profile is a hazardous exercise.

The filtering procedure generates smaller anisotropies if the model is layered. The results of averaging over suitably chosen layers are shown in Figures 4.1.1e to 4.1.1h respectively. As the number layers is increased and the depths to the interfaces between them are optimised, the overall anisotropy decreases. A scheme for inverting to a layered model has been devised which minimises the overall anisotropy.

There remains one open question from a study of the log. Is it possible to identify

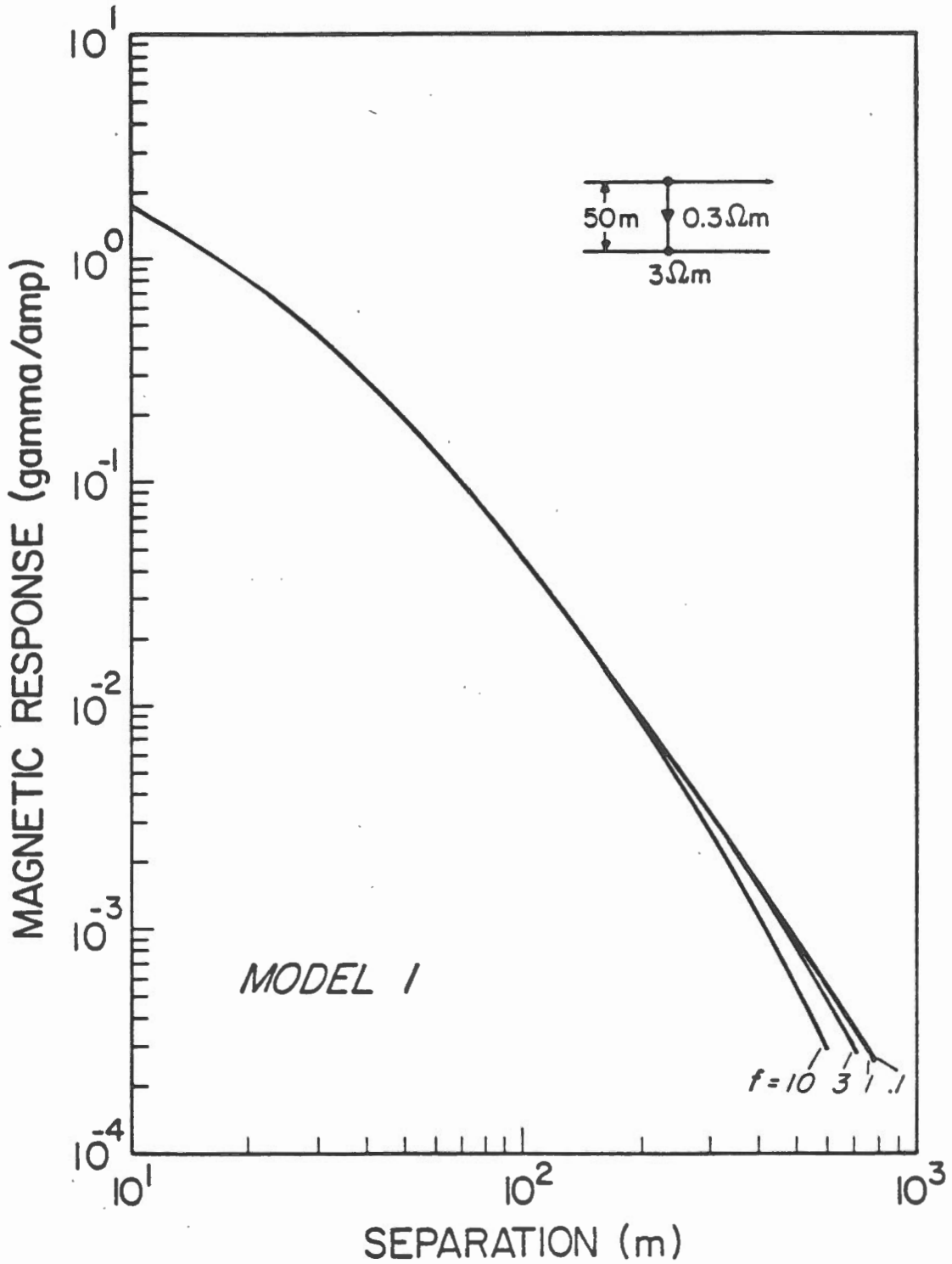


Figure 4.2.1a: Model 1 - magnetic field amplitude as a function of separation for the range of frequencies 0.1 to 10 Hz.

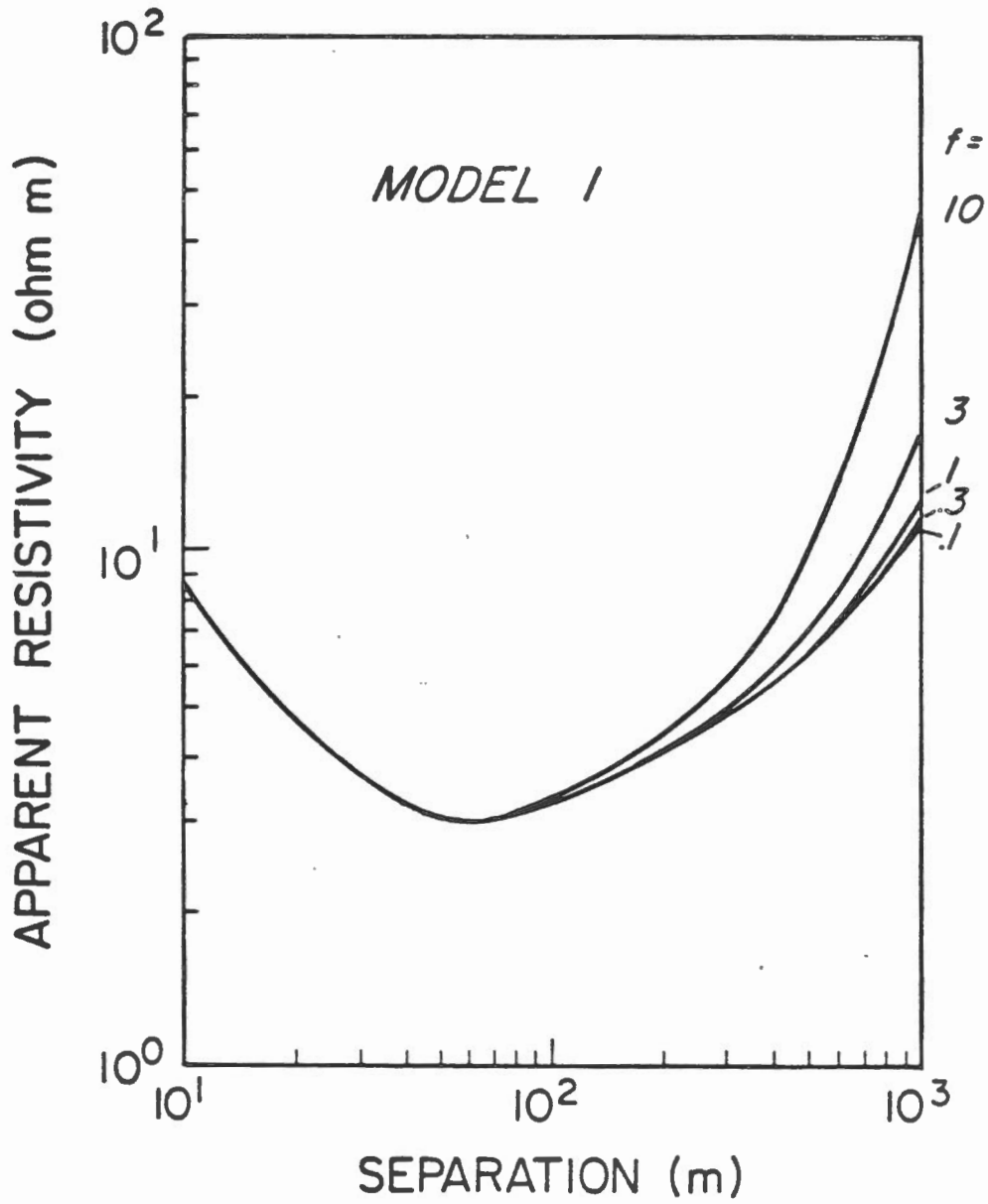


Figure 4.2.1b: Model 1 - apparent resistivity as a function of separation for the range of frequencies 0.1 to 10 Hz.

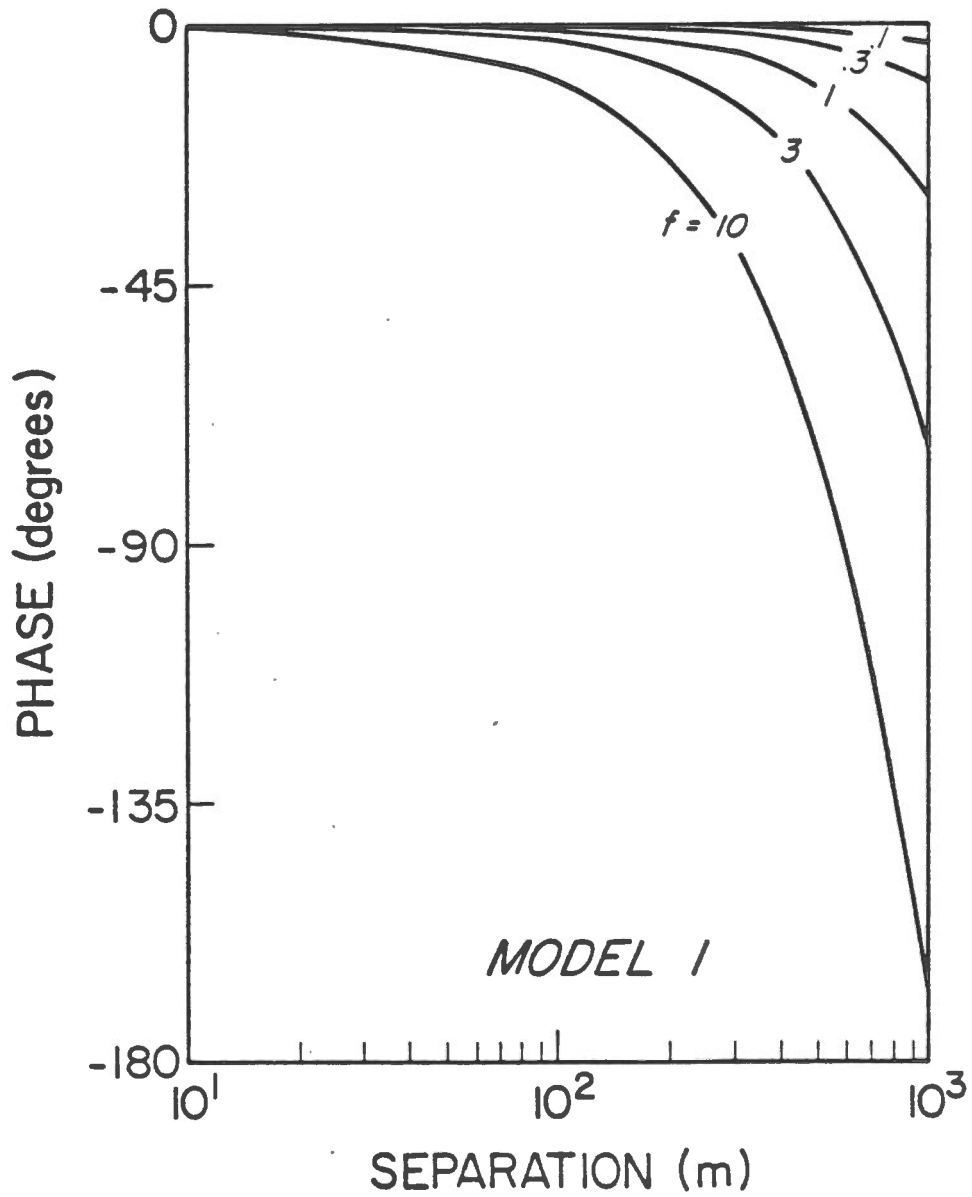


Figure 4.2.1c: Model 1 - magnetic field phase as a function of separation for the range of frequencies 0.1 to 10 Hz.

the grade of permafrost by the magnitude of the anisotropy? Is it certainly safe to conclude that hard permafrost exhibits only a small anisotropy. Whether the larger values of anisotropy at shallow depths can always be correlated with soft permafrost is a matter for further study.

4.2: Forward one-dimensional modelling

The theory presented in section 3.1 has been implemented as a computer algorithm so that the MOSES response of a layered earth may be calculated. The response of a given model is presented as a group of three curves - magnetic field amplitude, apparent resistivity and magnetic field phase. Edwards et al. (1984) derived an apparent resistivity formula as an elementary aid in the interpretation of MOSES data. Traditionally, such a formula is a function of the actual field measurements multiplied by a numerical factor derived for the special case when the ground volume studied is homogeneous and isotropic. For MOSES, no simple formula exists which is valid over a wide range of model parameters. However, an asymptotic expansion of the theoretical response of a uniform zone beneath the sea does give a formula which may be used to transform field data into a domain where they may be compared with model type curves for the whole range of model parameters we encounter. The formula for the apparent resistivity ρ_a is

$$\rho_a = \rho_0 \mu I d / 4 \pi r^2 B, \quad (4.2.1)$$

where ρ_0 , μ , I , d , r and B are the resistivity of sea water, the permeability of free space, the bipole current, the depth of the sea, the transmitter-receiver separation and the magnitude of the azimuthal magnetic component respectively. The expression reduces to the resistivity of a half-space beneath the sea only when the contrast in resistivity between the sea water and the sea floor is large, when the separation r is greater than the depth d and when the frequency tends to zero. A further constraint is that the integrated conductance of the sea layer has to be large compared with the product of the half-space conductivity and the separation.

The first set of curves presented, Model 1, is the very simple case of the uniform half-space response. The sea layer thickness is selected as 50 m, typical of the Beaufort Sea, and the resistivities of the sea and the material beneath are .3 and 3 Ωm respectively. The latter resistivity is typical of an unfrozen sedimentary zone.

The magnetic field amplitude curves shown in Figure 4.2.1a for the range of

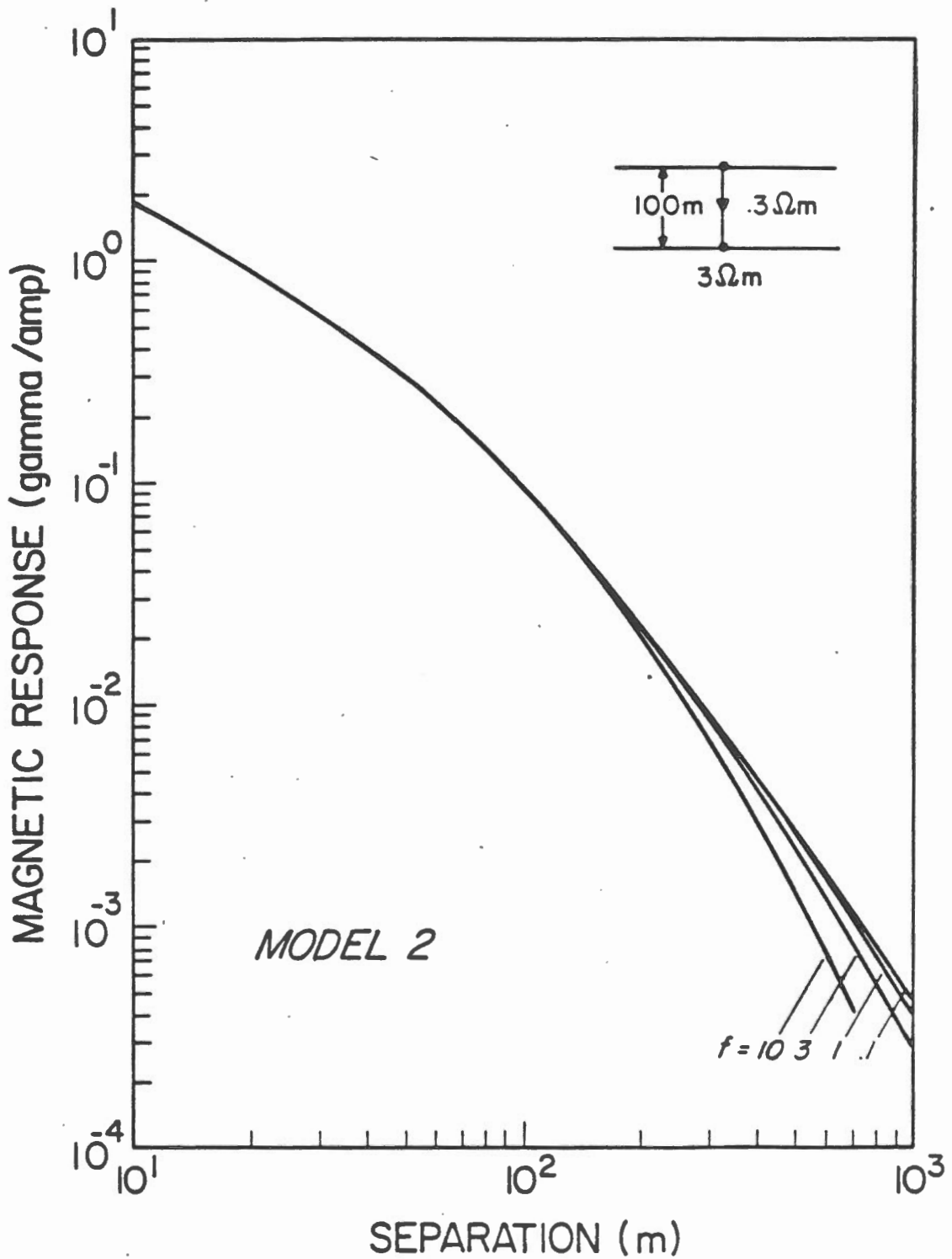


Figure 4.2.2a: Model 2 - magnetic field amplitude as a function of separation for the range of frequencies 0.1 to 10 Hz.

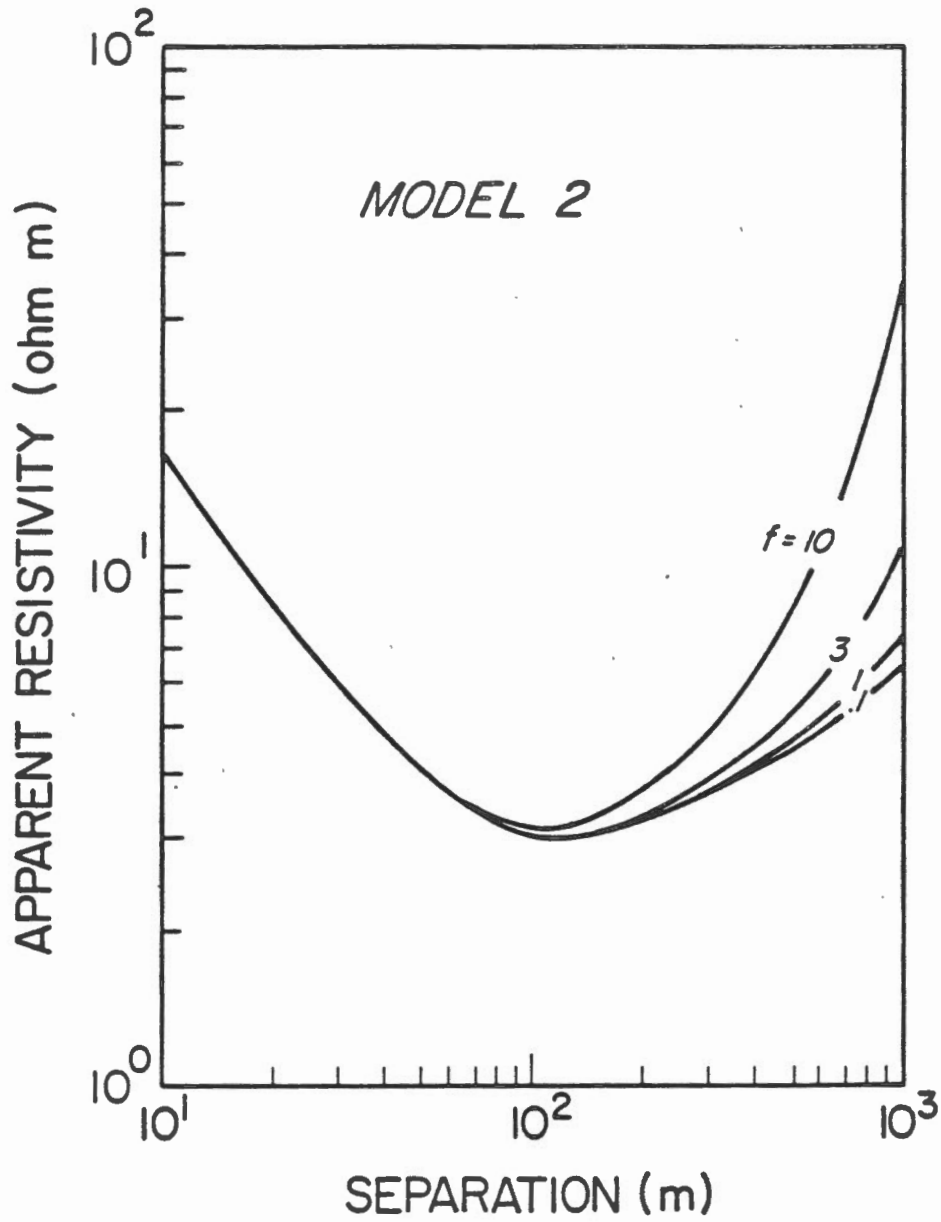


Figure 4.2.2b: Model 2 - apparent resistivity as a function of separation for the range of frequencies 0.1 to 10 Hz.

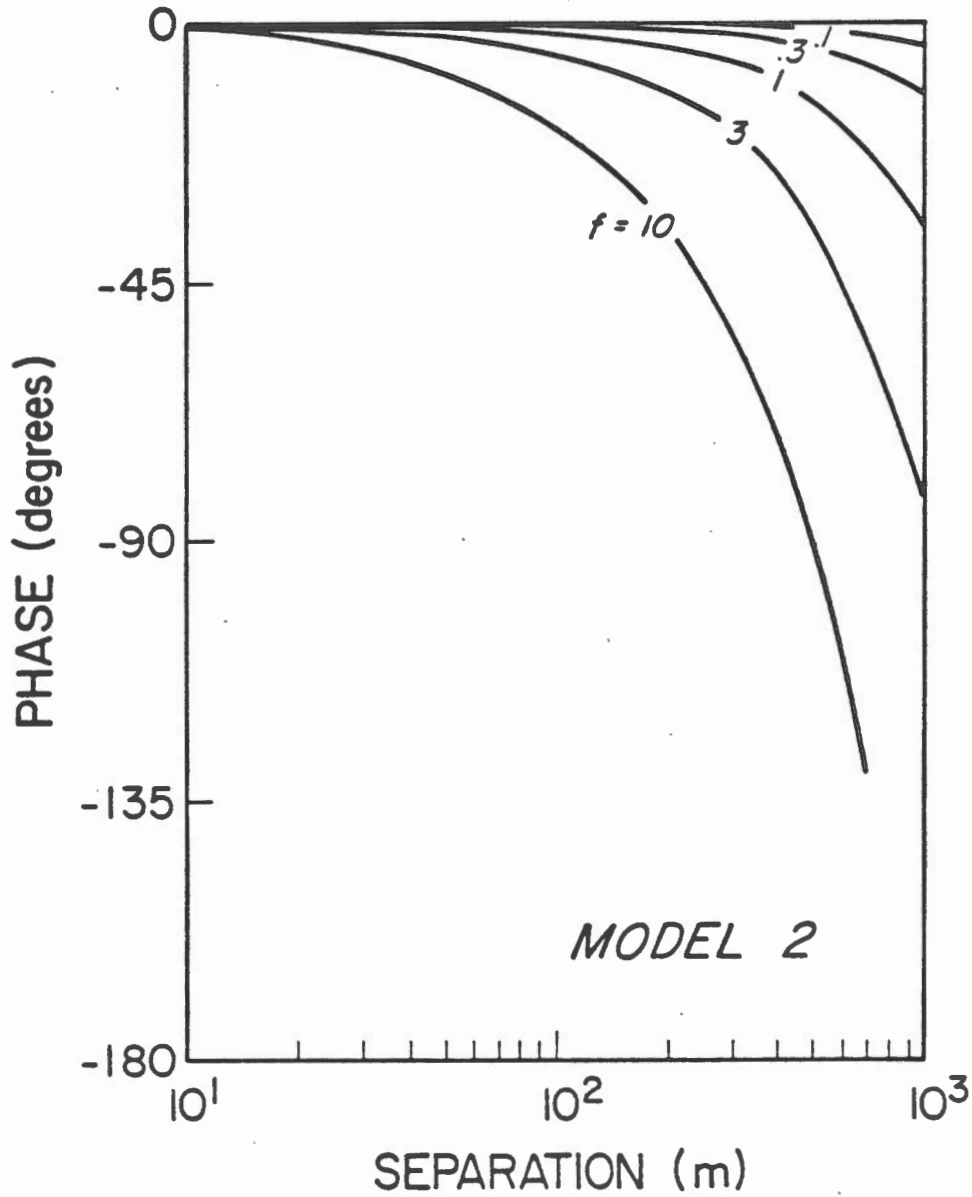


Figure 4.2.2c: Model 2 - magnetic field phase as a function of separation for the range of frequencies 0.1 to 10 Hz.

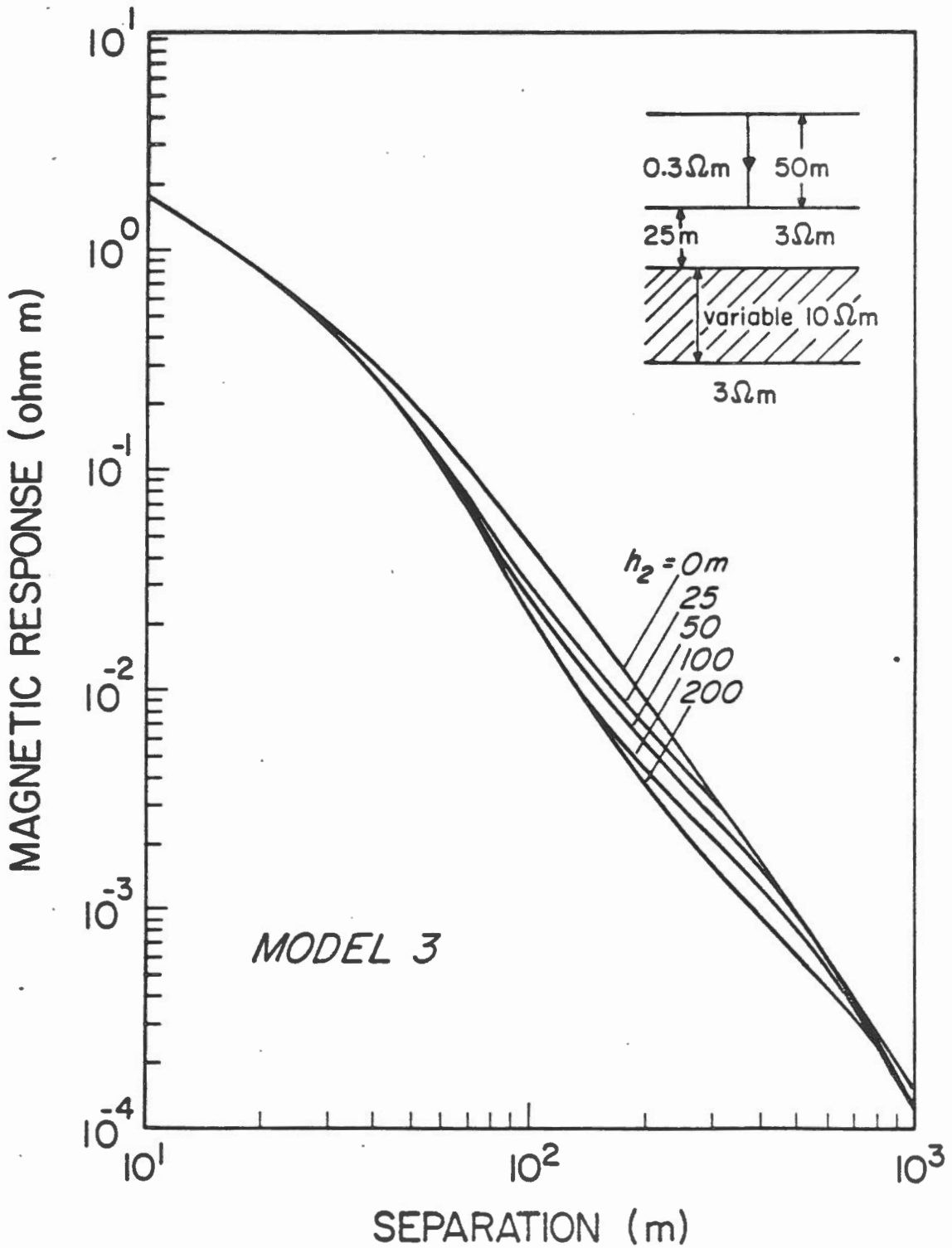


Figure 4.2.3a: Model 3 - magnetic field amplitude as a function of separation for the range of intermediate layer thicknesses 0 to 200 metres.

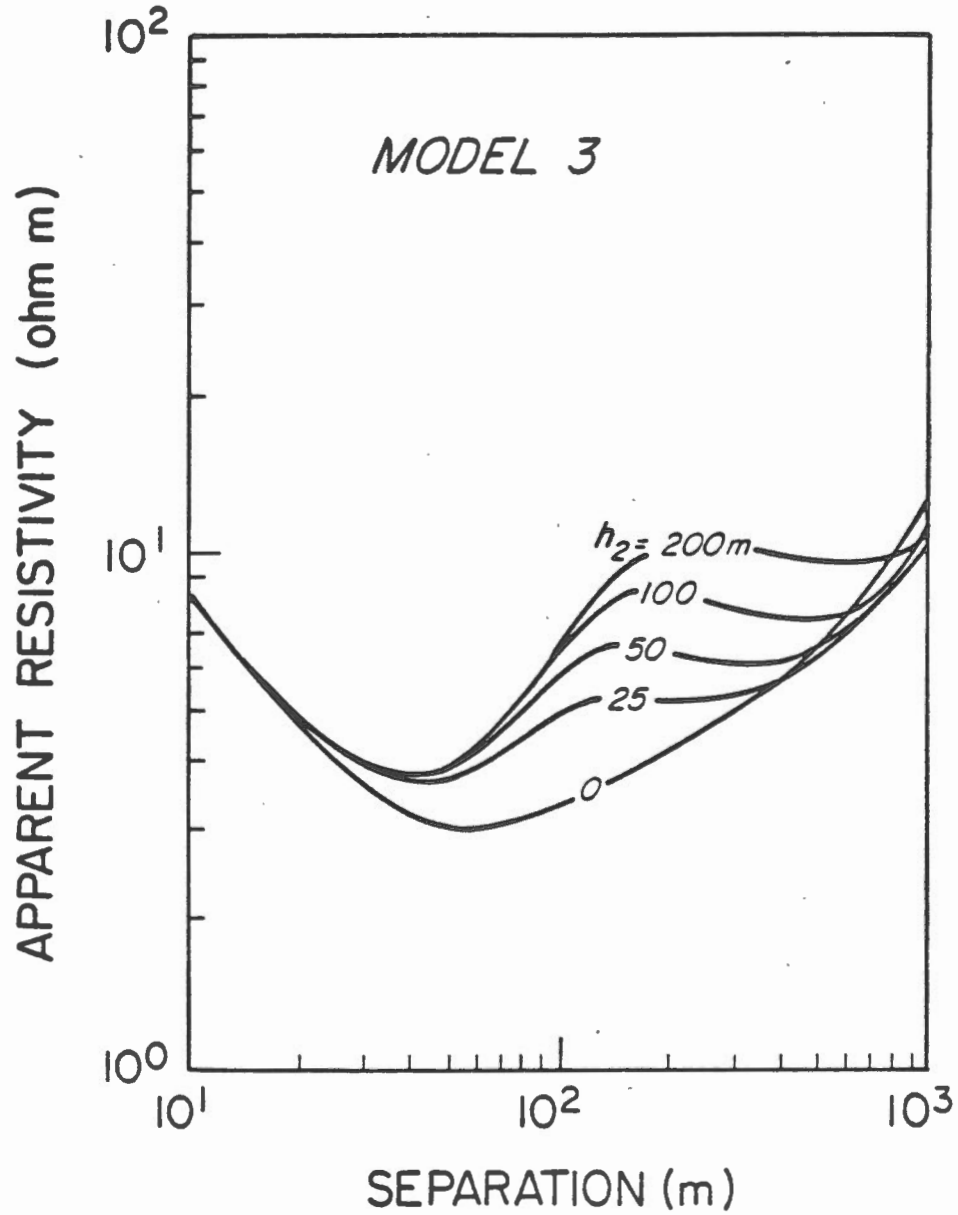


Figure 4.2.3b: Model 3 - apparent resistivity as a function of separation for the range of intermediate layer thicknesses 0 to 200 metres.

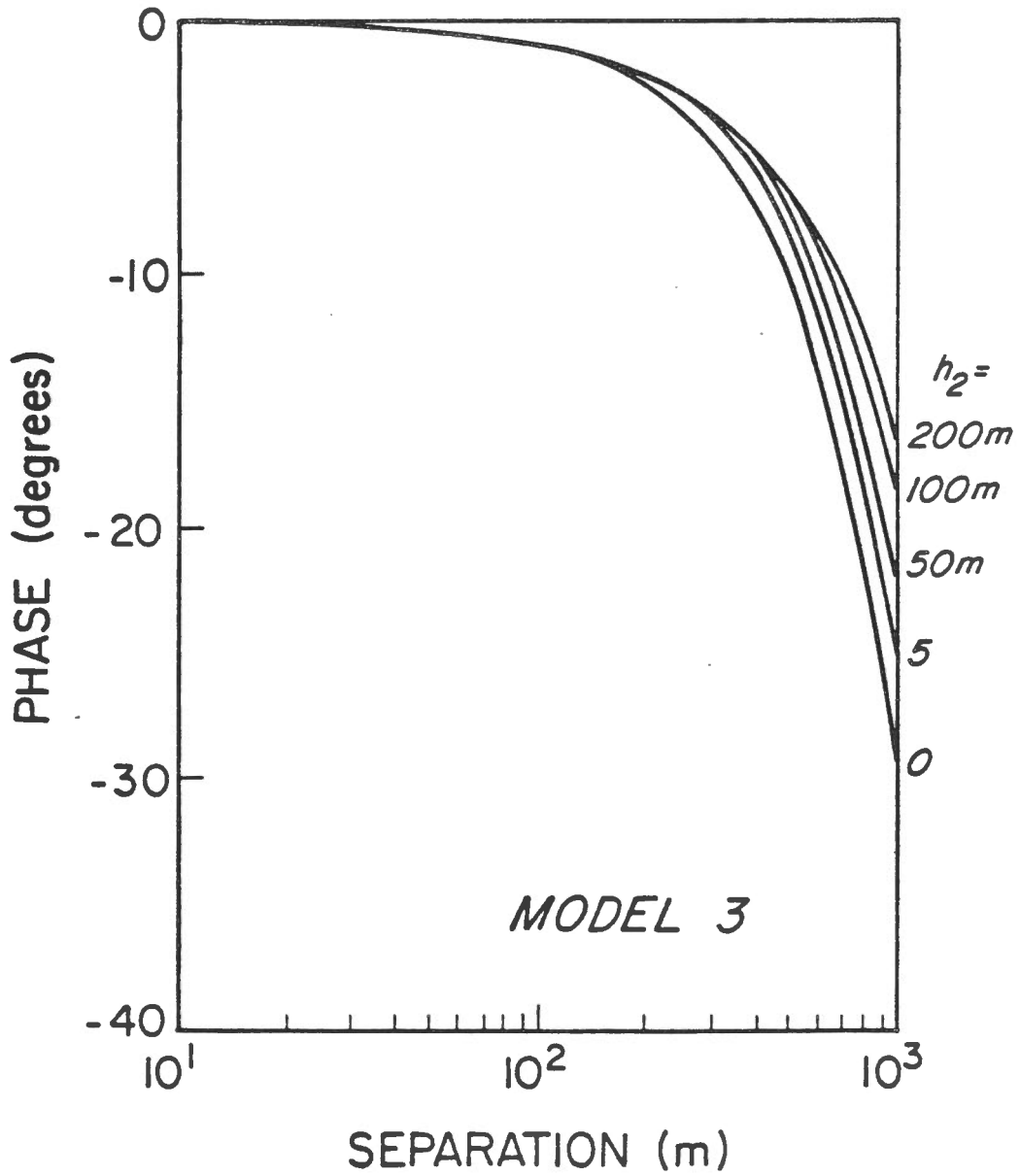


Figure 4.2.3c: Model 3 - magnetic field phase as a function of separation for the range of intermediate layer thicknesses 0 to 200 metres.

frequencies $0.1 < f < 10$. Hz are characteristic MOSES half-space responses. For separations r less than and greater than depth d , the power law behaviour is r^{-1} and r^{-2} respectively. At separations of about 1 km the inverse power law exponent increases due to both induction effects and the violation of the last condition given above for the validity of the apparent resistivity formula. The conductance, i.e. the depth, of the sea water is too small to carry the bipole current out to large separations. Of particular interest to the designer of an Arctic experiment is the amplitude of the field at large distances which is of the order of 1 milligamma per ampere of bipole current.

The apparent resistivity curves of Figure 4.2.1b merely express the deviation of the magnetic field from a r^{-2} behaviour more clearly. The phase curves define the useful range of frequencies for the designer, and indicate that .1 Hz is the static limit whereas 10 Hz produces very significant phase rotations at the larger separations.

The second model, Model 2, differs from model 1 in that the depth of the sea has been increased from 50 to 100 m. The calculated magnetic field amplitudes, Figure 4.2.2a, are twice those of Figure 4.2.1a for intermediate values of r and a factor of 3 or 4 greater at the largest values of r shown. Clearly, an Arctic experiment should be conducted in deep water if possible.

The final model, Model 3, is included to demonstrate the detection of a $10 \Omega m$ resistive zone within a $3 \Omega m$ background. The latter could be near-surface, soft permafrost. The frequency was selected as 1 Hz. Notice the clear effect on the type curves, Figures 4.2.3a and 4.2.3b, of the intermediate layer. Notice that the type curve for a layer 200 m thick returns to the normal type curve by a separation of 1 Km, implying that a sounding to this separation could resolve both the upper and lower interfaces. While sets of curves like these can suggest to the designer of an experiment that a parameter like layer thickness is resolved, they do not prove that fact. The problem is the non-uniqueness of electromagnetic data, and the whole question of resolution must be addressed more formally.

4.3: *Eigenparameter statistical analysis*

The investigation of the resolution by a given data set of a model parameter has to address a fundamental question of uniqueness. When one parameter of a model is changed, a change will be observed in the model type curve which passes through the data. If a certain parameter change moves the type curve, on average,

just outside the errors on the data, it is tempting to state that the parameter is resolved to an accuracy which depends simply on size of this change. Unfortunately, the way in which the type curve is displaced need not be unique, and varying the value of a different model parameter, or the values of a particular group of model parameters, sometimes produces a very similar displacement. In such a case, one can not argue that the first model parameter is resolved by the data even though varying it does significantly alter the form of the type curve. The problem of this type of parameter intercorrelation is avoided by a technique known as eigenparameter statistical analysis. The method provides a very clear, unambiguous set of statements for the interpreter, or the designer, of an experiment as to what parts of his model are determined by real or synthetic data respectively. Further, if experimental or estimated errors are assigned to the data, the method provides a simple scheme for assessing the errors in the model.

Let a given model have parameters $P_j, j = 1, N$. The P_j are the thicknesses, resistivities and coefficients of anisotropy of the layered model. Let the data set, either an experimental or a synthetic one, from which the model is determined be $Y_i, i = 1, M$, and let the measured or assigned errors on the data be $e_i, i = 1, M$.

For a small variation dP_j in a parameter P_j , the expected changes dY_i in the data set Y_i are given by the first term of Taylor's series as

$$dY_i = \sum_{j=1}^N A_{ij} dP_j, \quad (4.3.1)$$

or, in matrix notation,

$$d\mathbf{Y} = \mathbf{A} d\mathbf{P}, \quad (4.3.2)$$

where each coefficient A_{ij} is simply a measure of the sensitivity of datum Y_i to a change in parameter P_j , or the partial derivative $\partial Y_i / \partial P_j$. These derivatives may be found either analytically or numerically from the forward solution given the physics of the problem.

Expressions (4.3.1) and (4.3.2) clearly display the problem of non-uniqueness. A given change in a datum can be produced by changing any one of the model parameters provided the associated A_{ij} is non vanishing. However, it is possible to choose linear combinations $d\mathbf{P}^*$ of the parameter changes $d\mathbf{P}$ and corresponding

linear combinations dY^* of the data changes dY such that expressions (4.3.1) and (4.3.2) are greatly simplified. The process of finding these combinations is through Singular Value Decomposition (SVD) of the matrix A . Standard software exists to write A as

$$A = U \times L \times V^T. \quad (4.3.3)$$

The matrices U and V have the property that

$$U^T U = V^T V = V V^T = 1, \quad (4.3.4)$$

and the matrix L is diagonal. If dY^* and dP^* are defined by the equations

$$dY^* = U^T dY, \quad (4.3.5)$$

and

$$dP^* = V^T dP, \quad (4.3.6)$$

then equation (4.3.2) may be written as

$$dY^* = L dP^*. \quad (4.3.7)$$

Only one set of weights U and V permits this simplification. The matrix L contains the eigenvalues of A . The vectors dP^* and dY^* are termed eigenparameters and eigendata respectively. Each eigendatum is related to a corresponding eigenparameter *and only that eigenparameter* through the equation

$$dY_j^* = L_{jj} dP_j^*, \quad 1 < j < N. \quad (4.3.8)$$

The problem of parameter intercorrelation is clearly avoided if parameter resolution and error assessment are considered in terms of these eigensolutions.

The error in each eigenparameter is expressed very simply in terms of the above analysis provided each datum of the data set has an independent standard error estimate ϵ of unity. Expression (4.3.5) is a relationship between small changes in the original data and small changes in the eigendata. The same set of weights must relate the errors in the two data types, so that

$$e_i^* = \sum_{j=1}^M U_{ji} e_j. \quad (4.3.9)$$

The covariance, or mean product, of the errors e_i^* and e_l^* is

$$\text{cov}(e_i^*, e_l^*) = \mathcal{E}(e_i^*, e_l^*) = \sum_{j=1}^M \sum_{k=1}^M U_{ji} U_{lk} \mathcal{E}(e_j, e_k), \quad (4.3.10)$$

where \mathcal{E} is the expectation value operator. The original data errors are independent and of unit variance. Hence, their covariance is simply given by

$$\mathcal{E}(e_j, e_k) = \delta_{jk}. \quad (4.3.11)$$

Equation (4.3.10) reduces first to

$$\text{cov}(e_i^*, e_l^*) = \sum_{j=1}^M U_{ji} U_{lj}, \quad (4.3.12)$$

and then to

$$\text{cov}(e_i^*, e_l^*) = \delta_{il}, \quad (4.3.13)$$

because the rows of the matrix \mathbf{U}^T are orthonormal vectors. Equation (4.3.13) shows that the standard errors in the eigendata are also independent and also have a value of unity. Now any small change in an eigendatum is related to a corresponding small change in an eigenparameter by equation (4.3.8). Hence, the standard error in an eigenparameter is just the reciprocal of the corresponding eigenvalue - a remarkably simple result.

Each element $\partial Y_i / \partial P_j$ of the Jacobian matrix \mathbf{A} is scaled in two ways before SVD is undertaken. It is divided by e_i . This has the effect of rescaling the units in which datum Y_i is measured so that its standard error is unity, as required by the theory. The element is also multiplied by P_j . This has the effect of redefining the parameter P_j as $\log P_j$, because

$$P_j \partial Y_i / \partial P_j = \partial Y_i / \partial (\log P_j). \quad (4.3.14)$$

The whole procedure of eigenparameter analysis clearly has very limited appeal if the eigenparameters cannot be identified as representing physically understandable combinations of the original model parameters. The use of logarithmic scaling of the model parameters makes this identification much like dimensional analysis. As an example, consider the model of a layer of resistivity ρ_1 and thickness h_1 over a half-space of resistivity ρ_2 . A change in P_1^* , one of the three possible eigenparameters, is related to changes in the model parameters by

$$dP_1^* = V_{11}d(\log \rho_1) + V_{21}d(\log h_1) + V_{31}d(\log \rho_2). \quad (4.3.15)$$

The weights V_{11} , V_{21} and V_{31} are normalised by the SVD analysis so that the sum of their squares is unity. The physical interpretation of the eigenparameter may be deduced as

$$\rho_1^{V_{11}} h_1^{V_{21}} \rho_2^{V_{31}}. \quad (4.3.16)$$

If the conductivity-thickness product of the layer is the 'physical interpretation' of the eigenparameter, then $V_{11} = -V_{21} = .707$ and $V_{31} = 0$. Also, the standard error in the eigenparameter is the standard error in the logarithm of the conductivity-thickness product or, equivalently, the fractional standard error in the conductivity-thickness product itself.

The relationship between the fractional standard error in a given model parameter and the standard errors in the eigenparameters is obtained by inverting equation (4.3.6), having noted from equation (4.3.4) that the inverse of matrix \mathbf{V}^T is just matrix \mathbf{V} . A coarse upper bound on the fractional standard error in the thickness h_1 in the example is given by

$$(V_{11}/L_{11}) + (V_{12}/L_{22}) + (V_{13}/L_{33}). \quad (4.3.17)$$

where L_{11} , L_{22} and L_{33} are the eigenvalues of the Jacobian. A fractional error in a model parameter may only be computed in this manner provided it is small compared with unity because the theory described is only valid for small changes, that is to first order. If the standard error in the parameter is predicted as being much larger than unity, due for example to a non-zero weight being divided by a small eigenvalue, then a different technique has to be adopted to find the true error bound.

4.4: Model resolution, hypothesis testing

In this section, the capability of the MOSES method of resolving the parameters of a given model is investigated. For each investigation, the starting point is a layered model of the ground. A set of synthetic MOSES responses is next computed for a reasonable survey over the area. The responses are assigned reasonable errors, based on experience. The result is a set of synthetic data.

An inverse analysis, using parameter eigenvector statistics is performed. The analysis will show how well the model parameters are constrained by the data. Some combinations of parameters will be well determined, some poorly. In other words, the model in total is rarely completely defined by the data set. It is particularly important in real data inversion to convey to the interpreter the nature of the undetermined parameter combinations. The model can be altered in these directions without influencing the data. Consequently, if the interpreter has a hypothesis that the real earth is somewhat different from the inverted model, then he can try to alter the inverted model towards the hypothetical model by changing the undetermined parameters. In many, many cases electrical data and geological data can be made consistent by this simple exercise.

Another game that can be played is to fix certain parameters in the model, based on a priori knowledge, and then examine whether the remainder are determined.

The eigenparameter statistics are displayed in tables. The eigenparameters are ranked from top to bottom in order of decreasing eigenvalue, increasing standard error. Each coefficient in a row is the weight with which the logarithm of each model parameter is included in the combination of parameters forming the eigenparameter. The interpretation of the eigenparameter is included under 'physics', while the standard error is the last entry in the row.

The first model is the elementary half-space, Model 1 of section 4.2. The anisotropy of the half-space is assumed to be unity. The set of synthetic apparent resistivity data at the low-frequency static limit is displayed in Figure 4.4.1a. There are 7 data points with a constant, conservative percentage error of 10 per cent. We will allow the model to have two free parameters, mean resistivity ρ_1^m and anisotropy f_1 . The eigenanalysis is shown in Table 4.4.1a. The eigenparameters are just the two free parameters, a very special case. The resistivity has a standard error of 5 per cent. The anisotropy has a standard error right outside the linear range,

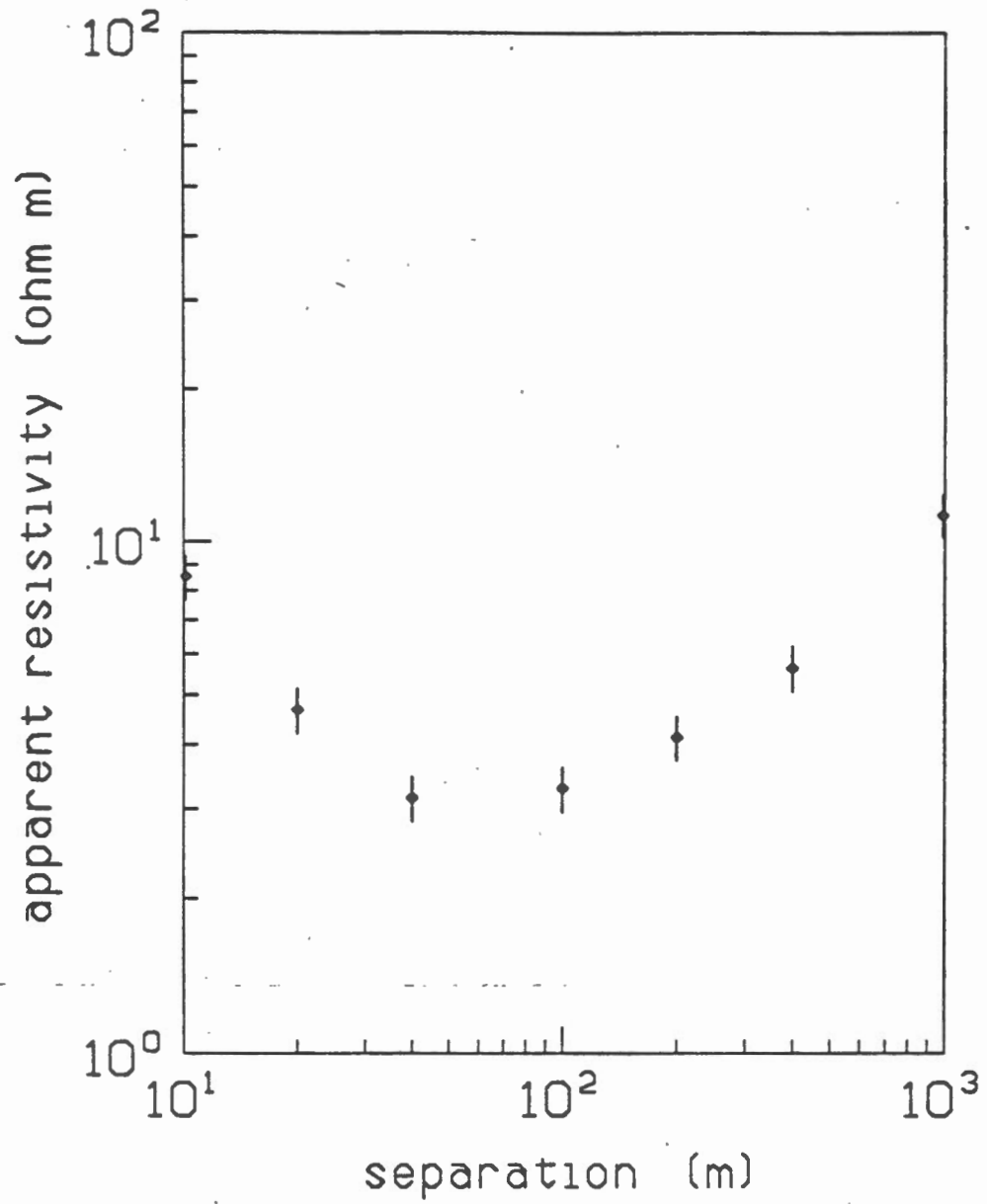


Figure 4.4.1a: Model 1 - a synthetic apparent resistivity data set, frequency zero, anisotropy unity.

| P* | LAYER 1 | | | LAYER 2 | | | LAYER 3 | | PHYSICS | STD. ERR. |
|----|-----------------------------------|--------------------------|--------------------------|-----------------------------------|--------------------------|--------------------------|-----------------------------------|--------------------------|----------------|-----------|
| | $\frac{\Delta\rho_1^m}{\rho_1^m}$ | $\frac{\Delta f_1}{f_1}$ | $\frac{\Delta h_1}{h_1}$ | $\frac{\Delta\rho_2^m}{\rho_2^m}$ | $\frac{\Delta f_2}{f_2}$ | $\frac{\Delta h_2}{h_2}$ | $\frac{\Delta\rho_3^m}{\rho_3^m}$ | $\frac{\Delta f_3}{f_3}$ | | |
| 1 | 1.00 | 0.00 | | | | | | | Resistivity L1 | 0.05 |
| 2 | 0.00 | 1.00 | | | | | | | Anisotropy L1 | 31.00 |
| 3 | | | | | | | | | | |
| 4 | | | | | | | | | | |
| 5 | | | | | | | | | | |
| 6 | | | | | | | | | | |
| 7 | | | | | | | | | | |
| 8 | | | | | | | | | | |

Table 4.4.1a Model 1 - the parameter eigenvector analysis at the low-frequency, static limit based on apparent resistivity data.

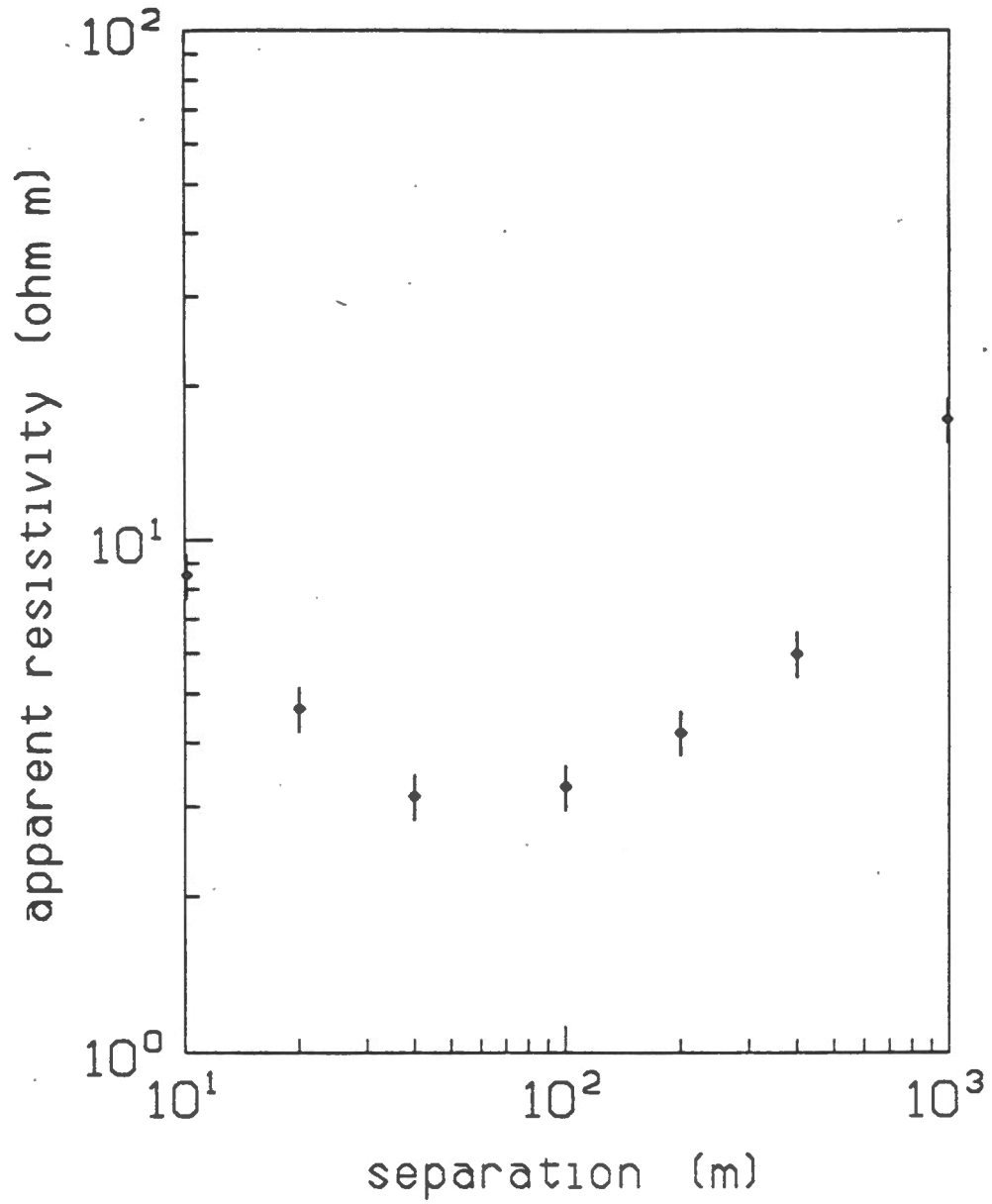


Figure 4.4.lb: Model 1 - a synthetic apparent resistivity data set, frequency 3 Hz, anisotropy unity.

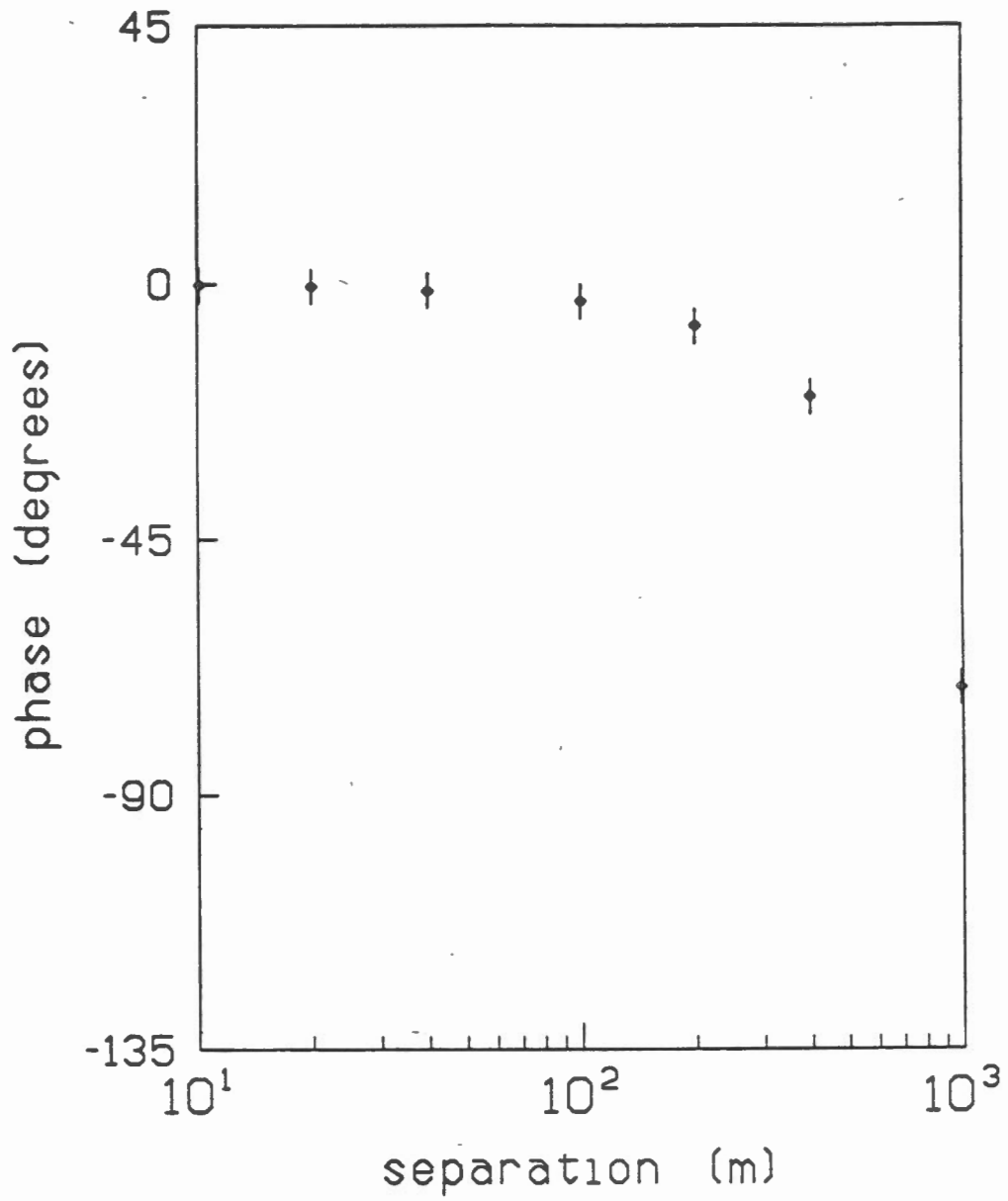


Figure 4.4.1c: Model 1 - a synthetic phase data set, frequency 3 Hz, anisotropy unity.

| P* | LAYER 1 | | | LAYER 2 | | | LAYER 3 | | PHYSICS | STD. ERR. |
|----|-----------------------------------|--------------------------|--------------------------|-----------------------------------|--------------------------|--------------------------|-----------------------------------|--------------------------|----------------|-----------|
| | $\frac{\Delta\rho_1^m}{\rho_1^m}$ | $\frac{\Delta f_1}{f_1}$ | $\frac{\Delta h_1}{h_1}$ | $\frac{\Delta\rho_2^m}{\rho_2^m}$ | $\frac{\Delta f_2}{f_2}$ | $\frac{\Delta h_2}{h_2}$ | $\frac{\Delta\rho_3^m}{\rho_3^m}$ | $\frac{\Delta f_3}{f_3}$ | | |
| 1 | 0.99 | 0.02 | | | | | | | Resistivity L1 | 0.05 |
| 2 | -0.02 | 0.99 | | | | | | | Anisotropy L1 | 0.22 |
| 3 | | | | | | | | | | |
| 4 | | | | | | | | | | |
| 5 | | | | | | | | | | |
| 6 | | | | | | | | | | |
| 7 | | | | | | | | | | |
| 8 | | | | | | | | | | |

Table 4.4.lb: Model 1 - the parameter eigenvector analysis at a frequency of 3 Hz based on apparent resistivity data.

| P* | LAYER 1 | | | LAYER 2 | | | LAYER 3 | | PHYSICS | STD. ERR. |
|----|-----------------------------------|--------------------------|--------------------------|-----------------------------------|--------------------------|--------------------------|-----------------------------------|--------------------------|---------|-----------|
| | $\frac{\Delta\rho_1^m}{\rho_1^m}$ | $\frac{\Delta f_1}{f_1}$ | $\frac{\Delta h_1}{h_1}$ | $\frac{\Delta\rho_2^m}{\rho_2^m}$ | $\frac{\Delta f_2}{f_2}$ | $\frac{\Delta h_2}{h_2}$ | $\frac{\Delta\rho_3^m}{\rho_3^m}$ | $\frac{\Delta f_3}{f_3}$ | | |
| 1 | 0.87 | 0.49 | | | | | | |) Mixed | 0.04 |
| 2 | -0.49 | 0.87 | | | | | | | | 0.08 |
| 3 | | | | | | | | | | |
| 4 | | | | | | | | | | |
| 5 | | | | | | | | | | |
| 6 | | | | | | | | | | |
| 7 | | | | | | | | | | |
| 8 | | | | | | | | | | |

Table 4.4.lc: Model 1 - the parameter eigenvector analysis at a frequency of 3 Hz based on both apparent resistivity and phase data.

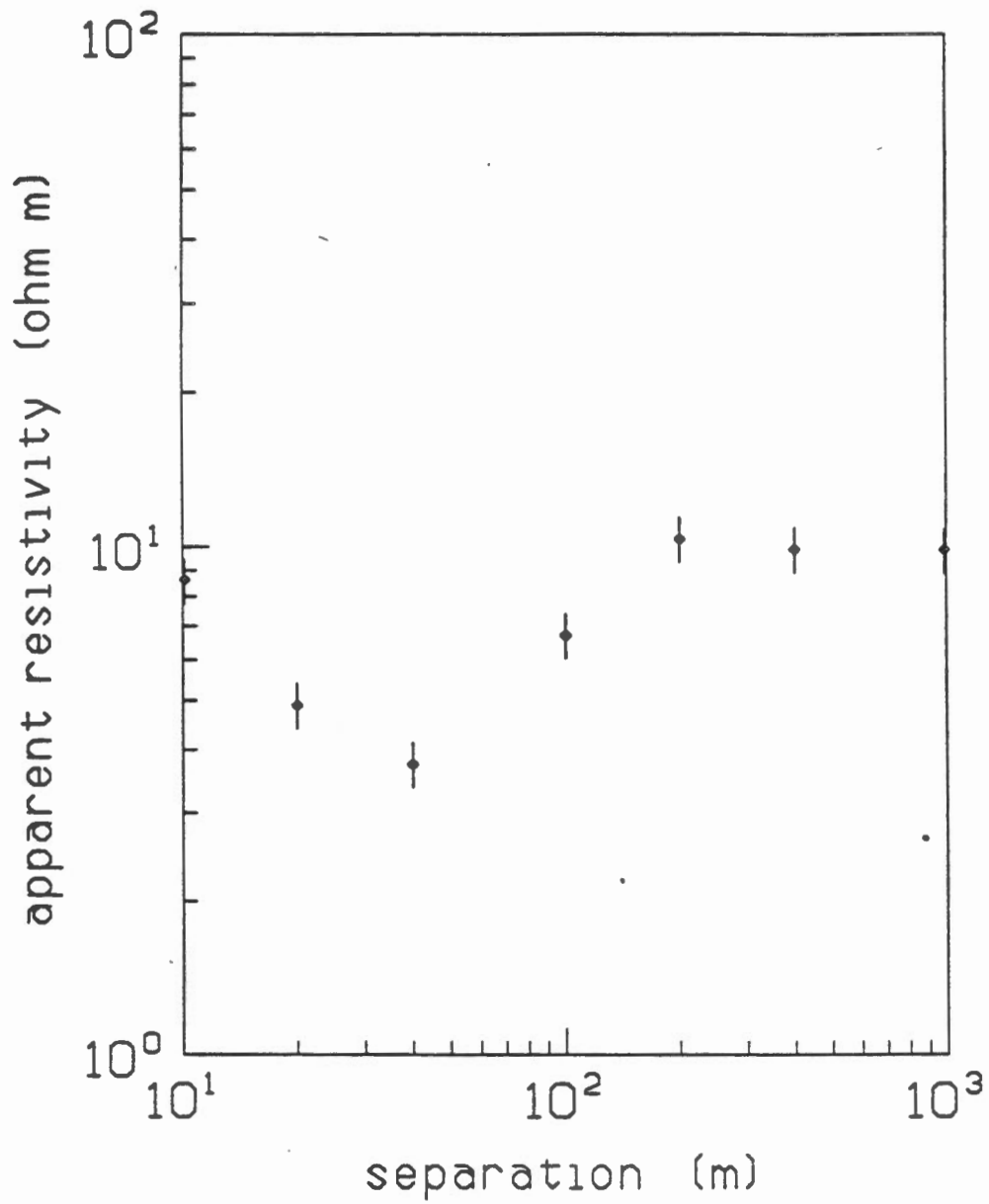


Figure 4.4.2a: Model 3 - a synthetic apparent resistivity data set, frequency zero, anisotropy unity everywhere, intermediate layer thickness 100 m.

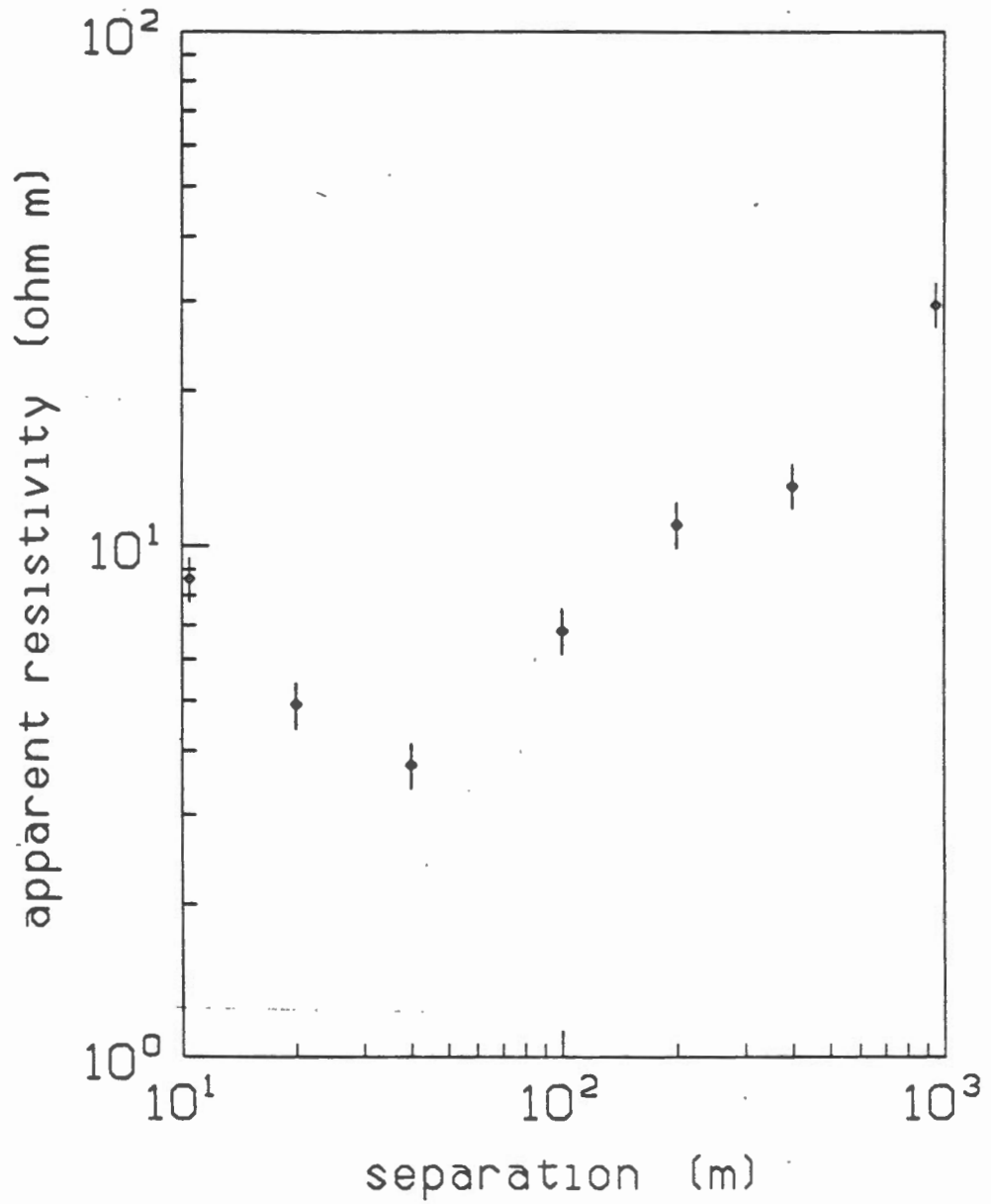


Figure 4.4.2b: Model 3 - a synthetic apparent resistivity data set, frequency 15 Hz, anisotropy unity everywhere, intermediate layer thickness 100 m.

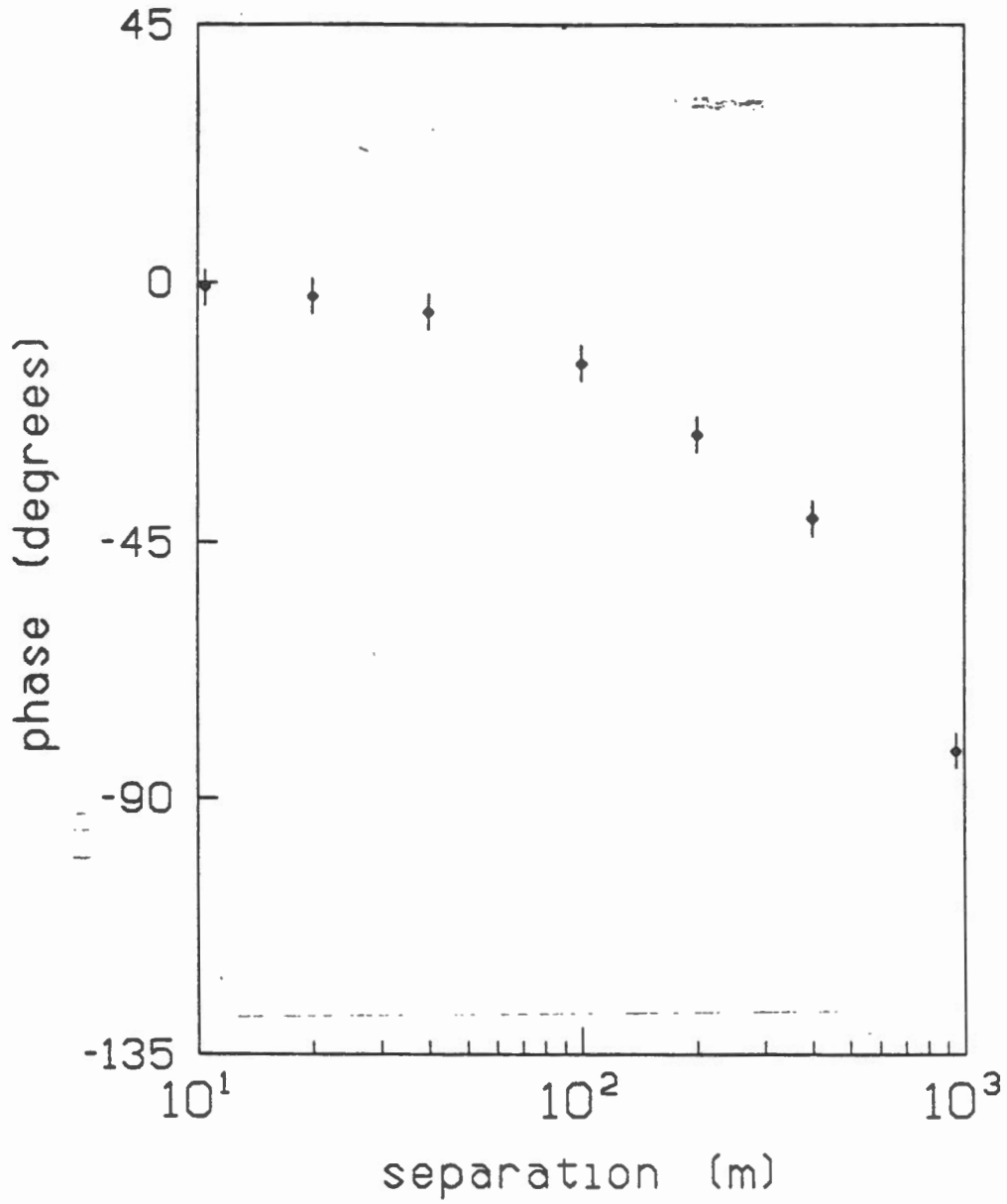


Figure 4.4.2c: Model 3 - a synthetic phase data set, frequency 15 Hz, anisotropy unity everywhere, intermediate layer thickness 100 m.

| P* | LAYER 1 | | | LAYER 2 | | | LAYER 3 | | PHYSICS | STD. ERR. |
|----|-----------------------------------|--------------------------|--------------------------|-----------------------------------|--------------------------|--------------------------|-----------------------------------|--------------------------|-------------------------------------|-----------|
| | $\frac{\Delta\rho_1^m}{\rho_1^m}$ | $\frac{\Delta f_1}{f_1}$ | $\frac{\Delta h_1}{h_1}$ | $\frac{\Delta\rho_2^m}{\rho_2^m}$ | $\frac{\Delta f_2}{f_2}$ | $\frac{\Delta h_2}{h_2}$ | $\frac{\Delta\rho_3^m}{\rho_3^m}$ | $\frac{\Delta f_3}{f_3}$ | | |
| 1 | | | 0.25 | -0.92 | | -0.27 | | | Resistivity L2)) Mixed) | 0.07 |
| 2 | | | -0.87 | -0.10 | | -0.48 | | | | 0.16 |
| 3 | | | 0.41 | 0.36 | | -0.83 | | | | 0.44 |
| 4 | | | | | | | | | | |
| 5 | | | | | | | | | | |
| 6 | | | | | | | | | | |
| 7 | | | | | | | | | | |
| 8 | | | | | | | | | | |

Table 4.4.2a: Model 3 - the parameter eigenvector analyses at the low-frequency, static limit based on apparent resistivity data.

| P* | LAYER 1 | | | LAYER 2 | | | LAYER 3 | | PHYSICS | STD. ERR. |
|----|-----------------------------------|--------------------------|--------------------------|-----------------------------------|--------------------------|--------------------------|-----------------------------------|--------------------------|---------------------------------|-----------|
| | $\frac{\Delta\rho_1^m}{\rho_1^m}$ | $\frac{\Delta f_1}{f_1}$ | $\frac{\Delta h_1}{h_1}$ | $\frac{\Delta\rho_2^m}{\rho_2^m}$ | $\frac{\Delta f_2}{f_2}$ | $\frac{\Delta h_2}{h_2}$ | $\frac{\Delta\rho_3^m}{\rho_3^m}$ | $\frac{\Delta f_3}{f_3}$ | | |
| 1 | | | 0.18 | -0.64 | -0.74 | -0.01 | | | Vertical Res.L2) Mixed) | 0.02 |
| 2 | | | -0.60 | -0.58 | 0.36 | -0.41 | | | | 0.07 |
| 3 | | | 0.73 | -0.42 | 0.54 | -0.01 | | | | 0.12 |
| 4 | | | -0.26 | -0.27 | 0.16 | 0.91 | | | Thickness L2 | 0.28 |
| 5 | | | | | | | | | | |
| 6 | | | | | | | | | | |
| 7 | | | | | | | | | | |
| 8 | | | | | | | | | | |

Table 4.4.2b: Model 3 - the parameter eigenvector analyses at a frequency of 15 Hz based on apparent-resistivity and phase data.

3100 per cent. The result is exactly the expected one. At the dc, static limit electrical methods cannot resolve anisotropy. The interpreter has complete freedom to vary the undetermined anisotropy to conform with geological information.

A second set of data, apparent resistivity and phase at 3 Hz, is shown in Figures 4.4.1b and 4.4.1c. The phase data have standard errors of 3 degrees. The eigenanalysis of the apparent resistivity, essentially amplitude, data alone yields the results in Table 4.4.1b. The eigenparameters are virtually the same as those in Table 4.1.1a, but the error in the anisotropy has been reduced to 22 per cent. The eigenanalysis of the total data set is shown in Table 4.4.1c. The eigenparameters are now mixed, but still mostly resistivity and anisotropy, and the largest error has been reduced to 8 per cent. The use of phase data to measure anisotropy was suggested by Edwards et al. (1985). The results here confirm their analysis.

The second model is described in section 4.2 as Model 3. The thickness of the second layer is fixed at 100 m. All anisotropies are assumed to be unity. A dc, static, apparent resistivity synthetic data set is shown in Figure 4.4.2a. In analysing these data, we shall assume that we have been told by a client that we are looking for a layer of permafrost within a uniform half-space of known resistivity. The object of the survey will be to find the depth to the top and thickness of the permafrost and to obtain its physical properties. The eigenanalysis is shown in Table 4.4.2a. The best determined eigenparameter is the resistivity of the layer, standard error 7 per cent. All three unknowns are determined to at worst 44 per cent. Clearly, the message here is that 10 per cent errors are not good enough!

A data set of both apparent resistivity and phase is shown in Figures 4.4.2b and 4.4.2c. The addition of the phase data enables us to release the anisotropy of the intermediate zone as a free parameter. The eigenanalysis is shown in Table 4.4.2b. All parameters are determined to better than 28 per cent. The designer of an experiment should recommend data collection to an accuracy of about 2 degrees in phase and 2 per cent in amplitude to resolve the layer and hopefully satisfy the client.

The computer software written for these analyses is quite general and can be adapted for any geophysical method.

4.5 Three dimensional modelling

Several computer programmes were written implementing the theory of the MOSES response of thin lamellae described in sections 3.4 and 3.5. The first model

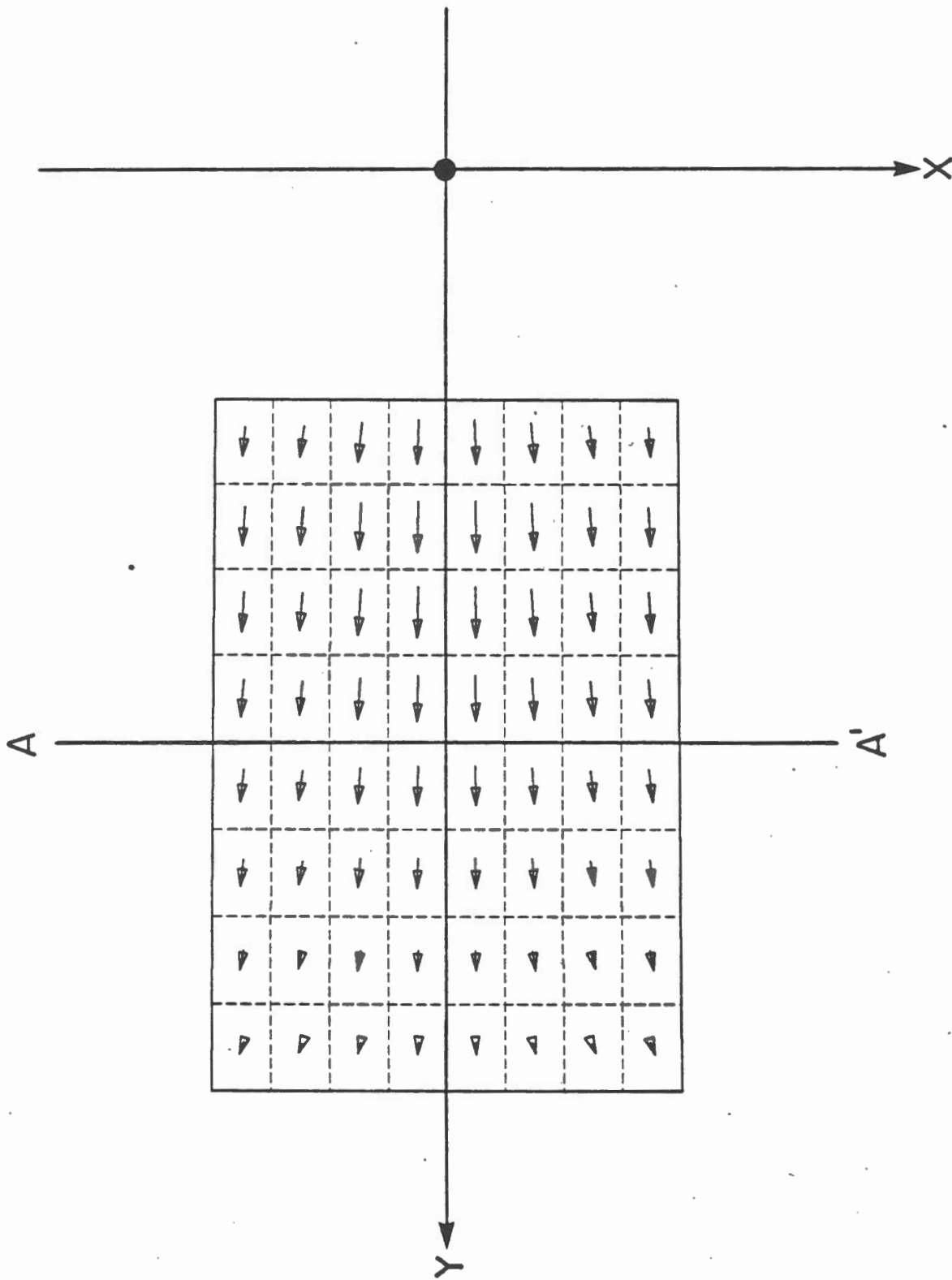


Figure 4.5.1: A plan view of a thin horizontal plate.

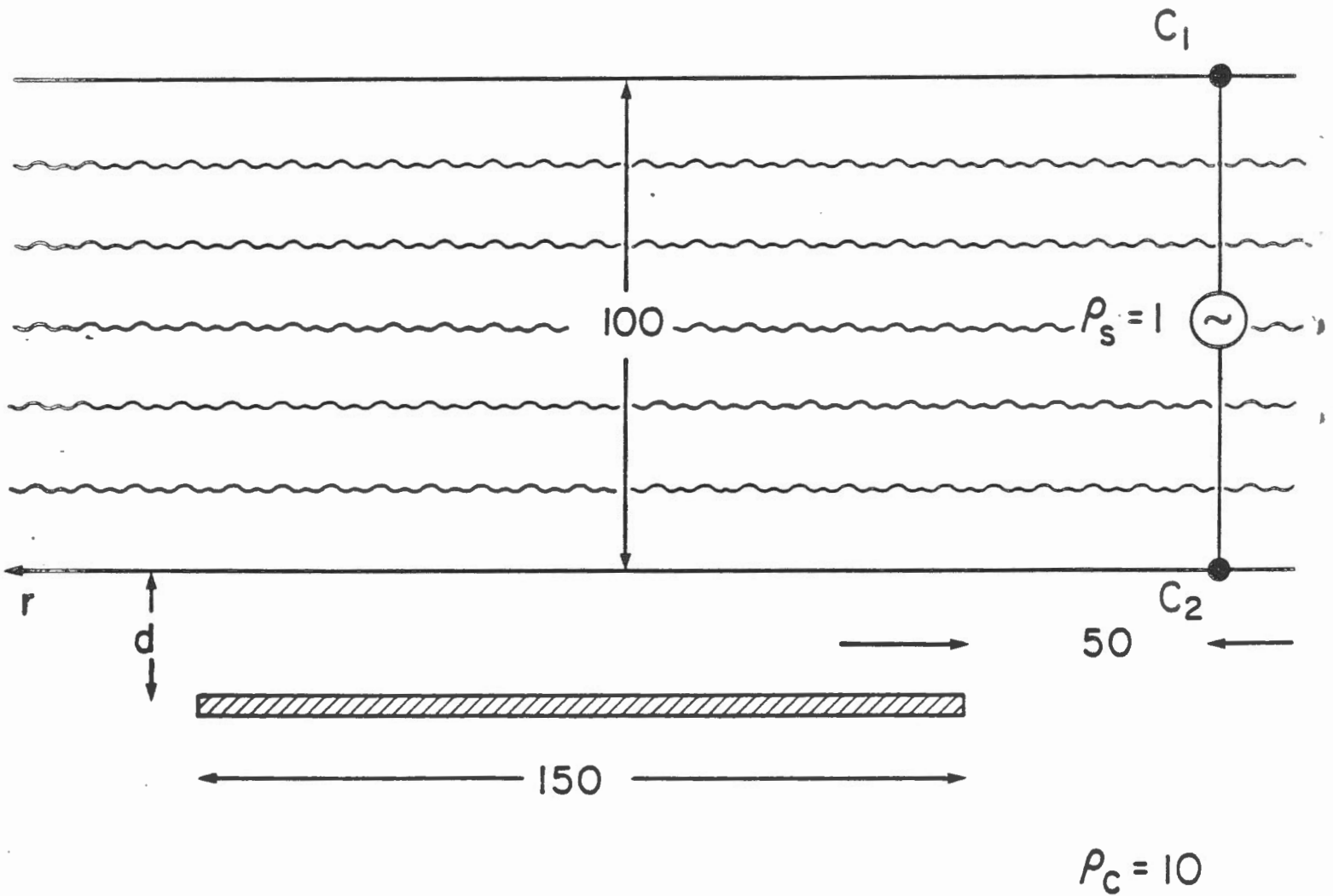


Figure 4.5.2: A sectional view of a thin horizontal plate.

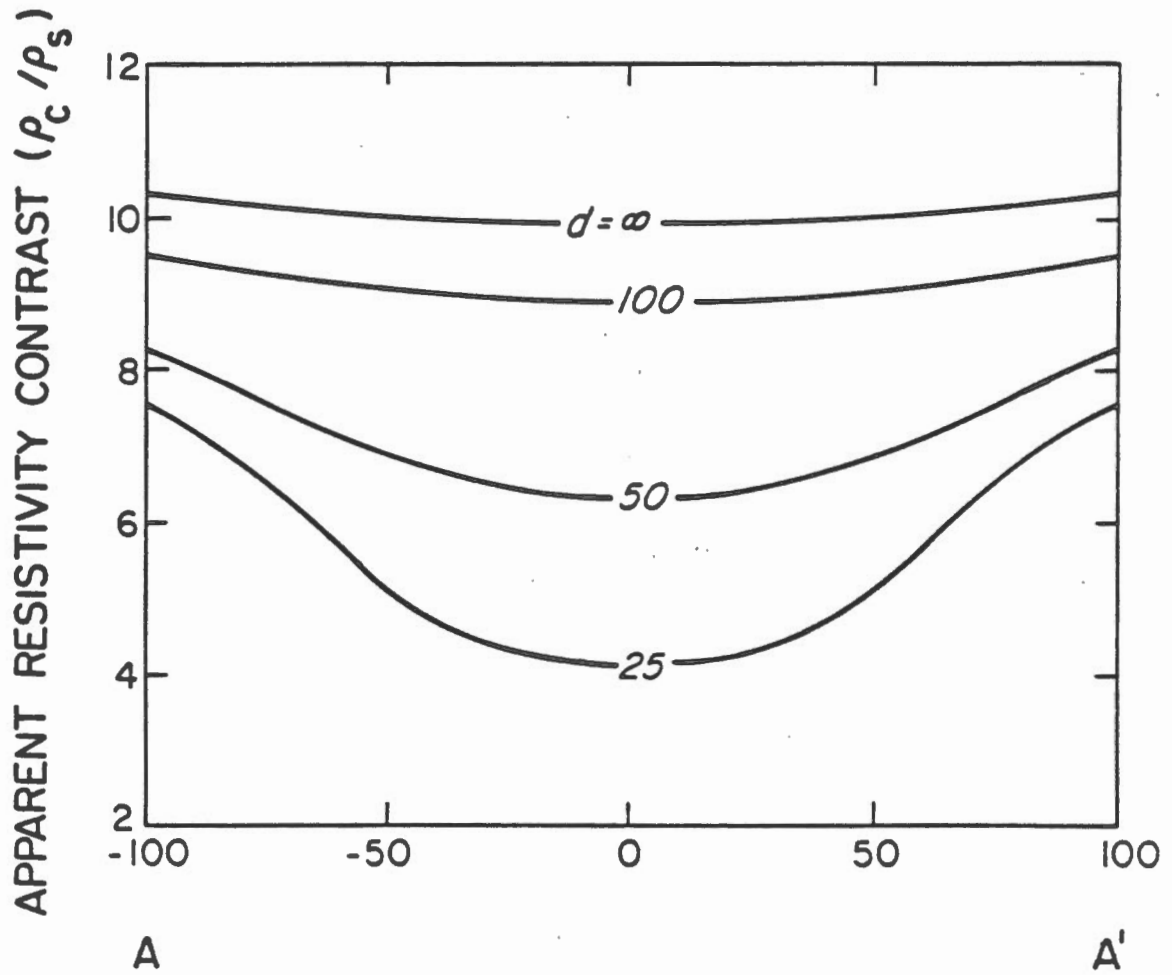


Figure 4.5.3: The apparent resistivity response of the horizontal plate along the profile AA' shown in Figure 4.5.1.

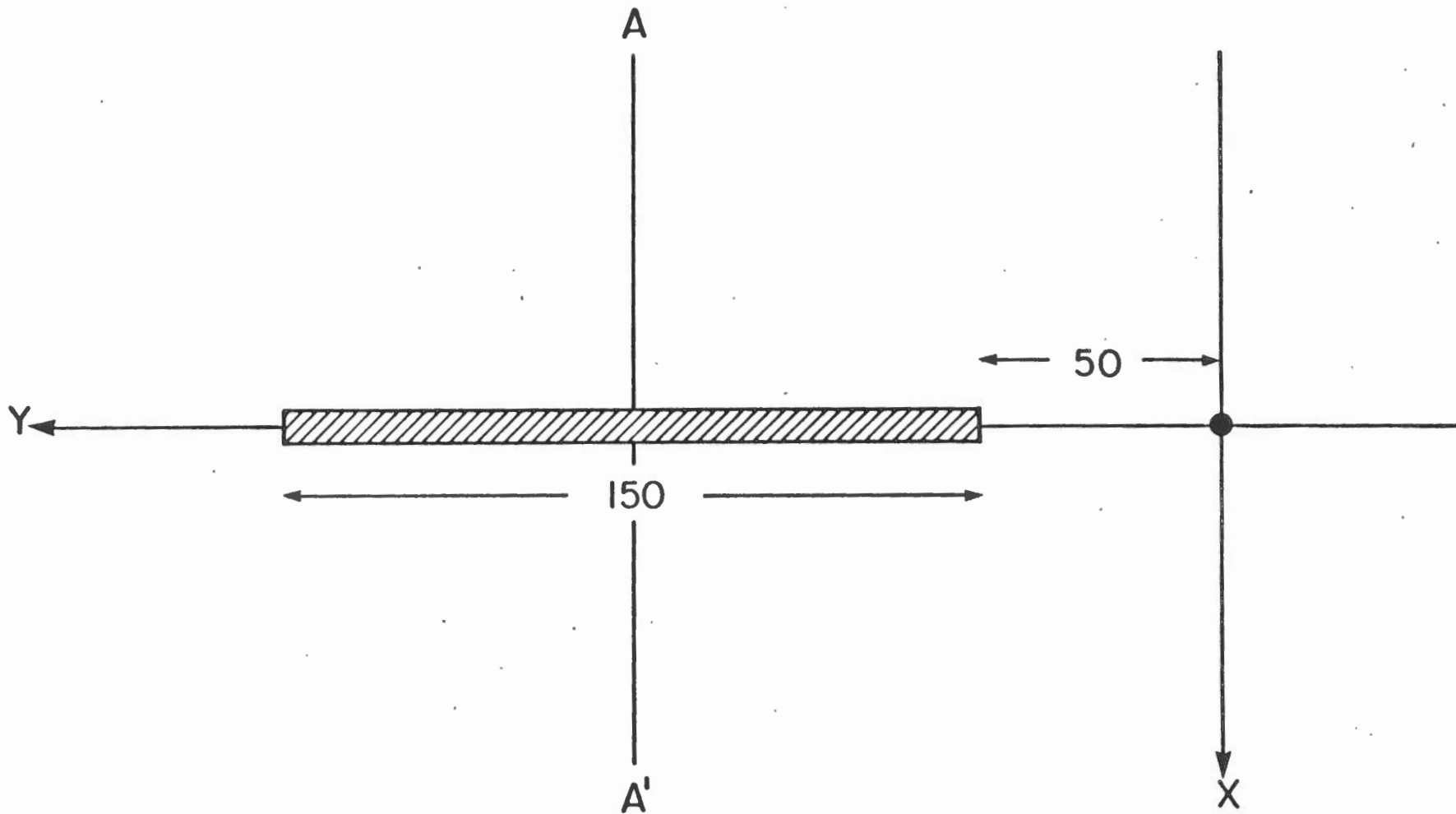


Figure 4.5.4: A plan view of a thin vertical plate.

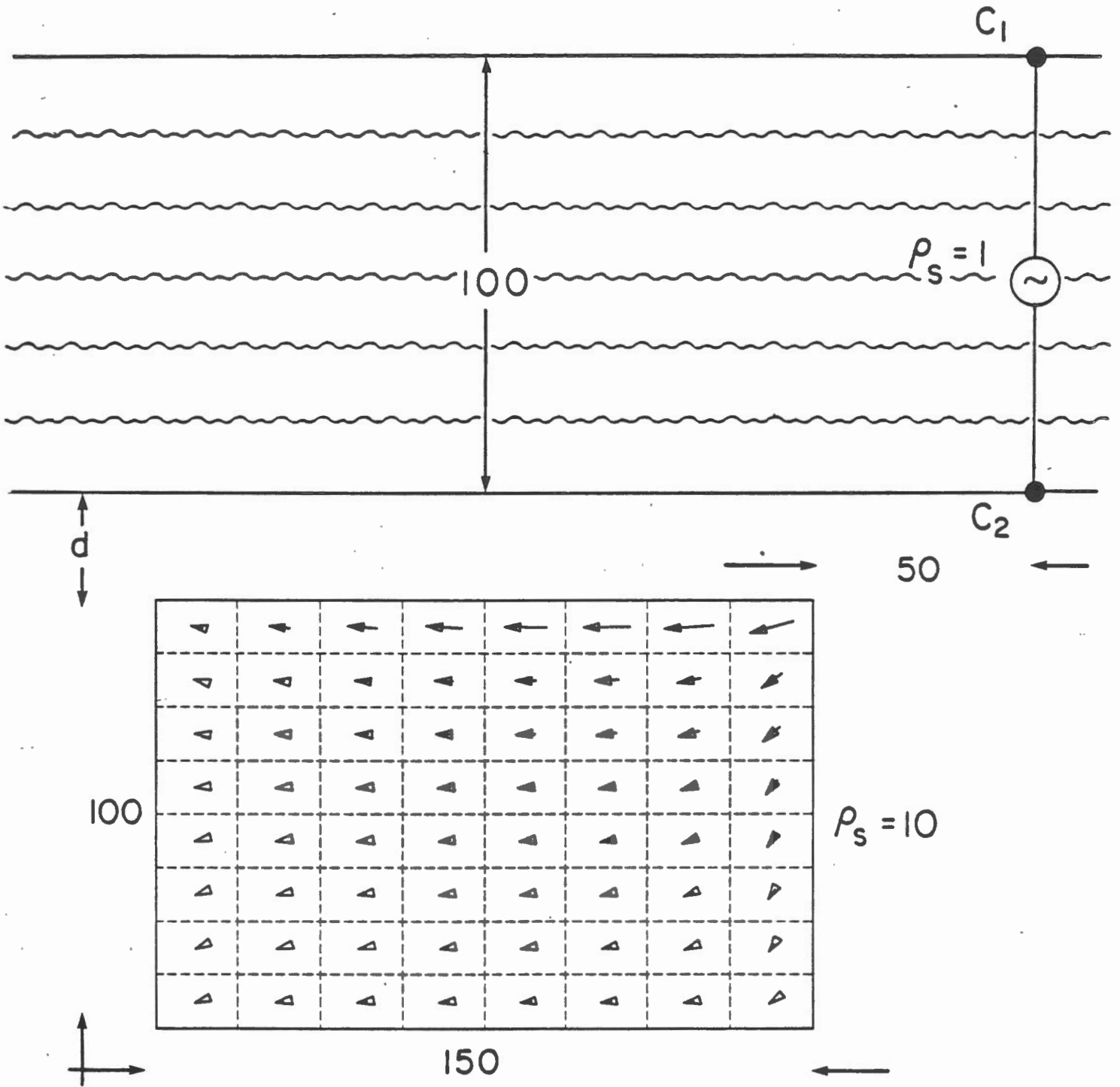


Figure 4.5.5: A sectional view of a thin vertical plate.

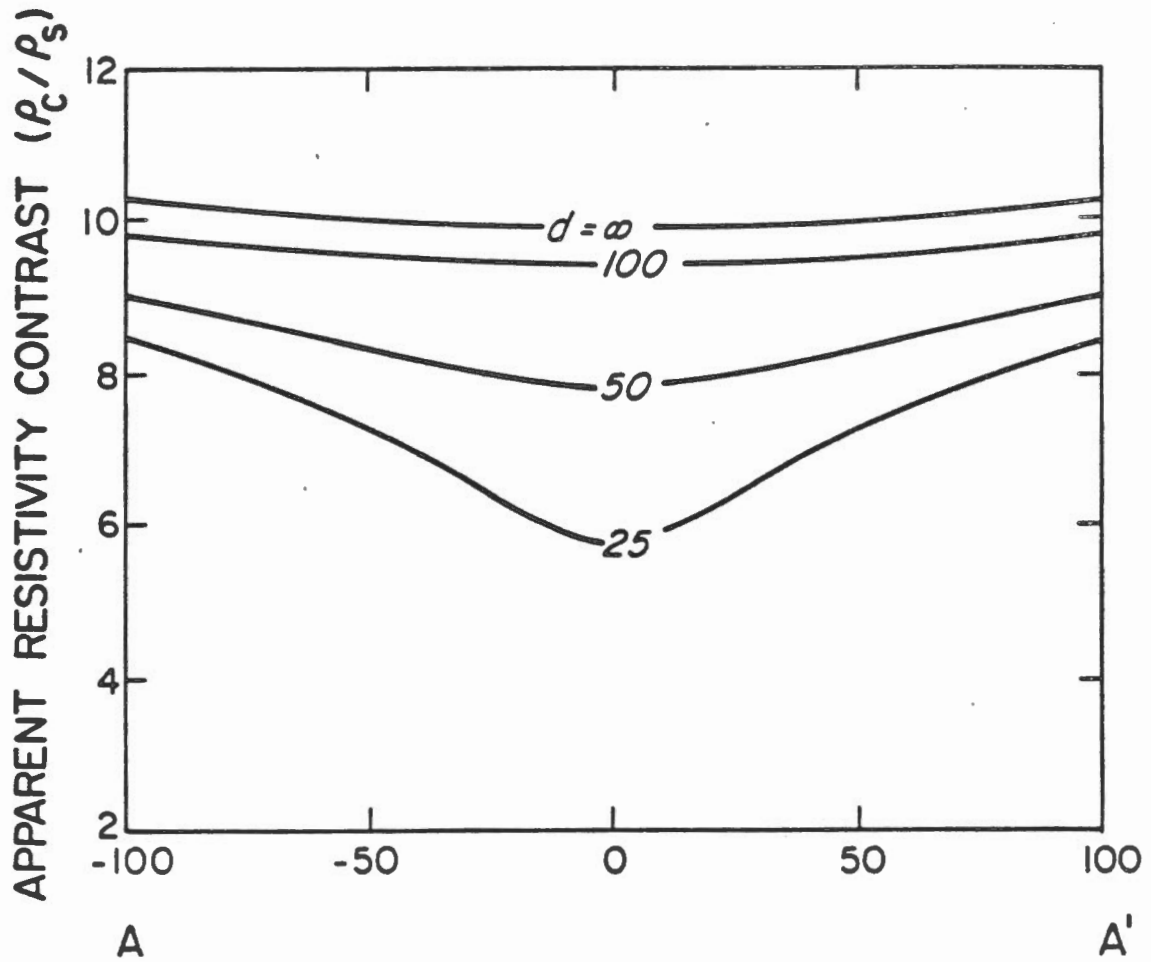


Figure 4.5.6: The apparent resistivity response of the vertical plate along the profile AA' shown in Figure 4.5.4.

is a thin horizontal plate located in a half-space beneath the sea in the vicinity of a MOSES bipole as shown in Figures 4.5.1 and 4.5.2. The resistivity of the half-space is assumed to be ten times that of the sea and the plate is a perfect conductor. The static limit of frequency is assumed. A set of apparent resistivity profiles AA' across the plate is shown in Figure 4.5.3. The plate is clearly detected provided its depth is less than about one third its size. The response of a plate of finite conductance will be less than the response shown by approximately the factor $\alpha/(1 + \alpha)$ where α is the dimensionless channelling number, the product of the conductance of the plate and the half-space resistivity divided by the length of the plate.

The corresponding figures for a vertical plate are Figures 4.5.4, 4.5.5 and 4.5.6. The software used to generate these results is also very flexible. Any number of flat or bent plates may be modelled.

The MOSES electromagnetic response of a horizontal disc co-axial with the MOSES bipole has also been programmed. Results are shown for sea layer thickness 50 m, resistivity .3 Ω m overlying a half-space of resistivity 3 Ω m. The disc was located 50 m beneath the sea floor. It was assumed to have a variable radius in the range 100 to 400 m and perfect conductance. The frequency of operation was selected as 3 Hz.

One of the major problems in numerical modelling is obtaining independent confirmation of the accuracy of results. It goes without saying that all our software is checked very thoroughly! A common scheme is to compare numerical results with analytic or closed form expressions. In the case of the disc, which is a layer of finite lateral extent, the radial current in it was compared with the radial current in a full layer, which can be written in closed form. Such a comparison of the in-phase and quadrature currents for a disc of radius 200 m is shown in Figure 4.5.7. The coincidence of the curves at radial distances small compared with 200 m is very good. At larger distances, the disc current decreases as it leaks out into the surrounding medium.

The apparent resistivities along a radial profile outward from the bipole is shown in Figure 4.5.8. The edge of the disc is clearly identified provided its radius is greater than about twice its depth. The corresponding phase curves shown in Figure 4.5.9 are a disappointment. There is no real effect of the disc at all! However, the reader should recall that the problem is purely a current channelling problem. The current

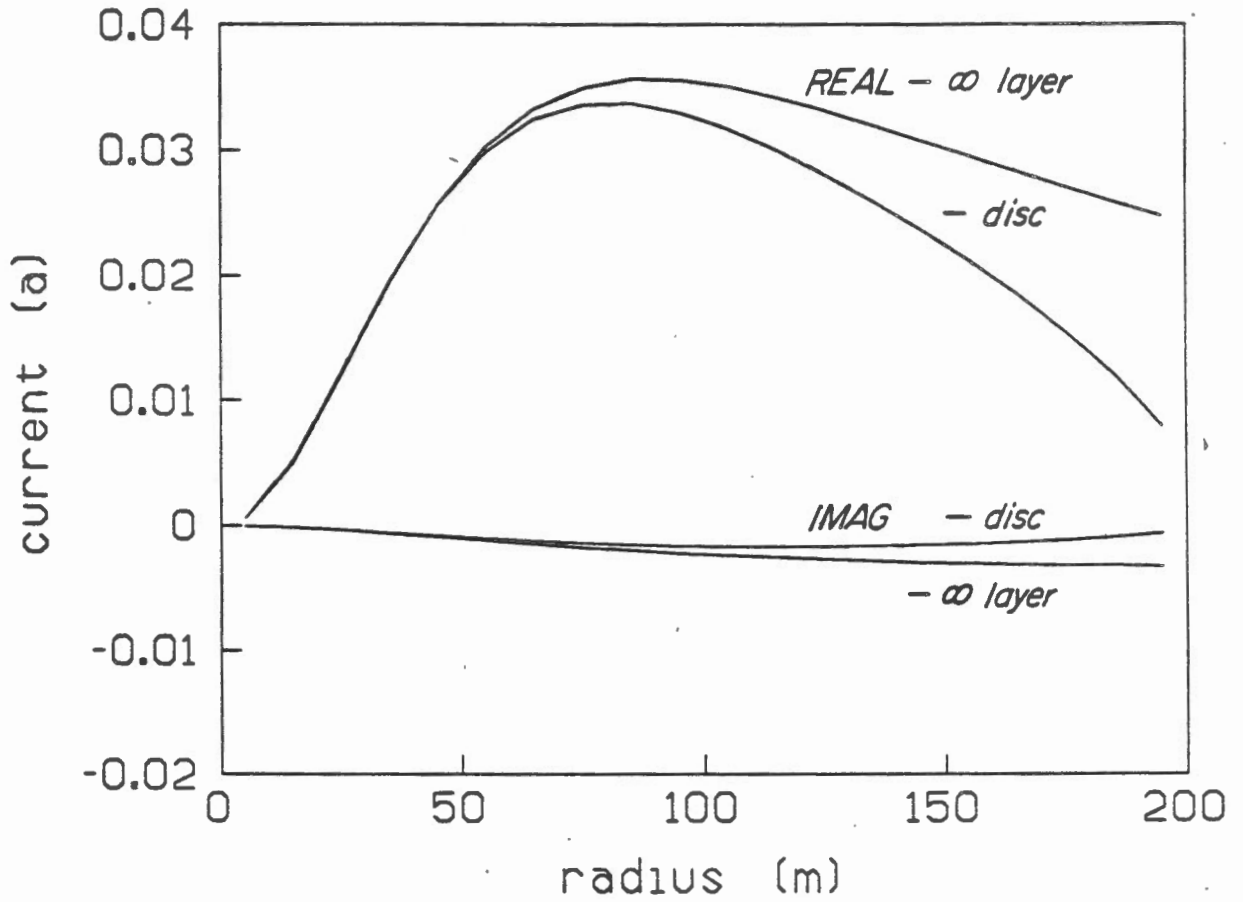


Figure 4.5.7: The in phase and quadrature currents collected by the disc of radius 200 m compared with the currents collected by a disc of infinite radius (a layer).

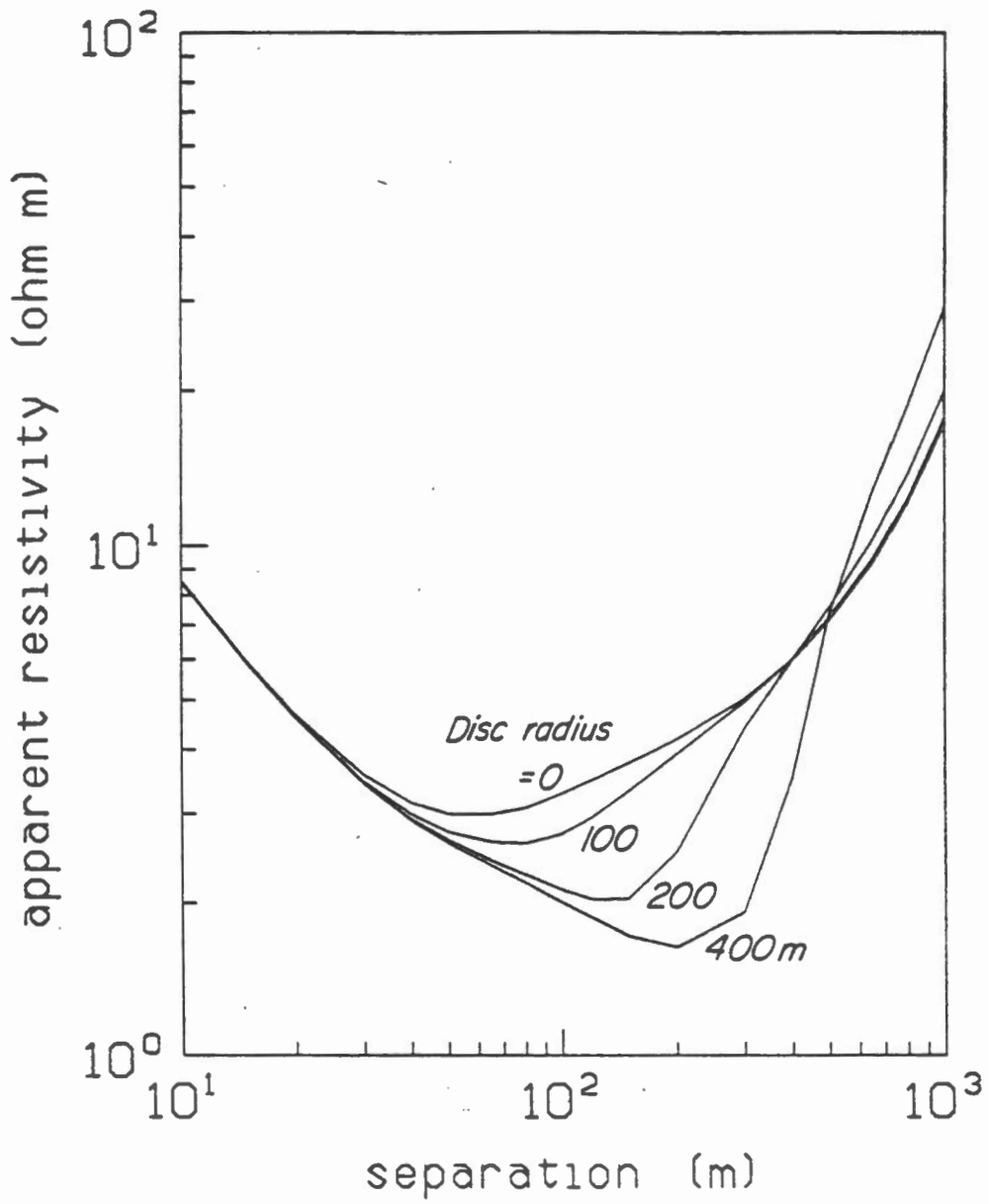


Figure 4.5.8: The apparent resistivity response of a disc of variable radius.

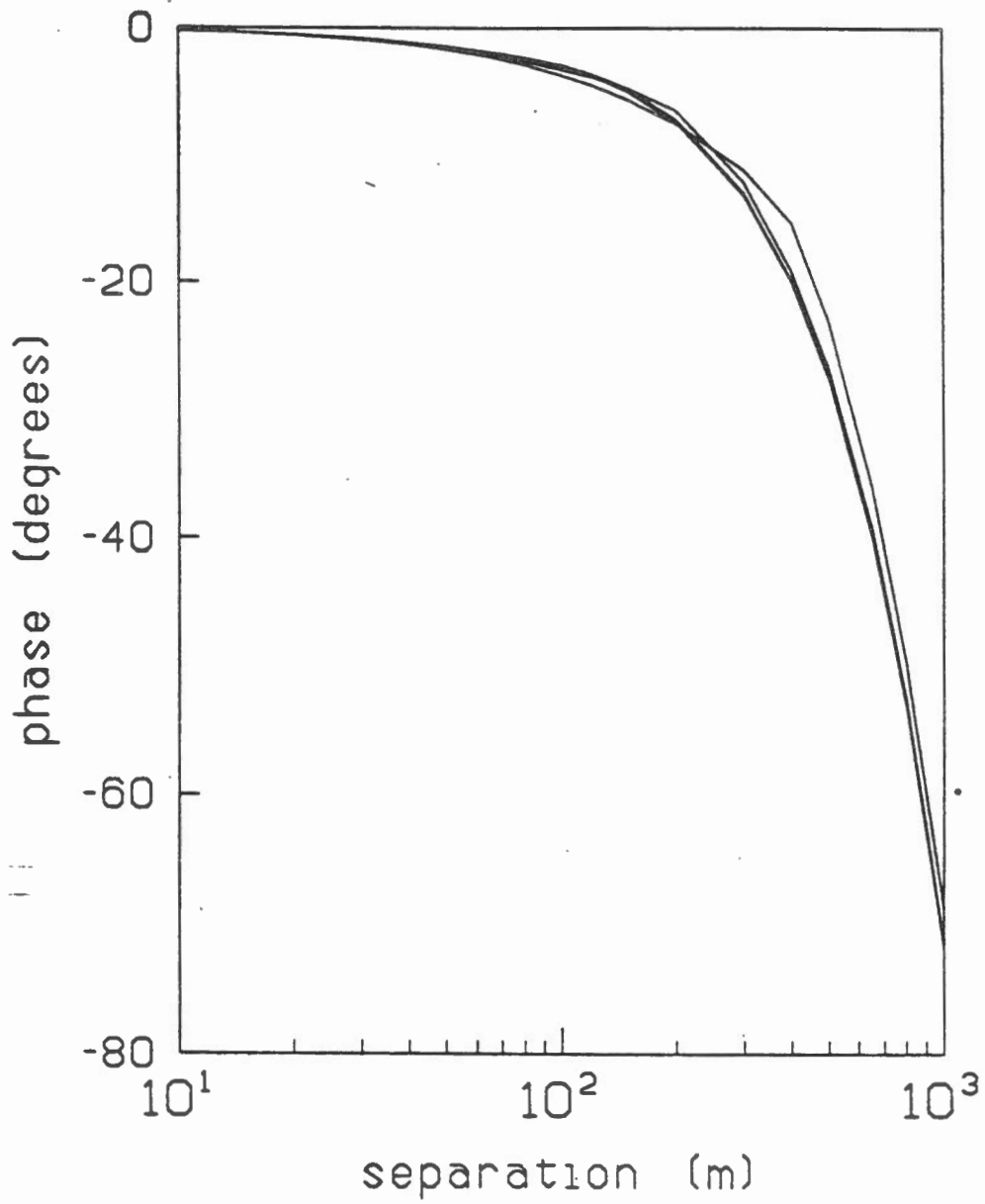


Figure 4.5.9: The phase response of a disc of variable radius.

gathered locally by the disc has the phase of the local current in the host medium. The magnitude of the current at any point in the medium will therefore change when the disc is present, but its phase will not. This seems to be a sufficient condition to make the phase of the magnetic field at the bottom of the sea, in turn, almost independent of whether the disc is present or not.

5. Research proposal and budget

The influx of funding from DEMR over the past year has enabled our group to take many cautious steps towards a full MOSES experiment in the Arctic, specifically north of Tuktoyaktuk in the Beaufort Sea. The purpose of this proposal is to obtain support for one further year only, so that a field trial can take place in the spring of 1986.

The proposed methodology is a little different from that described in previous publications (Edwards et al., 1985; Nobes et al., 1985). Because the availability to us of ship time in the Arctic is poor, we propose to operate on the sea ice which forms annually on the Beaufort Sea. Optimisation of signal strength requires a sea depth in excess of 50 m. The target will be selected in consultation with experts in local geology and should lie within 300 m of the bottom of the sea.

Even though we will have access to the equipment at all times, the fundamental automatic nature of the experiment will be retained. The transmitter and receiver will both be computer controlled and pre-programmed. In theory at least the packages which contain cold-sensitive electronic apparatus can consequently remain sealed against the elements for an extended period.

The concept of ICE-MOSES is shown in Figure 5.1. At the start of an experiment, the two computer modules which control the transmitter and the receiver respectively are programmed with operating frequencies, measurement times, stacking intervals, etc., and their crystal interrupt clocks are synchronized to provide a phase reference. The units are insulated and sealed and the equipment is transported to the field site. A single hole about 3" in diameter is drilled through the ice for the transmitter bipole. It is important to have a vertical bipole, and a flexible light cable tends to be deflected by sea currents. A better scheme may be to form the bipole by threading a robust, light, insulated wire through a number of short drill rod sections. The disassembled bipole, in the form of a bundle of rods, could be easily transported. A small A-frame would be required to aid reassembly of the bipole at a subsequent site.

The electrodes at the end of the bipole are stainless steel tubes about 2 feet long. The bipole and lower electrode assembly, and the upper electrode are connected independently to the transmitter. The latter is a constant voltage device, well tested

ICE - MOSES

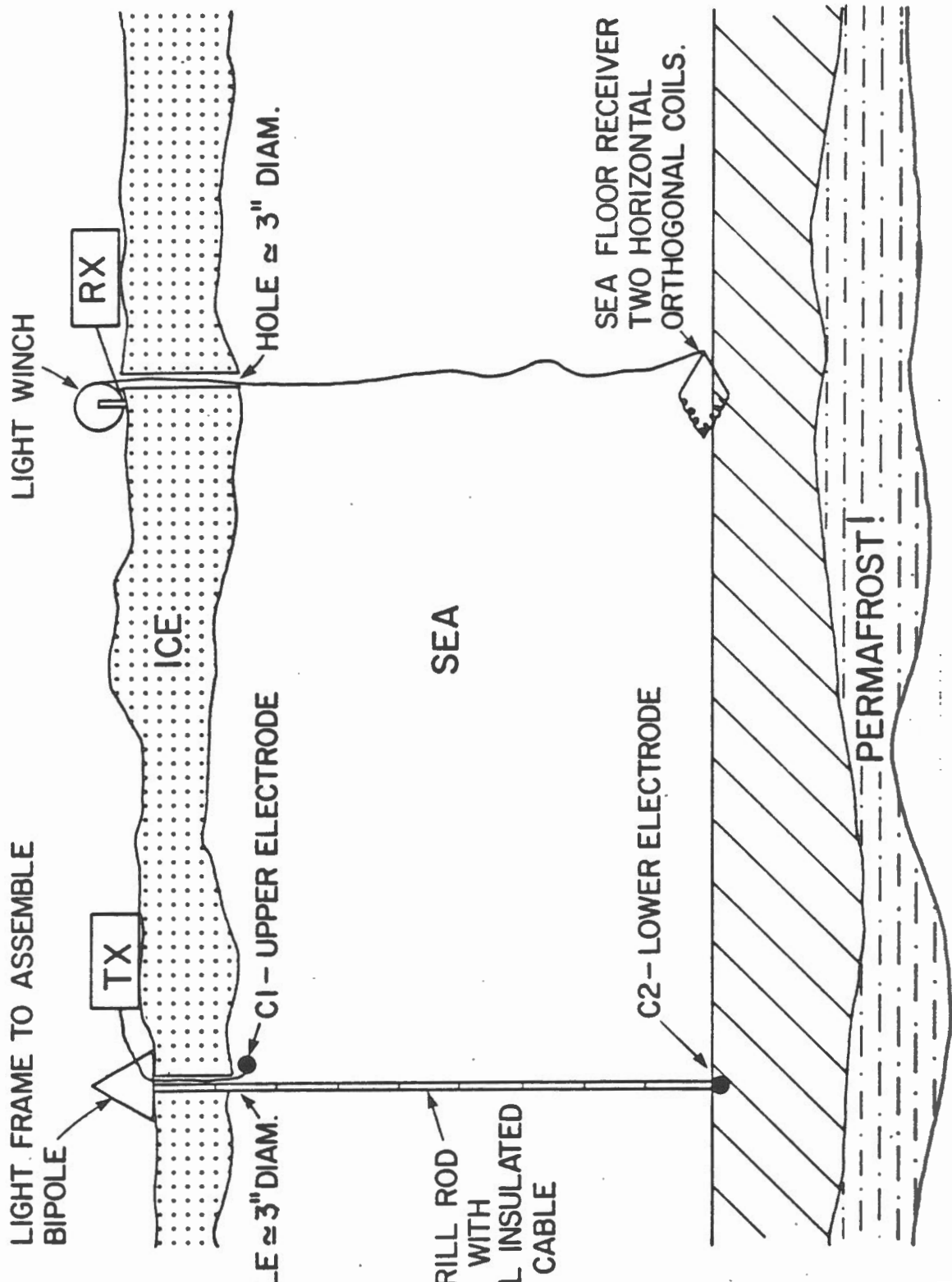


Figure 5.1: The ICE-Moses experiment.

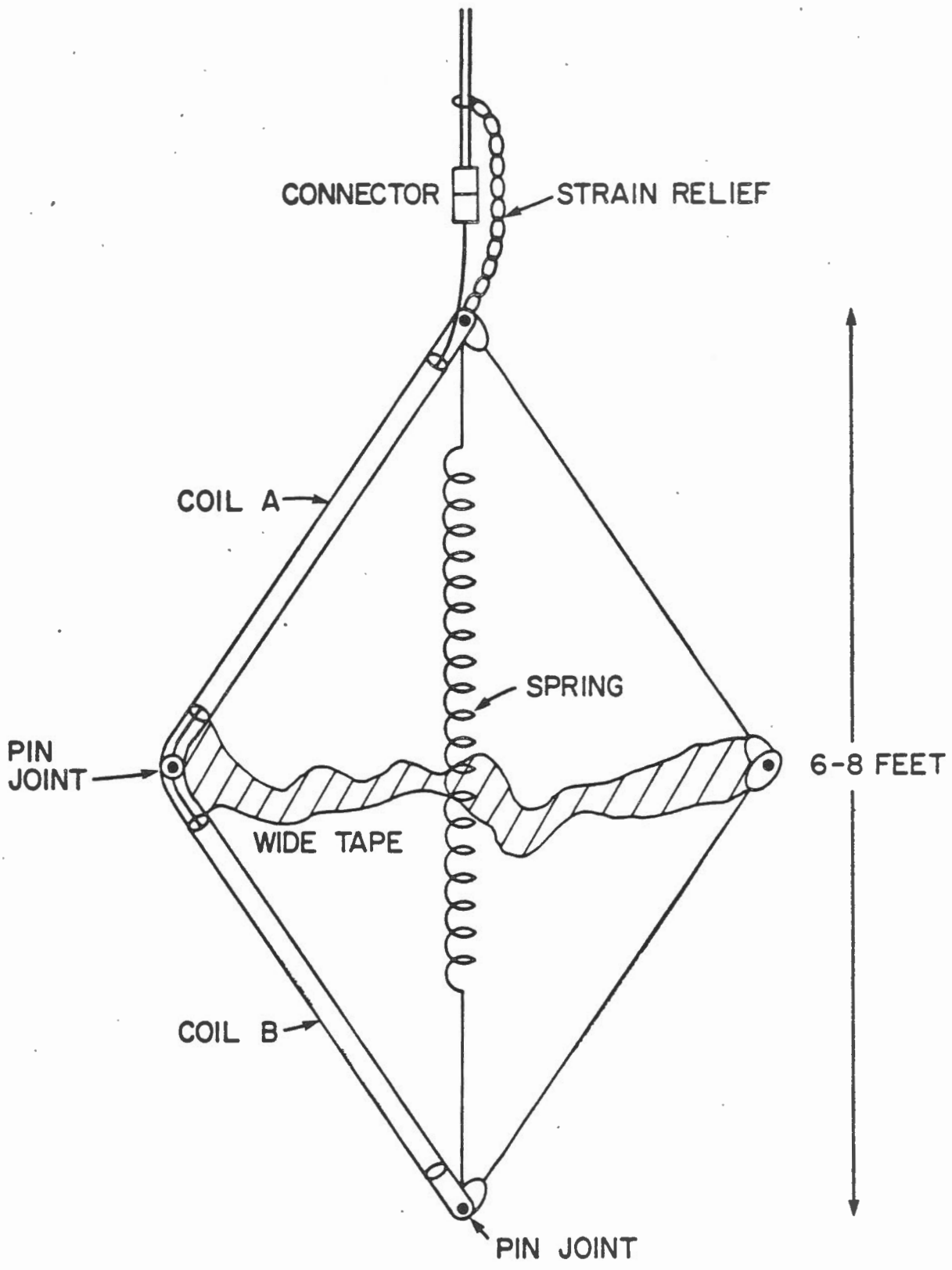


Figure 5.2: The new MOSES two-component sensor.

over a period of five years. It requires a 3-4 KW auxiliary generator and puts out about 12 A. The local computer controls the frequency of operation. It also monitors, stacks and records the output current and voltage so that the exact waveforms for a corresponding magnetic field measurement are known.

For an electrical depth sounding, a series of magnetic field measurements must be made at about 10 sites located at progressively increasing range from the bipole, to a maximum range of the order of 1 Km. The magnetic field sensor is sketched in Figure 5.2. It consists of two iron-cored coils, to sense two orthogonal components of the magnetic field. Each coil has its own battery powered pre-amplifier. On the sea floor, the coils form two sides of a square, horizontal frame. The signals recorded in the two horizontal, orthogonal directions are added vectorially to obtain the required azimuthal magnetic component. The exact orientation of the frame in the horizontal plane does not need to be known. The square frame is pin-jointed so that it can alter its shape and become a thin parallelogram capable of passing through a 3" diameter hole drilled in the ice.

The sensor is connected to its local computer which is identical to the computer controlling the transmitter. The computer stacks and records the two components of the horizontal magnetic field. Stacking times depend on the signal frequency and the signal to noise ratio. The final piece of apparatus at the receiver site is a light winch to recover the sensor. No auxiliary generator is required.

All of the apparatus described above including the computer hardware and software is to hand or can be borrowed, with one exception - the magnetic field sensor. In the course of the past several years similar sensors have been constructed by us, but the engineering involved in the sea floor sensor demands a new device. Consequently, the cost of our construction of this item is a major component of the budget.

The budget part of this document occupies only a few lines. We request in 1985/86 a sum of \$26000 (\$20000 net after U of T overhead has been removed) to construct and test the new sensor. We request in spring 1986 a sum of \$11700 (\$9000 net) to pay a technician for three months to expedite the project and travel with us to the field. In addition we request funding, or the equivalent, for accommodation and complete logistic support while in the Arctic (three weeks). The remaining costs estimated to be in excess of \$50000 will be covered by operating and northern supplement grants to the author from NSERCC.

References

- Becker, K., Von Herzen, R.P., Francis, T.J.G., Anderson, R.N., Honnorez, J., Adamson, A.C., Alt, J.C., Emmerman, R., Kempton, P.D., Kinoshita, H., Laverne, C., Mottl, M.J. and Newmark, R.L., 1982, In situ electrical resistivity and bulk porosity of the oceanic crust, Costa Rica Rift: *Nature*, v. 300, p. 594-598.
- Corwin, R.F., 1983, Marine Permafrost Detection Using Galvanic Electrical Resistivity Methods: *Proceedings, Offshore Technology Conference*, v. 1, p. 329-336.
- Chave, Alan D., 1985, Numerical integration of related Hankel transforms by quadrature and continued fraction expansion: *Geophysics*, v. 48, p. 1671-1686.
- Dieter, K., Paterson, N.R. and Grant, F.S., 1969, Induced polarization and apparent resistivity type curves for three dimensional bodies: *Geophysics*, v. 34, p. 615-632.
- Edwards, R.N., Lee, H. and Nabighian, M.N., 1978, On the theory of magnetometric resistivity (MMR) methods: *Geophysics*, v. 43, p. 1176-1203.
- Edwards, R.N. and Gomez-Trevino, E., 1979, MMR2D, A programme to compute the Magnetometric Resistivity (MMR) anomalies of two dimensional structures: available from School of Earth Sciences, Macquarie University, NSW, Australia
- Edwards, R.N., Law, L.K., and DeLaurier, J.M., 1981, On measuring the electrical conductivity of oceanic crust by a modified magnetometric resistivity method: *Journal of Geophysical Research*, v. 86B, p. 11609-11615.
- Edwards, R.N., Nobes, D.C. and Gomez-Trevino, E., 1984, Offshore electrical exploration in sedimentary basins: The effects of anisotropy in horizontally isotropic, layered media: *Geophysics*, v. 49, p. 566-576.
- Edwards, R.N., Law, L.K., Wolfgram, P.A., Nobes, D.C., Bone, M.N., Trigg, D.F., and DeLaurier, J.M., 1985, First results of the MOSES

- experiment: Sea sediment conductivity and thickness determination, Bute Inlet, British Columbia by magnetometric offshore electrical sounding: *Geophysics*, v. 50, No. 1, p. 153-161.
- Gomez-Trevino, E. and Edwards, R.N., 1979, Magnetometric Resistivity (MMR) anomalies of two dimensional structures: *Geophysics*, v. 41, p. 947-958.
- Gradshteyn, I.S. and Ryzhik, I.M., 1965, *Table of Integrals, Series, and Products*: Academic Press Inc, New York.
- Hoekstra, P., Sellman, P.V. and Delaney, A., 1975, Ground and airborne resistivity surveys of permafrost near Fairbanks, Alaska: *Geophysics*, v. 40, p. 641-656.
- Jackson, P.D., Taylor Smith, D. and Stanford, P.N., 1978, Resistivity-porosity-particle shape relationships for marine sands: *Geophysics*, v. 43, p. 1250-1268.
- Maillet, R., 1947, The fundamental equations of electrical prospecting: *Geophysics*, v. 12, p. 529-556.
- Nafe, J.E. and Drake, C.L., 1957, Variation with depth in shallow water marine sediments of porosity, density and the velocities of compressional waves: *Geophysics*, v. 22, p. 523-552.
- Nobes, D.C., Law, L.K. and Edwards, R.N., 1985, The determination of the resistivity and porosity of the sedimentary and fractured basaltic layers near the Juan de Fuca Ridge: *Geophysical Journal of the Royal Astronomical Society*, in press.
- O'Conner, M.J., 1980, Development of a Proposed Model to Account for the Surficial Geology of the Southern Beaufort Sea: Geological Survey of Canada, Open file report 954, pp. 128.
- Stefanescu, S.S., 1958, Uber die magnetische Wirkung einiger heterogenen Medien in der elektrischen Bodenforschung: *Zeitschrift fur Geophysik*, v. 24, p. 175-183.